Kinetic Monte Carlo simulations applied to Li-ion and post Li-ion batteries: a key link in the multi-scale chain

Article *in* Progress in Energy · August 2021

DOI: 10.1088/2516-1083/ac1a65

CITATIONS
0

READS
54

5 authors, including:

Edgardo Maximiliano Gavilán-Arriazu
National University of Cordoba, Argentina
14 PUBLICATIONS **92** CITATIONS
SEE PROFILE

Michael Mercer
Lancaster University
19 PUBLICATIONS **124** CITATIONS
SEE PROFILE

Harry E Hoster
Lancaster University
128 PUBLICATIONS **5,410** CITATIONS
SEE PROFILE

Ezequiel Pedro Marcos Leiva
National University of Cordoba, Argentina
245 PUBLICATIONS **3,498** CITATIONS
SEE PROFILE

Kinetic Monte Carlo simulations applied to Li-ion and post Li-ion batteries: a key link in the multi-scale chain

Title: Kinetic Monte Carlo simulations applied to Li-ion and post Li-ion batteries: a key link in the multi-scale chain

E. M. Gavilán-Arriazu[1,2,*], M.P. Mercer[3,4,5], D.E. Barraco[2], H.E. Hoster[3,4,5], E.P.M. Leiva[1,*]

[1]Departamento de Química Teórica y Computacional, Facultad de Ciencias Químicas, Universidad Nacional de Córdoba, INFIQC, Córdoba, Argentina
[2]Facultad de Matemática, Astronomía y Física, IFEG-CONICET, Universidad Nacional de Córdoba, Córdoba, Argentina
[3]Department of Chemistry, Lancaster University, Bailrigg, Lancaster, United Kingdom
[4]ALISTORE European Research Institute CNRS FR 3104, Hub de l'Energie, 80039 Amiens, France
[5]The Faraday Institution, Harwell Science and Innovation Campus, Didcot, United Kingdom

maxigavilan@hotmail.com, eze_leiva@yahoo.com.ar

Abstract:
Since 1994, Kinetic Monte Carlo (kMC) has been applied to the study of Li-ion batteries and has demonstrated to be a remarkable simulation tool to properly describe the physicochemical processes involved, on the atomistic scale and over long time scales. With the growth of computing power and the widespread use of lithium-based storage systems, more contributions from theoretical studies have been requested. This has led to a remarkable growth of theoretical publications on Li-ion batteries; kMC has been one of the preferred techniques to study these systems. Despite the advantages it presents, kMC has not yet been fully exploited in the field of lithium-ion batteries and its impact in this field is increasing exponentially. In this review, we summarize the most important applications of kMC to the study of lithium-ion batteries and then comment on the state-of-the-art and prospects for the future of this technique, in the context of multi-scale modeling. We also briefly discuss the prospects for applying kMC to post lithium-ion chemistries such as lithium-sulfur and lithium-air.

List of symbols

A	Electrode surface area
a	Size of one lattice site
α	Transfer coefficient (Symmetry factor)
Bi	Biot number
C	Concentration
c	Occupational parameter
Θ	Thermodynamic factor
$\Theta(\delta_e)$	Electron tunneling probability
D	Diffusion coefficient
D_{Li}	Chemical or Fickian diffusion coefficient
D_j	Jump-diffusion coefficient
D^*	Tracer diffusion coefficient
d	System dimension
Δ	Activation energy
Δ^*	Transition state energy barrier

Δ^0	"Bare" energy barrier
$\Delta^0{}_{diff}$	Bare energy barrier for diffusion
$\Delta^0{}_{i/d}$	Bare energy barrier for charge transfer
δ	Occupation ratio of cation sites available in electrolyte domain
δ_e	Tunneling distance from cathode surface
E_s	Microstate energy
E	Potential applied to the working electrode measured with respect to the reference electrode
E^0	Equilibrium potential
E_{eq}	Initial equilibrium (steady-state) potential of the experiment
$\vec{E}$	Electric Field
e	Fundamental electronic charge
F	Faraday constant
f	Correlation factor
Γ	Rate constant
γ	$t_{OFF}\ /t_{ON}$
H	Hamiltonian in the canonical ensemble
H'	Hamiltonian in the grand canonical ensemble
h	Height of the system
i	Current
i_p	Peak current
I_{cott}	Cottrellian current
j	Current density
j_0	Exchange current density
k_B	Boltzmann constant
k^0	Heterogeneous rate constant
L	Distance between the electrode/electrolyte interface and the edge of the electrode
Λ	Dimensionless kinetic factor
λ	Jump distance between diffusion sites
M	Number of lattice sites
M_n	Number of lithium ion neighbors
M_{if}	Number of sites located at the electrode / electrolyte interface
μ	Chemical potential
N	Number of particles
N_a	Avogadro constant
N_s	Number of particles in the microstate s
N_d	Number of removal events
N_i	Number of insertion events
n	Number of electrons transferred in a redox reaction
η	Overpotential
P	Probability of occurrence of a kinetic Monte Carlo event

Q	Charge corresponds to full material occupation
ΔQ	Total amount of charge transferred to the electrode when applying a potential step
R	Gas constant
r	Distance
$R_{diff}, R_{ch}, R_{\Omega}$	Diffusional, charge transfer and ohmic drop resistances
R_{cell}	Overall resistance of the electrochemical cell
R_{SEI}	Resistance of the solid electrolyte interphase
ρ	Viscosity of the solvent
s	Microstate
S	Number of microstates sampled in a Monte Carlo simulation
σ	Conductivity
σ'	Reduced conductivity
T	Temperature
t	Time
t_{ON}	Time lapse for the applied galvanostatic current
t_{OFF}	Time during which galvanostatic control is lifted
τ	Diffusion time constant
U	Potential energy
U^{Li-m}	Interaction energy of the lithium ion with the host material
v	Potential sweep rate
v^0	pre-exponential factor
x	Lithium ion occupation fraction inside the electrode material
Ξ	Grand canonical partition function
ξ	Random number
Z	Canonical partition function

1. Introduction:

The history of commercial lithium-ion batteries (LIBs) turns thirty during the current year. In this relatively brief period, they have become the most important industrial technology to promote a change in the energy paradigm towards renewable sources and eco-friendly storage devices. They have become prolific in portable electronic devices, are driving a revolution in mobile transport and could play a role in stationary storage [1–8].

A Li-ion battery is a secondary or rechargeable battery that alternates between charge/discharge cycles. The main foundation of a LIB cell lies in the reversible storage reaction of Li^+ between two materials. The electrodes in commercial LIBs are typically graphite (anode) and $LiCoO_2$ or similar layered transition metal oxide (cathode), the cathode being the source of Li^+ in the first charging cycle. Lithium manganese oxide (LMO) spinel and olivine lithium iron phosphate (LFP) are also viable cathode chemistries. The migration of Li^+ between the electrodes through the cell occurs in a non-aqueous electrolyte. Typically, the electrolyte is composed of an organic solvent, as mixtures of ethylene carbonate (EC) and either dimethyl carbonate (DMC); and a lithium salt, as lithium hexafluorophosphate ($LiPF_6$). A schematic view of a commercial LIB is shown in Figure 1.

The world demand for lithium-based storage devices is increasing drastically, posing a scenario of lithium shortage in the future. This is why, in recent years, research has been intensely focused on the improvement of LIB and the development of new battery technologies.

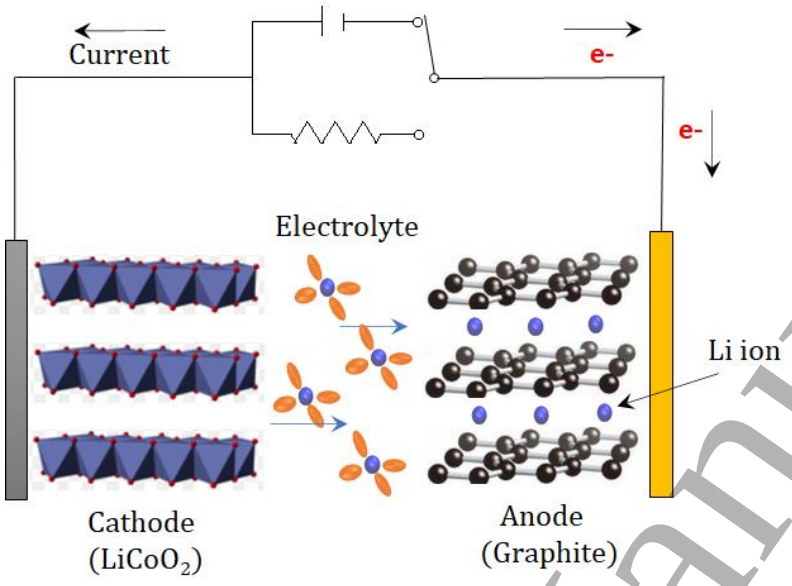

Figure 1: Typical setup of a LIB cell used in commercial devices, involving a cathode, an anode, and an electrolyte. The drawing illustrates the charging phase.

The advances in improving LIBs performance pushes the limits on designing materials at the micro- and nano-scale. Hence, it is crucial to understand how atomistic-detail events impact the electrochemical operation of storage devices. However, a detailed study on this scale exceeds the limits of experimental electrochemical techniques, as well as numerical models that study phenomena in the continuum. In parallel, theoretical methods that consider events in atomistic detail have a size limitation, since the more detailed the approximation, the larger the computational power required [9].

Since the beginning of lithium-based rechargeable batteries, attempts have been made to use Li metal as an anode, since this metal combines the properties of being the lightest metal with the lowest standard voltage (-3.02 V vs NHE), thus leading to a material with a very high specific capacity. However, the formation of dendrites and drastic volume changes are two common limitations for this material as an anode [10]. In the last years, several strategies have been applied to surmount these technical challenges, such as polymer coating [11,12], use of carbon hosts, metal hosts, or polymer hosts [13]. For these reasons, graphite remains the predominant anode material in LIBs, with small amounts of silicon oxides increasingly being added to increase the gravimetric capacity of the material [14,15].

Metallic Li is the material generally used as the anode in Post-Li-ion cells, like those foreseen for Li-air batteries (Li-O_2), and Li-sulfur (Li-S) batteries. Li-O_2 batteries use a cathode composed of an active surface material where oxygen is reduced, while Li-S cathodes contain sulfur embedded in a carbon matrix [16–18]. These two types of electrochemical cells present higher theoretical capacities than the commercial LIBs cells, so they have attracted attention because of the limitations of current LIBs for long-distance transportation. However, their practical application remains a challenge for

researchers, because both cells present severe technical problems, like parasitic reactions in Li-O_2 and the "shuttle effect" in Li-S [19,20].

Kinetic Monte Carlo (kMC, or the alternative denomination "dynamic Monte Carlo") is a powerful dynamic simulation technique that was developed by Gillespie [21] and refined by Fichthorn [22]. It allows simulating longer time scales, without losing configurational atomistic details, because-unlike other methods like Molecular Dynamics it overlooks vibrational atomic motions. This approximation becomes particularly relevant for intercalation systems because these are characterized by being, in general, very slow processes. For example, a routine Li^+/graphite cyclic voltammetry experiment involves potential sweep rates of the order of $\mu V.s^{-1}$ [23]; this means several days of measurement. The history of kinetic Monte Carlo simulations applied to the study of LIBs starts shortly after the birth of Li-ion commercial batteries, with the work of Deppe et al. in 1994 [24]. However, the largest critical mass of publications and references to specialized publications on this subject, dates back to the last few years, reflecting the need for an increasingly thorough understanding of events in LIBs. In this respect, Figure 2 shows the results for two Scopus (https://www.scopus.com/) searches: "Lithium-ion battery " + "kinetic Monte Carlo" (blue bars) and "Lithium-ion battery + "dynamic Monte Carlo" (white bars), performed on October 2020. The exponential growth of the number of publications over the years illustrates what we have said above.

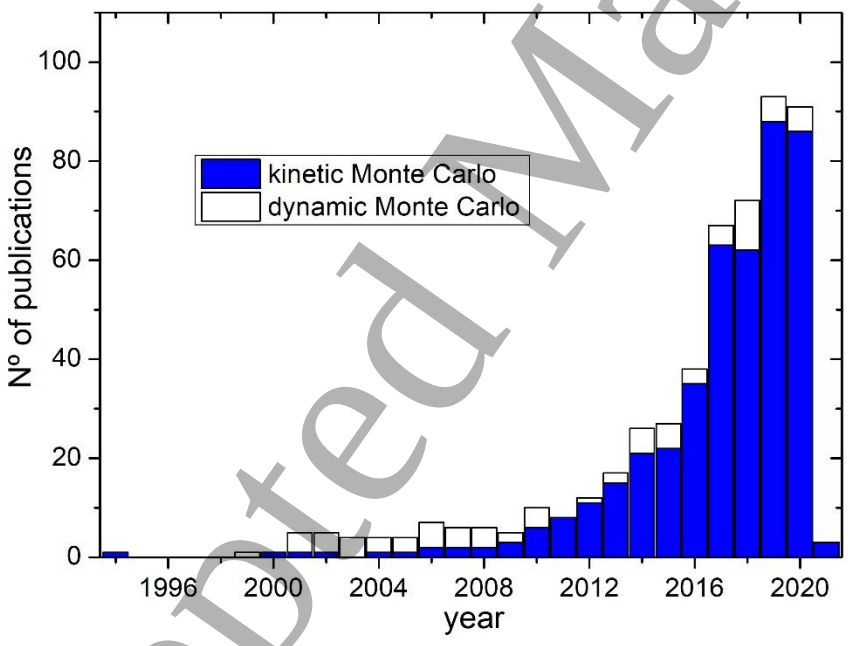

Figure 2: Results from a Scopus search: "Lithium-ion battery" + "kinetic Monte Carlo" (blue bars) and "Lithium-ion battery + "dynamic Monte Carlo" (white bars) in Scopus on October 2020.

The operation of a Li-ion cell presents a large and complex collection of different phenomena occurring simultaneously that determine the cell's overall performance: electrochemical reactions, transport phenomena, material alteration, temperature and volume changes, etc. This is why theoretical researchers generally need to couple different simulation/calculation approaches at different length and time scales. Such strategies are needed to develop refined models, in order not to overlook the physicochemical details. This is precisely the goal sought by multiscale models.

Multiscale modeling (MSM) is a type of modeling strategy that couples multiple lengths scale to provide a holistic description of a system. Generally speaking, it presents a hierarchy structure where the output of a finer resolution model serves as input to the next larger-scale model. In this way, the limitations of coarse-grained approximations are overcome by obtaining the results from more detailed models [9,25].

In the present review, we discuss the application of kMC to different aspects of lithium-ion batteries and closely related systems, like lithium-air (Li-air) and sulfur (Li-S) batteries (so-called post-Li batteries). Firstly, the kMC foundations are presented in an electrochemical framework, especially related to intercalation problems. Subsequently, the applications discussed are Li transport phenomena in electrodes, interfacial phenomena, mesoscale, ion transport in the electrolyte, and the formation of the so-called solid-electrolyte interphase (SEI). Finally, the state-of-the-art and perspectives of kMC within the multiscale modeling approach are considered.

2. The kinetic Monte Carlo technique and electrochemistry

Figure 3 presents a schematic view of different simulation techniques and their relative time and size domains. There, we can find that kMC is placed between Molecular dynamics (MD) and Meso-scale (MS) models. Roughly speaking, this scale involves simulation times between ≈10^{-10} s and several seconds, and length scales between ≈10^{-9} m and ≈10^{-3} m, but these limitations depend on the computational power and simulation strategies. For example, there are several works focused on accelerating kMC simulations [26–32], but we will not discuss these strategies here. There are several publications focused on the foundations of kMC [22,27,33–35] and we will deal with this later on.

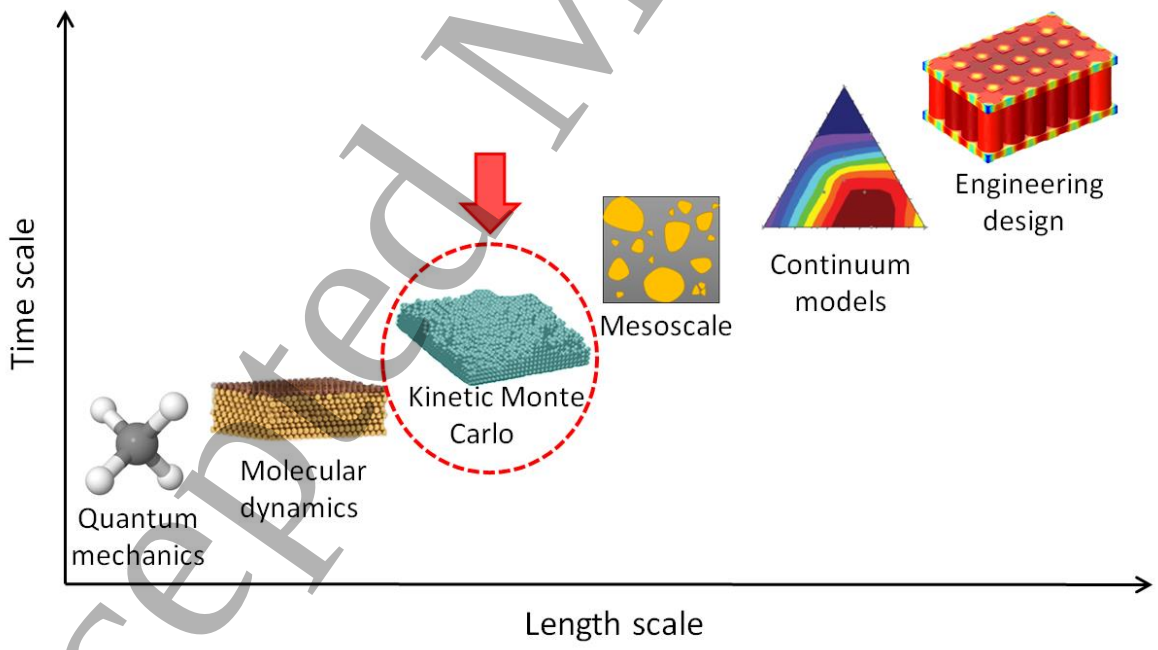

Figure 3: Scheme of relative length scales and timescales for different strategies of computer simulations. Kinetic Monte Carlo is placed between Molecular dynamics and mesoscale modeling. The figure for engineering design is reproduced from reference [36] with permission.

It is instructive to start comparing kinetic Monte Carlo with his predecessor, equilibrium Monte Carlo. Both simulation techniques can be used in a complementary way to study the impact of kinetics on the behavior of the system, in comparison with the thermodynamic equilibrium scheme.

2.1. Thermodynamics and kinetics: Equilibrium Monte Carlo and kinetic Monte Carlo

Within Statistical Mechanics, at a constant temperature, volume and particle number (NVT), all thermodynamic properties of a physical system can be obtained from a single mathematical expression, the canonical partition function:

$$Z = \sum_s \exp\left(-\frac{E_s}{k_B T}\right) \quad (1)$$

where the sum is taken over all the microstates *s* of the system, and E_s is the energy for those states. Similarly, for open systems a grand canonical partition function (Ξ) can be written by including the chemical potential of the particles involved:

$$\Xi = \sum_{N_s} \sum_s \exp\left(-\frac{E_s - N_s\mu}{k_B T}\right) \quad (2)$$

where N_s is the number of particles in microstate *s* and μ represents the chemical potential of the particles (in the present case Li-ions) of the system and the first sum runs over all possible particle numbers. In battery models, μ is an important term because it is related to the potential of the electrochemical cell. If metallic Li is the reference electrode, then the equilibrium potential of the cell is $E(V) = -\mu/e$, where e is the fundamental electronic charge. Moreover, it is pertinent to clarify that for bulky systems the results should not depend on the ensemble used, but some ensembles are more convenient to use in certain situations than other ones. For example, when simulating the electrode/electrolyte interphase where insertion/deinsertion of particles occurs, the natural choice is the Grand Canonical ensemble, where μ is the control parameter linearly related to the electrode potential [8,37,38]. On the other hand, in simplified lattice models [39–42], the canonical ensemble is more simple to handle, and μ is an outcome of the modeling.

In principle, E_s contains translational and internal (rotational, vibrational, electronic, nuclear) degrees of freedom, that can be suitably separated [43]. In the case of intercalation compounds, we are often interested in calculating all the possible ways to distribute the ions (and vacancies) over the host, and we ignore the electronic and vibrational contributions to the energy, since both show a small change with the lithiation degree, as compared with the configurational contribution [39,42,44–50]. If the partition function, Equation (1) or (2) can be directly calculated, such as the case of a two level system in the mean field approximation, then all of the thermodynamic parameters emerging from the configurational contributions to the free energy can be obtained from analytical expressions. However, for a more complex interaction Hamiltonian, this approach is generally not computationally tractable due to there being too many states to count. In this case, Monte Carlo techniques, as described below, can be utilized.

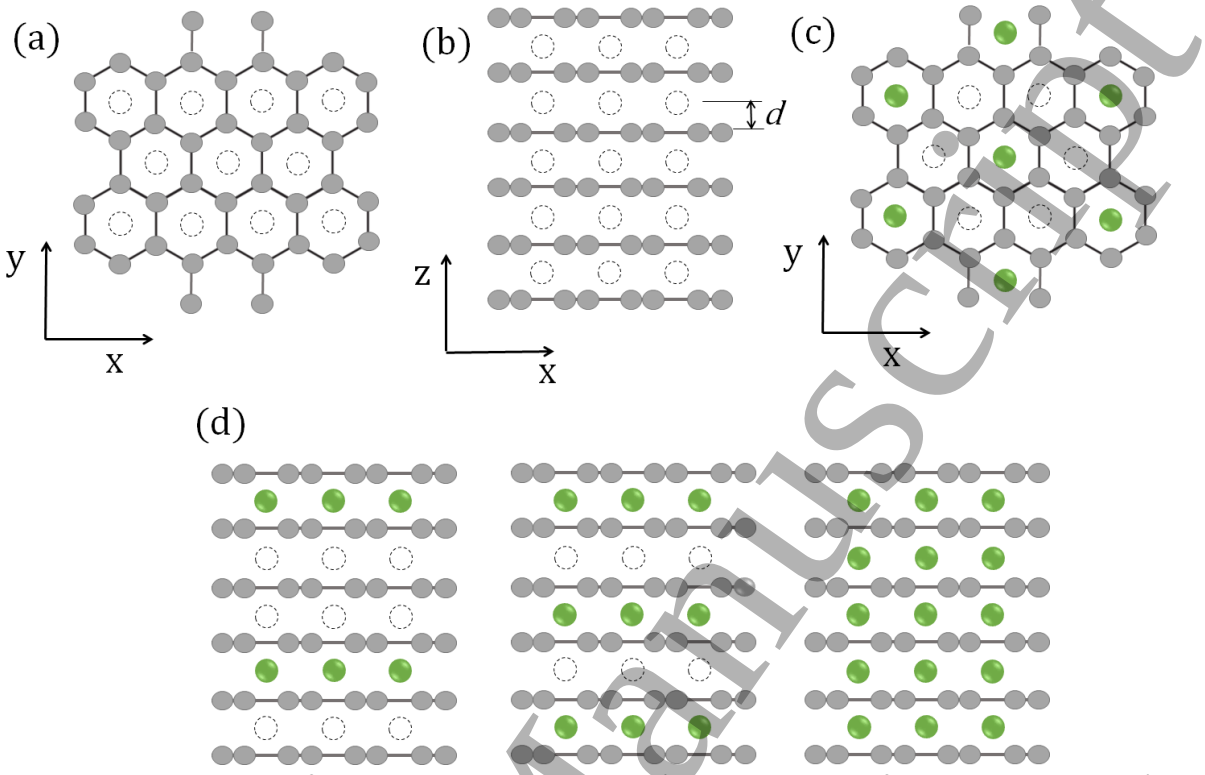

Figure 4: Lattice-gas setup for graphite with AA stacking (corresponding to fully lithiated graphite). A further approximation of the model is to keep this stacking for all Li occupations of the lattice. Empty sites are represented with white circles, sites occupied with Li^+ are represented with a green circle. The graphite substrate is represented in grey (carbon atoms with circles and bonds with lines). (a) upper view of the lattice + graphite substrate, lattice sites are located in the center of the carbon hexagons. (b) lateral view of lattice + substrate, *d* is the middle of the distance between two adjacent sites located in different layers. (c) Upper view for a full lithiated graphite layer. (d) different stable configurations (stages) observed during graphite intercalation.

These configurational states can be easily modeled within a lattice-gas approach. This model provides fixed points for the inclusion of Li^+ ions interacting with the host and with each other. Each site is marked with a Li^+ occupation status: full or empty; considering that none may have double occupancy. The spatial arrangement of the lattice sites is constructed from the crystalline structure of the host. For example, graphite consists of a honeycomb-like structure, comprising a stack of sheets made up of hexagonal carbon rings (Figure 4). The centers of the carbon hexagons in graphite with AA stacking are used to define the lattice for the Li-ion gas (Figure 4a). The sites of the lattice are located at a distance *d* from these centers (Figure 4b). This distance corresponds to half of the distance between the (0001) graphite basal planes. With this information, one can construct a 3D lattice-gas structure with a preexisting graphite substrate, composed of piles of 2D lattice intercalation sites with triangular geometry.

The energy expression (interaction Hamiltonian) that rules the configuration of Li^+ embedded in different systems (intercalation materials or electrolytes) can be modeled by considering the interaction energies among the particles (ions) of the system and the interaction of the ions with the host. Two approximations can be made to simplify this problem. One of them is to divide the Hamiltonian into two separate contributions: one due to the interaction among inserted ions and

another one between the inserted ions and the host. A further simplification is to assume pairwise interactions. With these two approximations, the Hamiltonian is:

$$H = \frac{1}{2}\sum_i^M \sum_{j\neq i}^{M_n}\left(c_i c_j U_{i,j}\right) + \sum_i^M \left(c_i U^{Li-m}\right) \quad (3)$$

In this expression, the summations run over the total M lattice intercalation (deposition) sites. The symbol c is an occupational parameter ($c = 0$, the site is empty, $c = 1$, the site is occupied by an ion) The terms $U_{l,k}$ and U^{Li-m} are interaction energies. The first of these terms considers the pairwise interaction of each Li^+ with the surrounding M_n Li^+ neighbors, the second is a constant value for the interaction energy of the ion with the host material.

In intercalation phenomena, the exchange of Li^+ between the electrode and the electrolyte is a key factor. Thus, it is suitable to set up a Li^+ reservoir with a fixed chemical potential that exchanges ions with the material. The partition function in this situation is given by Equation (2). However, as we stated before, due to the huge number of possible configurations, it is usually not possible to obtain the partition function by a simple summation over those microstates to derive any thermodynamic property. Hence, an adequate strategy to avoid the computation of the partition funtion consists of performing a random sampling with the so-called Metropolis algorithm, using a computer simulation [51]. Within this method, it is possible to obtain the average value of a thermodynamic property (say Y) over a finite (but large) number of sampled microstates sampled (S), Equation (4). This is known as a Monte Carlo simulation or Equilibrium Monte Carlo simulation [52–56].

$$\langle Y \rangle = \frac{\sum_i Y_i}{S} \quad (4)$$

Usually, Metropolis Monte Carlo is considered to be a stationary method, because it can only yield the thermodynamic properties of a system in equilibrium, without considering its physical time evolution. Conversely, kinetic Monte Carlo (that will be discussed shortly), follows the kinetic evolution over the free energy landscape of the system until reaching configurations around the global minimum. These differences between MC (light blue circle) and kMC (yellow arrow) are illustrated schematically in Figure 5a. So, these two simulation methods provide different approaches to the behavior of the system under consideration that may be contrasted: The thermodynamic equilibrium properties (MC) and the kinetic evolution (kMC). Consequently, to ensure that the algorithm reaches equilibrium in the fewest possible steps, MC allows the attempts of insertion/deletion of Li ions into/from any of the lattice sites (Figure 5b). On the contrary, the kMC algorithm must be adapted to consider events that occur close to a real (intercalation) situation; for example, the insertion/deletion attempts must be restricted to the exchange of Li^+ only at the electrode/electrolyte interphase, as depicted in Figure 5c. In surface deposition phenomena, like it is the case of Li^+ deposition on metallic Li, insertion and deletion events are more similar in both simulation techniques, because the interphase is closer to all the lattice sites. Another crucial event in the case of intercalation phenomena that must be included in a kMC algorithm is the diffusion of the ions inside the host or over the surface of the electrode (Figure 5c).

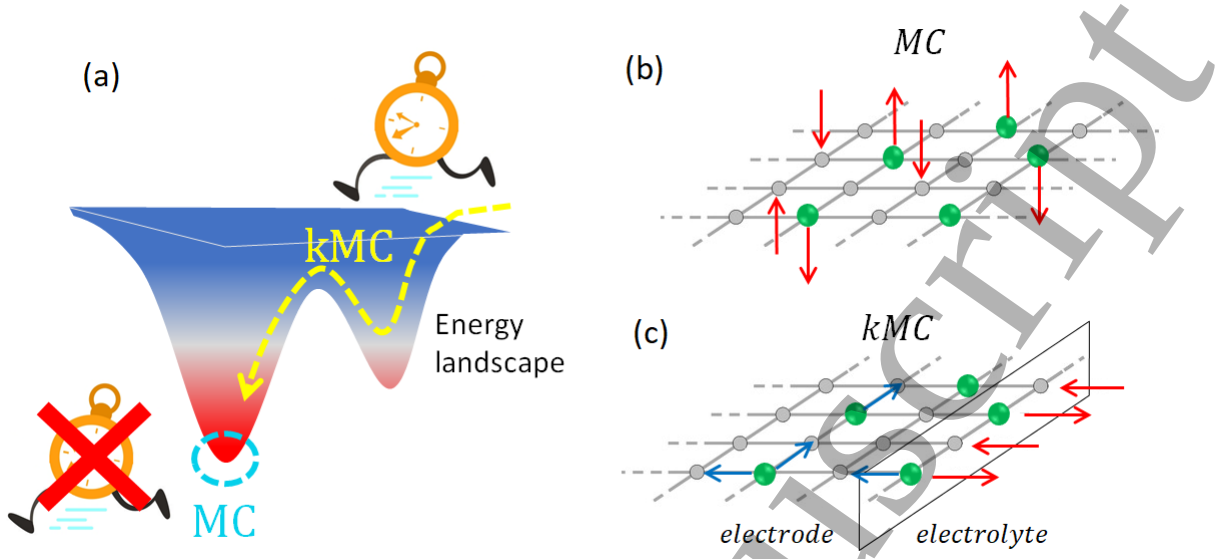

Figure 5: (a) Schematic comparison between the time evolution of kMC (yellow arrows) over the energy landscape provided by the configurations of the system and the stationary MC method (light blue circle)., where the thermodynamic quantities are obtained close to thermodynamic equilibrium. Higher energy values are marked in blue while lower energies are marked in red. (b) Insertion/deinsertion events allowed in a typical equilibrium MC simulation. Grey circles denote empty sites, while green spheres denote sites occupied by Li-ions. The red arrows indicate the attempts to change the occupation status of the site. (c) Events allowed in a kMC simulation of Li-ion (de)intercalation. The symbols used are the same as in Figure b), but the additional blue arrows indicate possible diffusion movements. Ions are also allowed to exchange at the electrode/electrolyte interphase, which is represented with a rectangle at one of the sides of the lattice.

Several studies have focused on thermodynamic equilibrium using MC to study different issues in LIBs, such as the staging phenomena [37,57], the entropic contributions to the intercalation process [38,48,58], the stability and phase transitions of lithium intercalation compounds and their structures [59,60], the impact of host changes during Li^+ intercalation [61–63], the construction of phase diagrams [64,65] and the solid electrolyte interface (SEI) [66].

2.2. The foundations of kMC

The basic principle of a kMC simulation is to generate a Poisson process of stochastic events with a hierarchy of rate constants Γ_j, in such a way that events with higher rates are more probable to occur than slower ones [22,67].

The workflow of a kMC algorithm is summarized in Figure 6.

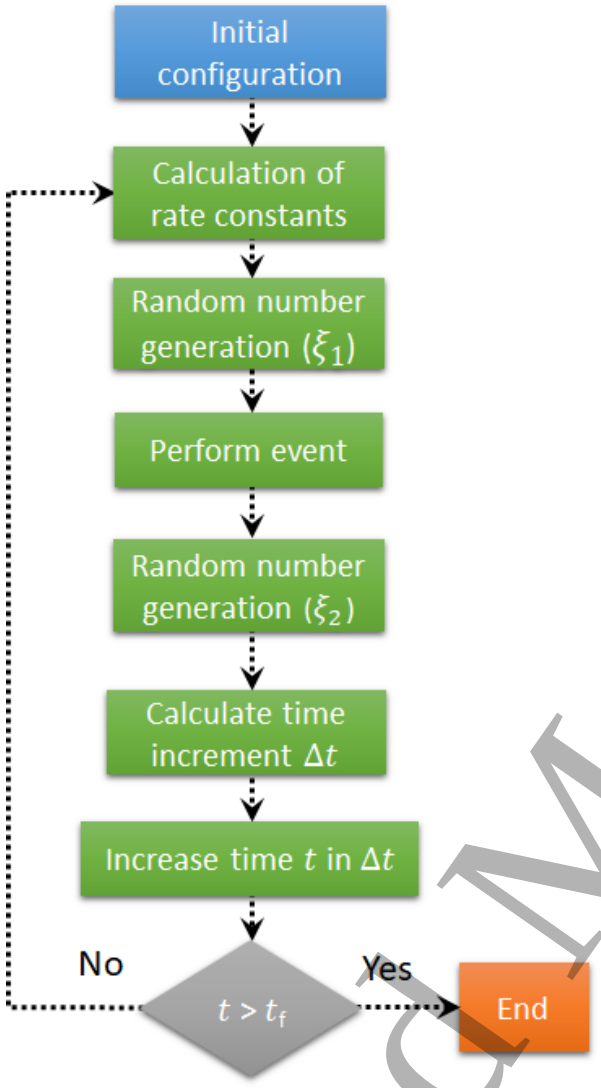

Figure 6: Flow diagram for kMC *Rejection-free-algorithm*. t_f is a predefined cut-off time.

Given a configuration of the system, the rate constants for all possible events, for each of the sites of the lattice, are generally expressed in an Arrhenius form, Equation (5) (other rate equations can be used as we will see in the next section), with a pre-exponential factor v^0 (average value of the vibrational motion or mean frequency of jumps) and an activation energy Δ_j. Then, given the total rate Γ_T as the sum of the rates of all possible events, Equation (6), the probability of occurrence of each event, P_i, is calculated with Equation (7).

$$\Gamma_j = v^0 \exp\left(-\frac{\Delta_j}{k_B T}\right) \quad (5)$$

$$\Gamma_T = \sum_j \Gamma_j \quad (6)$$

$$P_j = \Gamma_j / \Gamma_T \quad (7)$$

The rates obtained with Equation (7) are included in a list, where one of them is selected to occur using a random number ξ_1, between 0 and 1. Once the event has been identified from the list and performed, the time t is incremented a quantity Δt, Equation (8), which is obtained with a second random number ξ_2 between 0 and 1. Equation (8) calculates the time lapse from an exponential distribution.

$$\Delta t = -\frac{\ln(\xi_2)}{\Gamma_T} \tag{8}$$

For the next time step, the Γ_js are recalculated for the new configuration generated in the previous step, and the list of probabilities is updated. This commonly used *Rejection-free-algorithm,* summarized in Figure 6, ensures that, at each time step, an event occurs, without refutations.

Ordinary events assumed to simulate the phenomena occurring in the components of a LIB cell are insertion (or deposition), deinsertion (or dissolution), and diffusion. Migration can be simulated too, for the motion of Li^+ through the electrolyte when applying an electric field. Other restrictions to the processes to be allowed may be introduced, depending on the physical nature of the phenomenon. For example, in graphite intercalation, Li^+ cannot perform interlayer jumps, since the activation energy, in this case, is too high [68]. Hence, this kind of jump is not considered in kMC simulations for perfect graphite.

A comment must be added about the calculation of the rate constants, that we stated in equation (5) in one of the most popular (Arrhenius) forms. In kMC simulations, usually, all possible events and corresponding rate constants must be foreseen before starting simulations. This is sometimes not easy and this may be a crucial weak point of this type of formulation. The form given in (5) is an outcome in several levels of theory, that we revisit shortly here. In the most basic approach, v^0 is a constant factor that is considered to be the same for processes belonging to the same type of phenomenon (i.e. diffusion), and Δ_j is an activation energy, which depends on the close environment where the process is occurring. In the case of transition state theory [69,70], the v^0 term depends on the temperature; it contains the partition functions of the initial state and the activated complex, and a factor that accounts for barrier recrossing, denominated transmission coefficient. In the more general formulation by Kramers [71], the preexponential factor accounts for the effect of solvent viscosity, γ ,on the transmission coefficient. In this case, v^0 contains γ and information on the curvature of the potential energy surface in the vicinity of the reactants and the barrier. However, in principle, Γ_j does not need to have the form given in (5) and may be obtained from any level of theory. For instance, if Γ_j were meant to represent ion transfer across an interface, it could be obtained from first-principles molecular dynamics, considering solvent motion and electron transfer.

2.3. kMC in the electrochemical environment.

In this section, we present how to adapt kMC to the electrochemical environment found in LIB cells. One of the most common expressions used to describe the rate of charge transfer (current i) at the interface between the electrode and solution is the Butler-Volmer (BV) equation [72]:

$$i = nFAk^0\left\{x\exp\left[-\frac{\alpha F(E-E^0)}{RT}\right] - (1-x)\exp\left[-\frac{(1-\alpha)F(E-E^0)}{RT}\right]\right\} \tag{9}$$

where F is the Faraday constant, A is the electrode surface, k^0 is the heterogeneous rate constant (it determines the rate of the charge transfer), x is the Li^+ occupation fraction inside the electrode material, α is the transfer coefficient (it determines the symmetry of the reaction barrier), E is the potential applied to the working electrode measured with respect to the reference electrode, E^0 is the equilibrium potential, R is the gas constant, and T the temperature. This equation is often written in terms of the overpotential $\eta = E - E^0$.

Equation (9) is suited to calculate the current at the average level, concerning the energetics of the surface sites involved in the charge-transfer reaction. Note that the factors x and $(1-x)$ represent the probabilities of finding occupied and unoccupied sites respectively, while the constant k^0 contains no information about the close neighborhood where the charge transfer reaction is taking place, representing an averaged value over the different types of surface sites occurring. However, in a microstate occurring in kMC, the local charge transfer rate should be sensitive to the detailed information involved in the individual events, following Statistical Mechanics principles.

Rickvold et al. [73,74] and other works [75] have provided a useful way to build a kMC scheme with an electrochemical background. According to this approach, the barrier heights of Equation (5) for the rate constant of each event can be constructed, yielding an environment-sensitive version of the BV approximation [72], in the framework of the transition state theory. Within this method, the energy for the transition state is obtained from the initial and final configuration states of the lattice, as described in the following.

At the electrode/electrolyte interface, two main factors modify the kinetic energy barriers for the events of Li^+ insertion/deinsertion: the local interactions and the electrode potential. We have seen in section 2.1 that these energies are provided by a Hamiltonian, which in the case of statistical averaging was introduced in a suitable assembly. In this case, this Hamiltonian is used to obtain individual rates. Sometimes it is convenient to express the Hamiltonian of Equation (3) as a grand-canonical Hamiltonian, as In Reference [76]:

$$H' = H - \mu \sum_l^{M_{if}} c_l \tag{10}$$

where H is the Hamiltonian of Equation (3), while the second term on the right-hand side considers the chemical potential, μ, and the influence on the M_{if} sites located at the interface. As already seen, if the reference electrode is Li / Li^+ the Li chemical potential is related with the electrode potential $\mu = -eE$.

The proposal of reference [77] is to calculate the transition state energy barrier, ${\Delta^*}_{i/d}$, using the Hamiltonians of the initial and final configurations of the lattice (${H'}_I$ and ${H'}_F$), as follows:

$${\Delta^*}_{i/d} = {\Delta^0}_{i/d} + \frac{({H'}_I + {H'}_F)}{2} \tag{11}$$

where ${\Delta^0}_{i/d}$ is the "bare" energy barrier, i.e., the energy barrier when the energy sum of the initial ${H'}_I$ and final states ${H'}_F$ is zero.

This is shown in more detail in Figure 7, where the activation barrier, Equation (11), is represented as a function of the reaction coordinate. The horizontal segments correspond to the lattice configurations for the initial and final states and the activated complex. Black lines are the energies of each of these states in a "bare" energy situation, thus ${\Delta^*}_{i/d} = {\Delta^0}_{i/d}$. The red lines show the impact on the transition state when the energy for the final state is lowered.

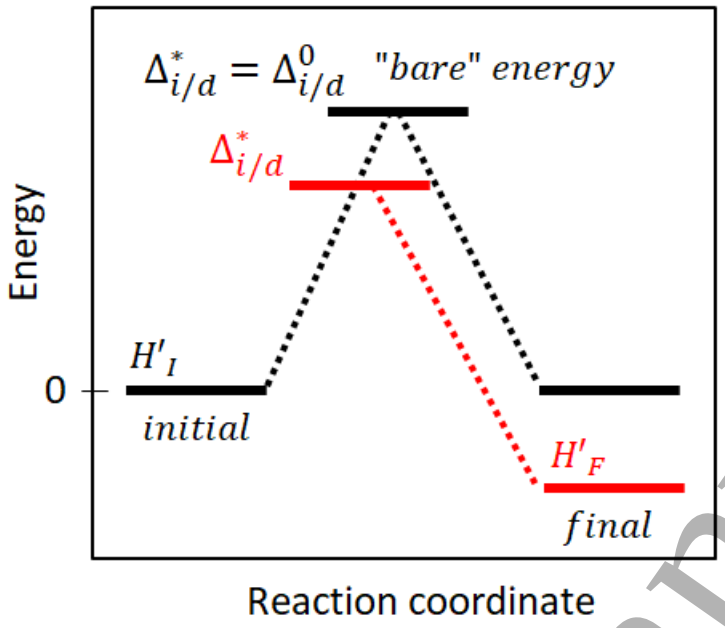

Figure 7: Energy coordinate scheme for Equation (11).

Hence, the activation barrier for going from the initial to the final state can be obtained from the energy difference between the transition state and the initial state, $\Delta_i = \Delta^0{}_{i/d} - H'_I$. Placing this expression into the equation of the rate constant, Equation (5), yields:

$$\Gamma_j = v^0 exp\left[-\frac{\Delta^0{}_{i/d}}{k_B T}\right] \exp\left[-\frac{H'_F - H'_I}{2k_B T}\right] \quad (12)$$

The current corresponding to each event is obtained by the product of Γ_j with the elemental charge e. v^0 is considered the same for all rate constants.
So, the total current is obtained by counting the insertion/removal events at the interface:

$$i = e\left(\sum_j^{N_d} \Gamma_j{}^d - \sum_j^{N_i} \Gamma_j{}^i\right) \quad (13)$$

Where $\Gamma_j{}^d$ accounts for the oxidative (deinsertion) rate, $\Gamma_j{}^i$ for the reductive (insertion) rate, N_d is the number of removal events and N_i is the number of insertion events.
Alternatively, the current can be calculated from the occupation of Li^+ intercalated in the material:

$$i = Q\left(\frac{dx}{dt}\right) \quad (14)$$

Where x is the lattice occupation, ranging between 0 and 1, t is the time and Q is the charge corresponds to the full material occupation (i.e. all of the sites being occupied).
Diffusion is also an activated process, so that the rate constant for the hopping jumps is equivalent to that of Equation (12), except for the fact that the chemical potential is no longer present in

transport phenomena within the material. In this situation $H' = H$, and the insertion/deletion "bare" barrier ${\Delta^0}_{i/d}$ must be replaced by the diffusional "bare" barrier ${\Delta^0}_{diff}$:

$$\Gamma_j = v^0 \exp\left[-\frac{{\Delta^0}_{diff}}{k_B T}\right] \exp\left[-\frac{{H'}_F - {H'}_I}{2k_B T}\right] \quad (15)$$

Other events, like the side reactions to form the solid electrolyte interphase (SEI), may be addressed when necessary.

Mesoscale kMC schemes

As discussed below, SEI formation may be included in the modeling using a mesoscale approach [78]. Here, the KMC model involves three steps. First, Li-ions and solvent adsorb on the SEI film surface near the electrolyte. Then, Li-ion and solvent diffuse through the SEI layer and reach the electrode-SEI interface. Following electron transfer, Li-ions may be reduced and then intercalate into the electrode or react with the solvent to produce new SEI. Thus, two redox systems are considered: one for Li^+ reduction and intercalation and another one for SEI formation.

Within this modeling, charge transfer for the first redox system is described by a unique equation as:

$$\Gamma = \frac{ia^2}{F} N_a \quad (16)$$

Where i is obtained with Equation (9), a is the size of one lattice site and N_a the Avogadro constant.

2.4. Testing and validation of the kMC code

Before starting the simulations for a given system, it is always healthy to test the code by making simulations for well-known systems. Thus, it is important to check if the answers of the different simulation methodologies give consistent results for the description of the same phenomenon. This will give us the confidence to later simulate the physics of more complex problems, whose analytical solutions are unknown.

In the first place, if kMC is correctly replicating the microkinetic events of a system, the overall behavior of a collection of free-wandering particles must coincide with the analytical solutions of Fick's laws at the continuum level.

To check the connection of kMC with Fick's law we can take a simple scenario: an infinite one-dimensional slab of intercalation material, having an initial uniform occupation degree x_0 occupying a portion of size l in the center of the slab, Equation (18). The diffusion equation for this system is:

$$\frac{\partial x(r,t)}{\partial t} = -D\left(\frac{\partial^2 x(r,t)}{\partial r^2}\right) \quad (17)$$

Where the occupation at $t = 0$ is:

$$x(r,0) = \begin{cases} x_0 & if\ |r| \le l/2 \\ 0 & if\ |r| > l/2 \end{cases} \quad (18)$$

The analytical solution for this problem is well known [79]:

$$x(r,t) = \frac{\theta_0}{2}\left[\mathrm{erf}\left(\frac{\frac{l}{2}+r}{2\sqrt{Dt}}\right) - \mathrm{erf}\left(\frac{\frac{l}{2}-r}{2\sqrt{Dt}}\right)\right] \quad (19)$$

Here $\mathrm{erf}\,(\mathrm{y})$ is the error function. Thus, fixing the initial occupation x_0, D and l, we can use equation (19) to calculate the evolution of lattice occupation, $x(r,t)$, with time.

To connect this with kMC simulations, let us consider the diffusion of noninteracting particles, where we have the following relationships [80]:

$$D = \Gamma(x)\lambda^2 \quad (20)$$

$$\Gamma(x) = \Gamma(0)(1-x) \quad (21)$$

$$\Gamma(0) = v^0 e^{-\Delta/k_B T} \quad (22)$$

Here, $\Gamma(x)$ is the coverage dependent diffusion rate, λ is the jump distance between diffusion sites, and $\Gamma(0)$ is the diffusion at zero occupation, which is calculated from the prefactor v^0 and Δ. With an arbitrary choice of some of these parameters, $v^0 = 1$, $\lambda = 1$, $k_B T = 1$, $\Delta = 2$, we get using equations (20-22) a value of $D = 0.1218$. Thus, we can compare the results of a kMC simulation using $\Gamma(0)$ as the transition rate, with the corresponding results from equation (19). For the initial occupation and system size, we used $x_0 = 0.1$ and $l = 14$, respectively. $N = 28$ diffusing particles were located at the center of the box at time, $t = 0$, and multiple occupancies of the sites were not allowed. Periodic boundary conditions were applied in one dimension.

To account for statistics, 250 different samples were used (less than 5 minutes of real simulation time in a single core, on a regular laptop with an Intel® Core™ i7-4710MQ processor (cache 6 MB, clock speed 2.50 GHz) with 8 GB RAM.

Figure 8, shows the results for the normalized occupation profiles x/x_0 at three different times, obtained with the continuum analytical solution, Equation (19), (red line), and the results from the atomistic kMC simulations (white dots). The changes of x/x_0 with time are the same in both cases and the diffusion coefficient obtained with kMC from the mean-square displacements was $D = 0.1218$. This shows the agreement of the simulations with the analytical solutions. The noise of kMC data can be smoothed with more statistics.

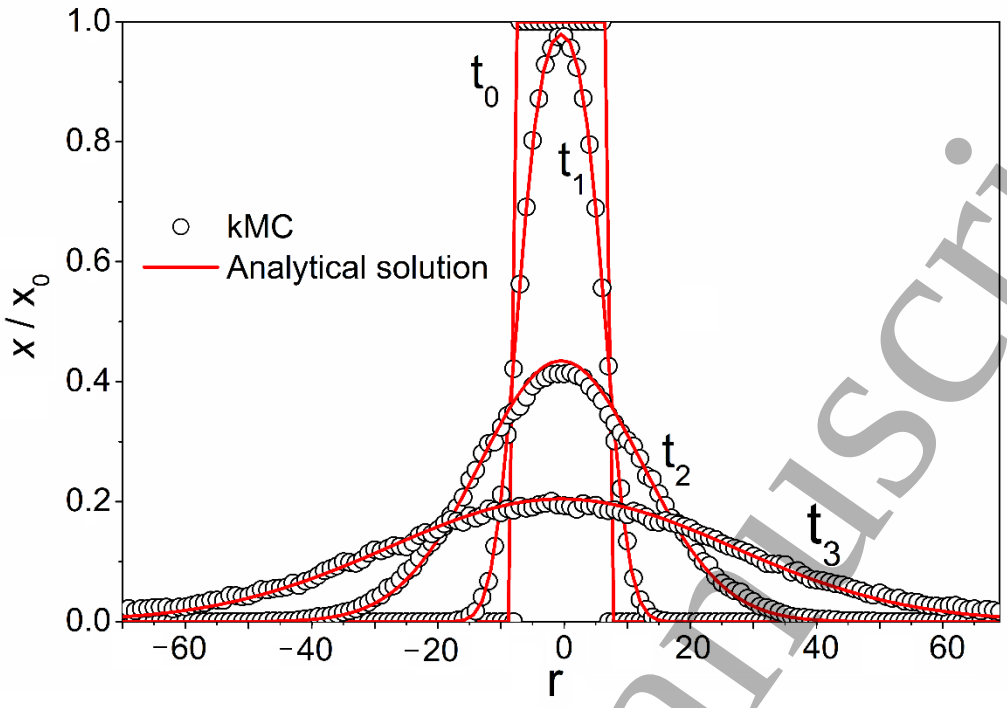

Figure 8: Comparison between concentration profiles given by the Fickian prediction, equation (19), and a kMC simulation, for the diffusion of non-interacting particles. The initial profile (t_0) is made of a constant concentration of particles concentrated at the center of the simulation box. The other profiles correspond to different diffusion times ($t_1 < t_2 < t_3$)

In the case of the electrochemical environment and in the particular case of intercalation systems, the overall behavior of electrodes depends not only on the diffusion of ions (i.e. Li^+) but also on their exchange at the electrode/solution interphase. These events are affected by kinetic-thermodynamic factors, coupled with the operating conditions of the experiment. When trying to approximate a particular theoretical model to complex experimental scenarios, such as those of lithium-ion batteries, it is important to rely on solid foundations, which are usually formulated via a set of differential equations. This connection with the theory at the continuum level is a crucial point to validate the use of kinetic Monte Carlo.

A simple and suitable scenario, considering the overall-electrode intercalation events, is that of the theory developed by Montella [81]. This author has derived theoretical expressions to explore ion diffusion, charge transfer, and the impact of the ohmic drop on the current, for the insertion of non-interacting ions in electrode slabs when applying potentiostatic steps. In such work, he found that the current response vs time depends on a dimensionless kinetic factor Λ, Equation (23), related to the diffusional R_{diff}, charge transfer R_{ch} and ohmic drop R_{Ω} resistances.

$$\Lambda = \frac{R_{diff}}{R_{ch}+R_{\Omega}} \tag{23}$$

This equation relates the effect of charge transfer/ohmic drop relative to diffusion kinetics. A small Λ value means a small contribution of charge transfer/ohmic drop to overall kinetics as compared with diffusion, and vice versa.

The theoretical framework also includes the Cottrellian current (I_{cott}) and the diffusion time constant (τ) in the dimension of the length L:

$$I_{cott} = \frac{\Delta Q}{\sqrt{\pi t \tau}} \quad (24)$$

$$\tau = \frac{L^2}{D} \quad (25)$$

where ΔQ is the total amount of charge transferred to the electrode when applying the potential step, D is the diffusion coefficient and L the distance between the electrode/electrolyte interface and the edge of the electrode.

Gavilán-Arriazu et al. [82], obtained Λ by adapting Montella´s conditions to a lattice-gas kMC scheme for non-interacting particles, using the fundamental rate constant equations and neglecting the ohmic drop from Equation (23). The result was:

$$\Lambda = \frac{|\Gamma_i d_s|}{D_y / L_y} \quad (26)$$

In this expression, Γ_i is the rate of particle insertion, d_s the (volume/surface) ratio of the unit cell where a particle is inserted, D_y the diffusion coefficient along one of the axes (*y*) and L_y is the distance in the *y* axis between the electrode/electrolyte interface and the edge of the electrode.

Figure 9a shows I/I_{cott} vs $\log(t/\tau)$ plots obtained from kMC simulations for potential steps. This representation presents a maximum when changing Λ from very high values (pure diffusional control without the maximum), to lower Λ values, as highlighted by Montella in figure 7 from reference [81]. Figure 9b shows the current maxima from Figure 9a, max I/I_{cott} as a function of Λ, compared with the results from reference [82] (white dots). An overlap between both approximations is satisfactorily observed, indicating agreement between kMC and the continuum simulation results of Montella.

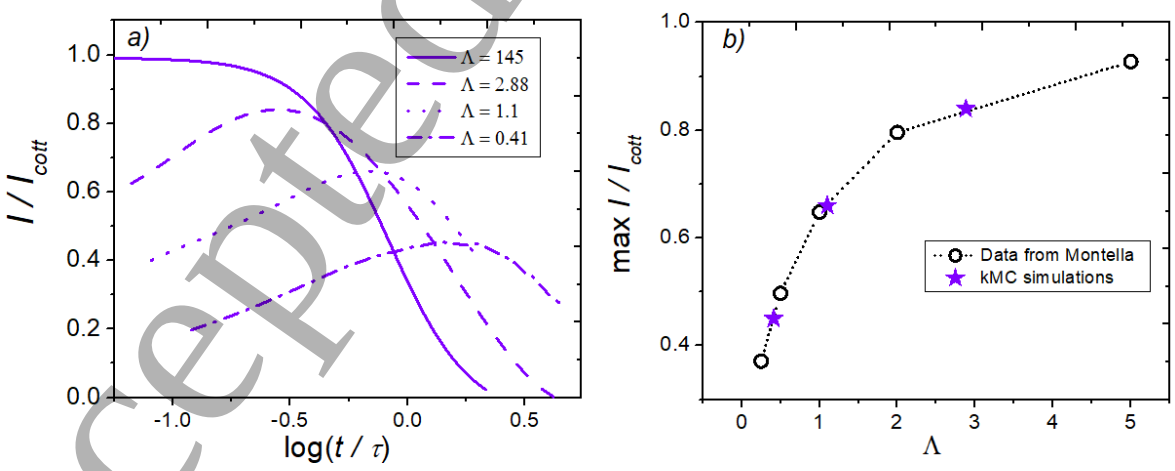

Figure 9: (a) I/I_{cott} vs $\log(t/\tau)$ plots for different Λ.(b) Comparison between kMC (stars) and continuum simulations (empty circles) for I/I_{cott} maxima (obtained from I/I_{cott} vs $\log(t/\tau)$ plots). Continuum results points were extracted from reference [81]. Reproduced with permission from ref [82]. Copyright 2020 Elsevier Ltd.

3. Ion transport in bulk electrodes

3.1. Introduction

Solid-state diffusion of Li^+ is considered one of the most important kinetic phenomena occurring during intercalation processes in LIBs, since it regulates the loading rate of Li^+ inside the electrode [83,84]. The chemical or Fickian diffusion coefficient (D_{Li}) is generally the parameter used to characterize the transport phenomena of the ionic species within the intercalation material. At small enough D_{Li}, ion transport may become relatively slow as compared with charge transfer at the electrolyte/electrode interface. Under these conditions, ion diffusion will become the rate-determining step, and mass transport will determine the charge/discharge rate of the cell.

Diffusion coefficients in LIBs electrodes are between ≈ 10^{-5} and 10^{-18} $cm^2.s^{-1}$ [85], indicating that diffusion may have an important kinetic influence. So, understanding diffusion in depth is one of the keys to improving the performance of battery materials.

The scenario may be even more complicated, since D_{Li} depends on the state of charge, varying by several orders of magnitude depending on the Li^+ concentration. This behavior is characteristic of each intercalation material. This is so because crystal structure alterations of the substrate during intercalation and other local factors have a pronounced influence on transport kinetics.

Determining D_{Li} experimentally presents several complications. It could be expected that different techniques [86], like cyclic voltammetry (CV) [87,88], potentiostatic intermittent titration technique (PITT) and galvanostatic intermittent titration technique (GITT) [84,89], electrochemical impedance spectroscopy (EIS) [84] and potential relaxation technique (PRT) [90] should give similar D_{Li} values. However, this is not the case, since different methods yield D_{Li}s that differ by two orders of magnitude or more [83–85,91,92]. These discrepancies have been attributed to assumptions made for some of the parameters needed by the different methods to calculate D_{Li}, and the difficulties in knowing the cross-sectional area of the particles, or to the occurrence of other relaxation processes that are involved in addition to solid-state diffusion, like slow charge transfer, Li^+ diffusion in pores, complex Li^+ migration processes through surface films, etc. The occurrence of different phases at different loadings of the material is a further source of uncertainty, with common models assuming an ideal solid solution and neglecting ordering in the lattice. Some new techniques have been proposed in the last years to study this phenomenon [85,93–95]. For these reasons, the support of computational simulations providing accurate calculations, without measurement uncertainties, may help and complement experimental techniques, revealing how diffusion mechanisms operate. This is important to know what are the factors that affect diffusion kinetics and thus what can be done to improve the characteristics of LIBs. In this regard, kMC may provide detailed information on Li^+ diffusion phenomena.

A relevant equation to study Fickian's diffusion using computer simulations is the Kubo-Green formula [79]:

$$D_{Li} = \Theta D_j \tag{27}$$

that relates the chemical diffusion coefficient D_{Li} with the thermodynamic factor Θ. The latter is defined in terms of the chemical potential μ and the lithium composition:

$$\Theta = \left(\frac{\partial(\mu/k_BT)}{\partial lnx}\right)_T \tag{28}$$

D_j in equation (27) is the jump-diffusion coefficient, related to the square of the displacement of the center of mass of N Li^+ particles

$$D_j = \lim_{t\to\infty}\left[\frac{1}{2dt}\left\langle\frac{1}{N}\left(\sum_{i=0}^{N}\Delta r_i\right)^2\right\rangle\right] \quad (29)$$

In this expression Δr is the displacement of a Li^+ ion from an initial point, t is time and d is the system dimension.

Alternatively, it is possible to obtain the tracer diffusion coefficient D^* , associated with the mean-square displacement of the individual Li^+

$$D^* = \lim_{t\to\infty}\left[\frac{1}{2dtN}\sum_{i=0}^{N}\langle(\Delta r_i)^2\rangle\right] \quad (30)$$

3.2. Cathodes LMO-LCO- $LiFePO_4$

An early model devoted to describing diffusion transport in bulk electrodes was developed in 1999 by Darling and Newman [96]. These authors investigated Li^+ diffusion in $Li_yMn_2O_4$ cathodes with a fraction of pinned Li, ranging between 0 % and 40%. They implemented a lattice-gas model defined by the 8a sites of the LMO structure (Figure 10a), using a Hamiltonian with short-range interactions adapted from the original Bragg-Williams approximation developed by Gao et al. [97]. The kMC procedure used by these authors used energy barriers for diffusion obtained experimentally. With this work, they showed how the diffusion coefficient changes with Li^+ concentration and how pinned lithium sites affect diffusion transport (Figure 10b).

Later on, Kim and Pyun [46] also investigated Li^+ thermodynamics and diffusivity in $Li_yMn_2O_4$ cathodes with kMC, using an interaction Hamiltonian similar to that of Darling [96]. In this work, the authors found agreement between the model predictions for the variation of D_{Li} with Li^+ composition and experimental GITT diffusion coefficients (Figures 10c and d). With these results, Kim and Pyum showed how the thermodynamic factor (W in Figure 10c and d) dominates the behavior of the chemical diffusion coefficient (Figure 10c and d), as compared with the jump-diffusion coefficient (Figure 10c and d). Moreover, the authors also showed the coincidence between the partial molar entropy obtained with MC simulations and experiments. A year after the work of Darling et al., Van der Ven and Ceder [65] calculated D_{Li} for the Li_xCoO_2 cathode (LCO) with kMC, using energy barriers obtained from DFT calculations for two different migration pathways (Figure 10e), instead of experimental data. These authors found agreement with experiments for Li^+ concentrations lower than 95%. The differences for high concentration values were attributed to the use of two fixed activation energies, without considering Li-Li interactions to capture the atomistic-level details. Ionic configurations were then considered to calculate D_{Li} (Figure 10f) in Li_xCoO_2 by Van der Ven et al. [98], implementing a local cluster expansion [99], combined with DFT, to obtain the energy barriers for diffusion in Li_xCoO_2. This work demonstrated the strong influence of Li^+ concentration on energy barriers, and so on kinetics. With a similar simulation strategy, the dependence of D_{Li} on Li^+ concentration was investigated in Li_xTiS_2 [100] and $Li_{1+x}Ti_2O_4$ [101].

Liu et al. [102] treated Li^+ diffusion in $LiFePO_4$ cathodes by considering Li-Fe antisite defects (in crystallography, an antisite defect is formed when atoms/ions exchange places [103]). This phenomenon is difficult to study experimentally, due to the low concentration of these defects. Comparison between solid-state NMR measurements and kMC simulations demonstrated the importance of considering antisite defects for Li^+ diffusion transport in $LiFePO_4$.

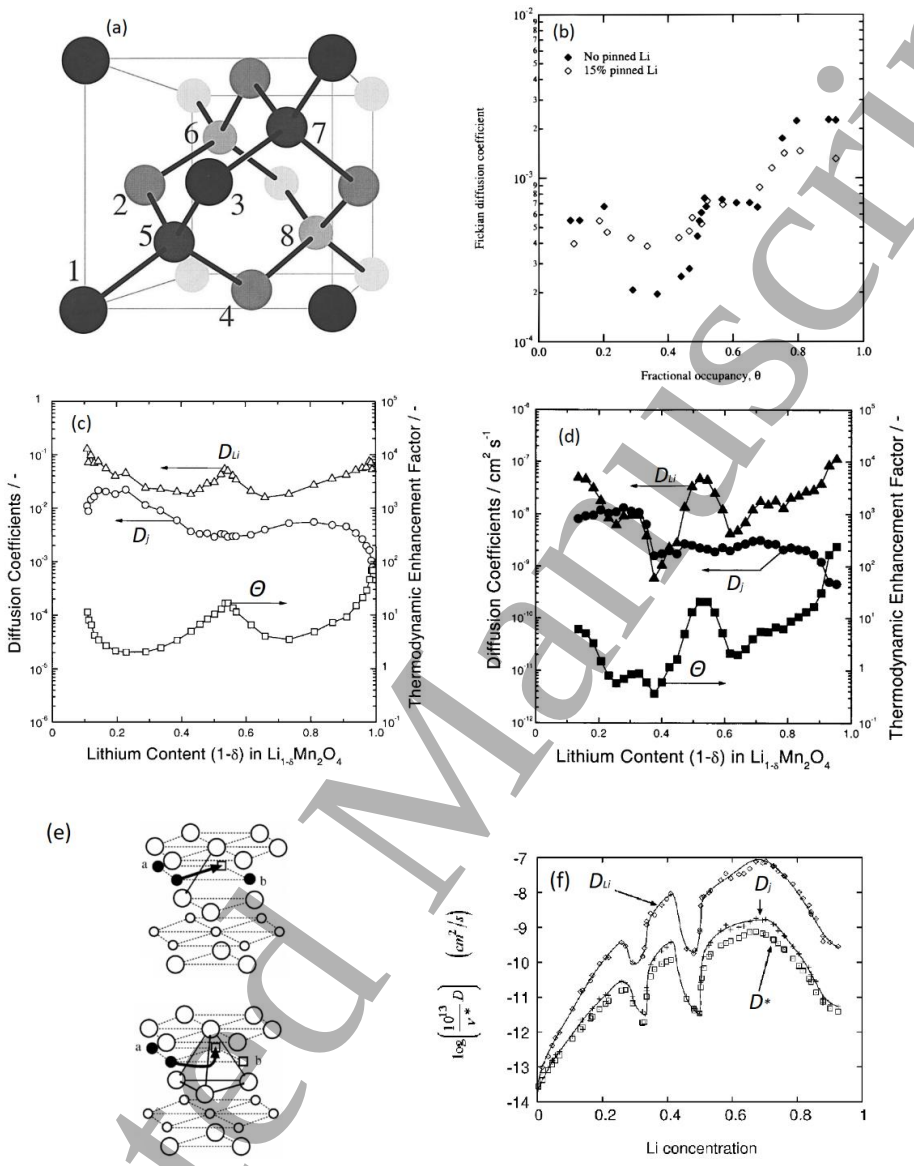

Figure 10: (a) Unit cell for $Li_yMn_2O_4$ showing intercalation sites. Sites 1-4 are from one of the fcc sublattices, while sites marked with 5-8 correspond to the other sublattice (the two sublattices together, representing all available Li sites, comprise a diamond lattice). (b) Fickian diffusion coefficients for pinned and unpinned $Li_yMn_2O_4$ for different Li occupancy values calculated with kMC. Reproduced with permission from ref [96]. Copyright 1999 The Electrochemical Society. (c) kMC Diffusion coefficients D_{Li} and D_j, and thermodynamic factor for LMO considering blocking sites. (d) Experimental D_{Li}, D_j and thermodynamic factor. Reproduced with permission from ref [46]. Copyright 2001 Elsevier Ltd. (e) Two diffusion mechanisms in $LiCoO_2$, Large circles are oxygen, black circles are Li^+, squares are lithium vacancies and small empty circles are cobalt. (f) Chemical (D_{Li}), jump (D_j) and tracer diffusion coefficients calculated for $LiCoO_2$. Reproduced with permission from ref [98]. Copyright 2001 The American Physical Society.

3.3. Anodes. TiO_2 – Graphene-Graphite-Silicon

Yu et al. [104], used kMC to study Li^+ diffusion in TiO_2 of different grain sizes, coupling Li^+ and electron-polaron (e^-) diffusion to understand charge transport in nanosized systems. According to this work, conductivity is determined by Li^+ diffusion, which is slower than electronic motion. They also investigated the role of the surface of the conductive contact material with the electrode, in this case, a carbon matrix, finding higher Li^+ diffusion rates for small surface areas. Activation energies were obtained from references [105,106] and the pre-exponential factor was taken from reference [107].

The kinetics and energetics of Li^+ diffusion in crystalline (c-Si) and amorphous silicon (a-Si) anodic materials were studied by Moon et al. [108], with DFT and kMC atomistic simulations. The formation energies of Li-Si in c-Si and a-Si were calculated using DFT, with the finding of a two-phase coexistence for lithiated c-Si and the occurrence of only one-phase for lithiated a-Si. DFT calculations of the diffusion energy barriers (Figure 11a) and the kMC kinetic study for different Li concentrations showed that diffusion coefficients are higher in a-Si as compared with c-Si. Similar conclusions were reached by Chang et al. [109] using Molecular dynamics to elucidate the diffusion pathways and kMC to obtain Li diffusivity for different Li concentrations, energy barriers were calculated using the climbing image nudged elastic band method (CI-NEB) [110] and the pre-exponential factor was taken from reference [111]. The results show that initially in a-Si the diffusivity increases with Li concentration, but above a limiting concentration, Li intercalation reduces D by blocking the diffusion pathways. Regarding Si anodes, Yan et al. [112] combined the Autonomous Basin Climbing (ABC) method, for sampling the potential energy surface of the material, together with the Nudged Elastic Band (NEB) method for calculating energy barriers from all the energy minima pairs obtained with ABC, and kMC to estimate Li^+ diffusion pathways in amorphous Si. This technique allowed the authors to reproduce the mixture of diffusion coefficients observed experimentally. A similar activation-relaxation technique [113] coupled with the Reactive Force Field (ReaxFF) with parameters from [114] was used by Trochet et al. [115] to study Li^+ diffusion in c-Si at low concentrations, showing the importance of Li interactions in favouring clustering, promoting the high concentration phase of Li. Kinetics and energetics in Li-Si binary compounds (LiSi, $Li_{12}Si_7$, $Li_{13}Si_4$, and $Li_{15}Si_4$) were then investigated by Moon et al. [116] using the climbing image nudged elastic band (NEB) to calculate the energy barriers. Lower migration barriers, of about two orders of magnitude, were obtained for all binary compounds as compared with crystalline Si. These results showed that the kinetic bottleneck is the initial lithiation of the Si anode. A previous multi-scale analysis using DFT, continuum calculations and kMC simulations for pre-lithiated Si nanowires delivered the same conclusions [117].

Turning to carbonaceous systems, Zhong et al. have studied the Li^+ kinetics of diffusion on graphene [118]. Energy barriers were calculated within DFT for single and two Li atoms adsorbed on a graphene sheet (Figure 11b and c), to investigate the concentration and temperature dependence of diffusion coefficients using kMC. A similar simulation approach was developed by Zhong et al. [119] to determine the energetics of Li^+ diffusion in bilayer graphene.

Persson et al. [64] have investigated the dependence of D_{Li} on Li^+ concentration by kMC, obtaining energy barriers from first-principles calculations and using a mean frequency of jumps (v^0) calculated in reference [120]. They have constructed a theoretical phase diagram for lithium-graphite intercalation compounds (LGIC) using first-principles / MC simulations. They also predicted the existence of new stages at elevated temperatures. A similar phase diagram was then found from the analysis of *in situ* X-ray diffraction patterns [121].

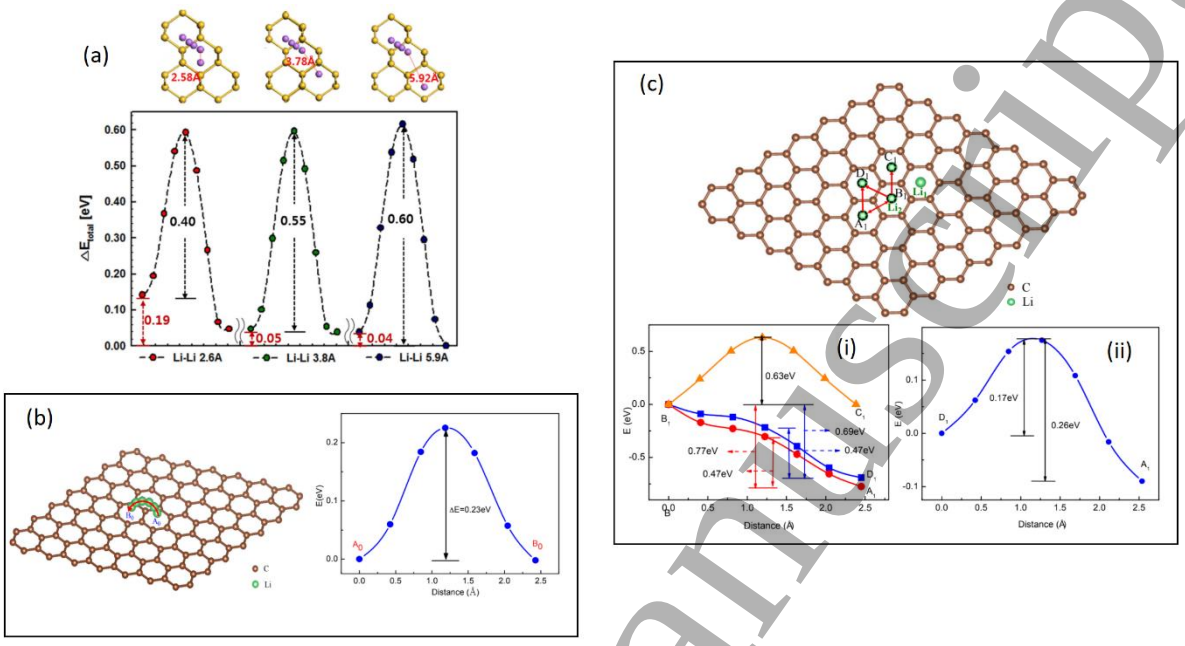

Figure 11: (a) DFT energy barriers for two Li^+ ions separated by three different distances in Si. One of the Li^+ ions migrates while the other remains fixed on the same point of the lattice. Reproduced with permission from ref [108]. Copyright 2014 Elsevier B.V. (b) Activation energy with DFT for the diffusion of one Li^+ on a graphene sheet. (c) Different paths (B1-A1, B1-C1, B1-D1, A1-D1) for the migration of one Li^+ while the other remained fixed. (i) Energy barriers for paths B1-A1, B1-C1, B1-D1. (ii) Energy barriers for path A1-D1. Reproduced with permission from ref [118]. Copyright 2017 MDPI.

The thermodynamic factor Θ is generally obtained from MC simulations, which reproduce equilibrium open-circuit voltage (OCV) conditions. However, in intercalation systems where a phase transition involves phase coexistence, the calculation of Θ with grand canonical MC is complicated. This is so, because the change of x with μ is infinitely steep in the case of a first order transition, and so the expression to determine Θ is not properly defined. An example of this is Li^+ (de)intercalation in graphite, where the equilibrium isotherm shows discontinuous jumps of x for the transition between stages [37,48], which can be modelled with effective in-plane attractive interactions. For such reasons, an alternative calculation of Θ was proposed by Gavilán-Arriazu et al. [82], to account for regions of phase coexistence. Instead of equilibrium MC simulations, they implemented kMC simulations in such a way as to reproduce experimental cyclic voltammetry (CV-kMC) conditions at very slow sweep rates. This quasi-equilibrium situation was used for the calculation of Θ from the simulated CV isotherms. Then, D_{Li} was obtained applying equation (28) and using Θ and the ordinary calculation of D_j within the NVT ensemble according to equation (29).

These authors implemented this methodology for Li^+/graphite. In such a model, the kinetic barrier Δ^0_{diff} for diffusion was fitted to get the experimental D_{Li} in the dilute Li^+ limit [84], where interactions can be neglected, as in a random walk scenario. Interactions were treated with a Hamiltonian fitted to yield a typical experimental isotherm [48]. The corresponding Θ and the isotherm for a CV-kMC simulation are shown in Figure 12a. The chemical diffusion coefficients D_{Li}

(full red circles) and jump-diffusion coefficients D_j (white squares) obtained are shown in Figure 12b, for room temperature ($T = 296$ K). An overall good agreement with experimental D_{Li} results obtained with PITT experiments can be noted [84]. The coincidence between theory and experiment is satisfactory, especially taking into account the complexity of the experimental system.

Previous work by Gavilán-Arriazu et al. [122] showed that metastable Daumas-Hérold structures (consisting of islands of Li^+ present in all graphite planes) frustrate the Li^+/graphite system from reaching thermodynamic equilibrium; the work of Mercer et al. [47], also shows the importance of metastable structures in Li^+ intercalation hysteresis observed in graphite. Thus, even experimental measurements conducted under extremely slow GITT conditions with relaxation times on the order of several hours do not reach thermodynamic equilibrium, but should rather reflect the metastable dynamics inherently present in kMC simulations [47].

With the same strategy, Gavillan-Arriazu et al. analyzed the influence of temperature on diffusion phenomena for the lithium/graphite system [123] (Figure 12c). They found that an increase in temperature increases diffusion coefficients for all lithium compositions. The same behavior has been observed experimentally [124,125]. Furthermore, the calculation from Arrhenius plots of energy barriers for diffusion (Figure 12d) at different states of charge demonstrates that the formal activation barrier changes with Li^+ concentration. The activation energies for Li^+ diffusion at different lithium occupations inside graphite (x) are included in Figure 12e

The effect of strain effect on Li^+ diffusion in graphite during intercalation has been investigated by Ji et al. [126] using DFT and kMC. Their results show how tensile strain perpendicular to graphite planes and compressive strain parallel to these planes accelerate Li^+ diffusion rates.

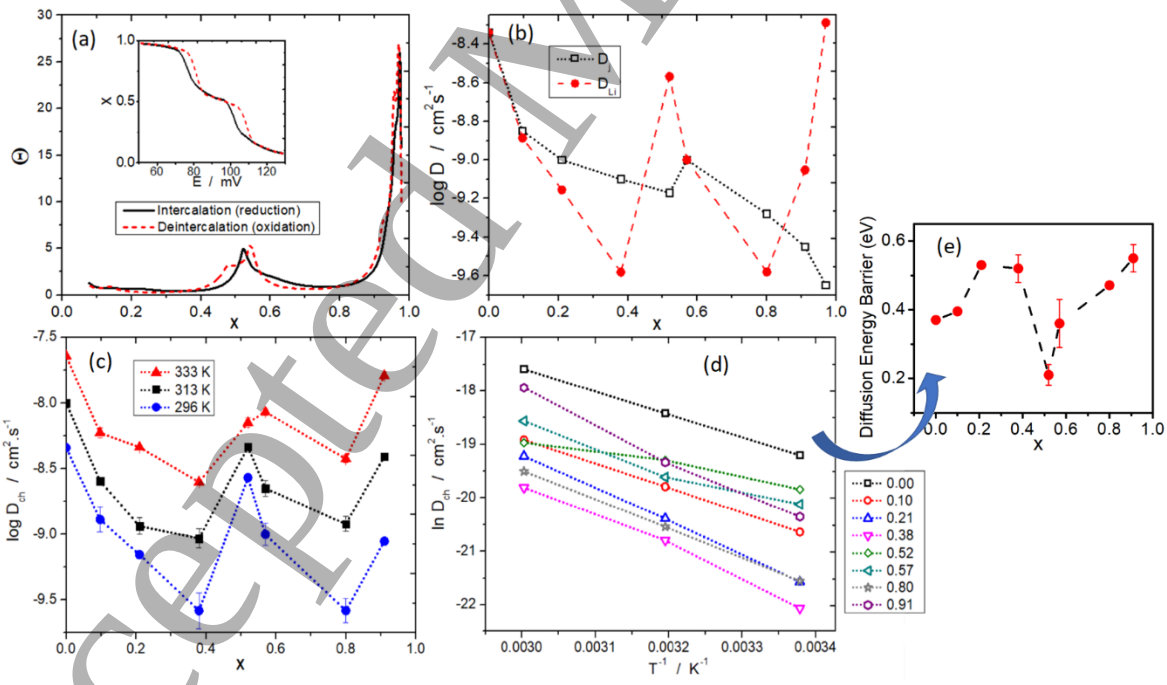

Figure 12: Results from kMC simulations for Li^+ intercalation in graphite. (a) the thermodynamic factor for intercalation and deintercalation obtained from kMC simulations of cyclic voltammograms at slow sweep rates at 296 K, the inset shows the corresponding isotherms. (b) D_{Li} and D_j , as given by equations (26) and (28) for different Li^+ occupations. Reproduced with permission from ref [82]. Copyright 2020 Elsevier Ltd. (c) D_{Li} vs Li^+ occupation for 296 K (blue circles), 313 K (black squares), and 333 K (red triangles). (d) Arrhenius plots for diffusion coefficients at different Li^+ occupations,

lines were drawn to guide the eye. (e) Activation energies for Li^+ diffusion at different x. Reproduced with permission from ref [123]. Copyright 2020 The Electrochemical Society.

3.4. Validation of KMC diffusion coefficients by step-isotope-exchange

Very recently, experimental work has used the step-isotope-exchange method together with secondary ion mass spectrometry (SIMS) analysis and PITT to obtain D_{Li}, D_j D^* and Θ for Li^+ diffusion in $LiMn_2O_4$ [95] and $LiCoO_2$ [127] thin films of different thicknesses. In particular, these techniques allowed the tracer diffusion coefficient D^* to be calculated directly. D_{Li} was obtained from PITT measurements and D_j was derived from it using the thermodynamic factor, according to Equation (27). The step-isotope exchange consists of the use of an electrolyte enriched with the isotope ^6Li. This isotope is allowed to exchange with the most abundant Li^+ isotope of the cathode, and the time evolution of the ^6Li concentration inside the electrode is quantified. With stepwise dipping, different isotope concentrations are recovered for the different regions of the sample (Figure 13a). The results of this work supported outcomes from previous simulations [46]. For example, Figures 13b and c show experimental results that can be compared with the kMC results previously shown in Figure 10c, $LiMn_2O_4$. The authors arrived at remarkable conclusions, like the great contribution of the thermodynamic factor to D_{Li} (predicted by simulations) and the key role of Li-Li interactions in the diffusion mechanism. Results for $LiCoO_2$ are also shown in (Figures 13d and e). Hence, this experimental methodology combined with kMC simulations presents an attractive and exhaustive tool to analyze in-depth Li^+ diffusion in different materials.

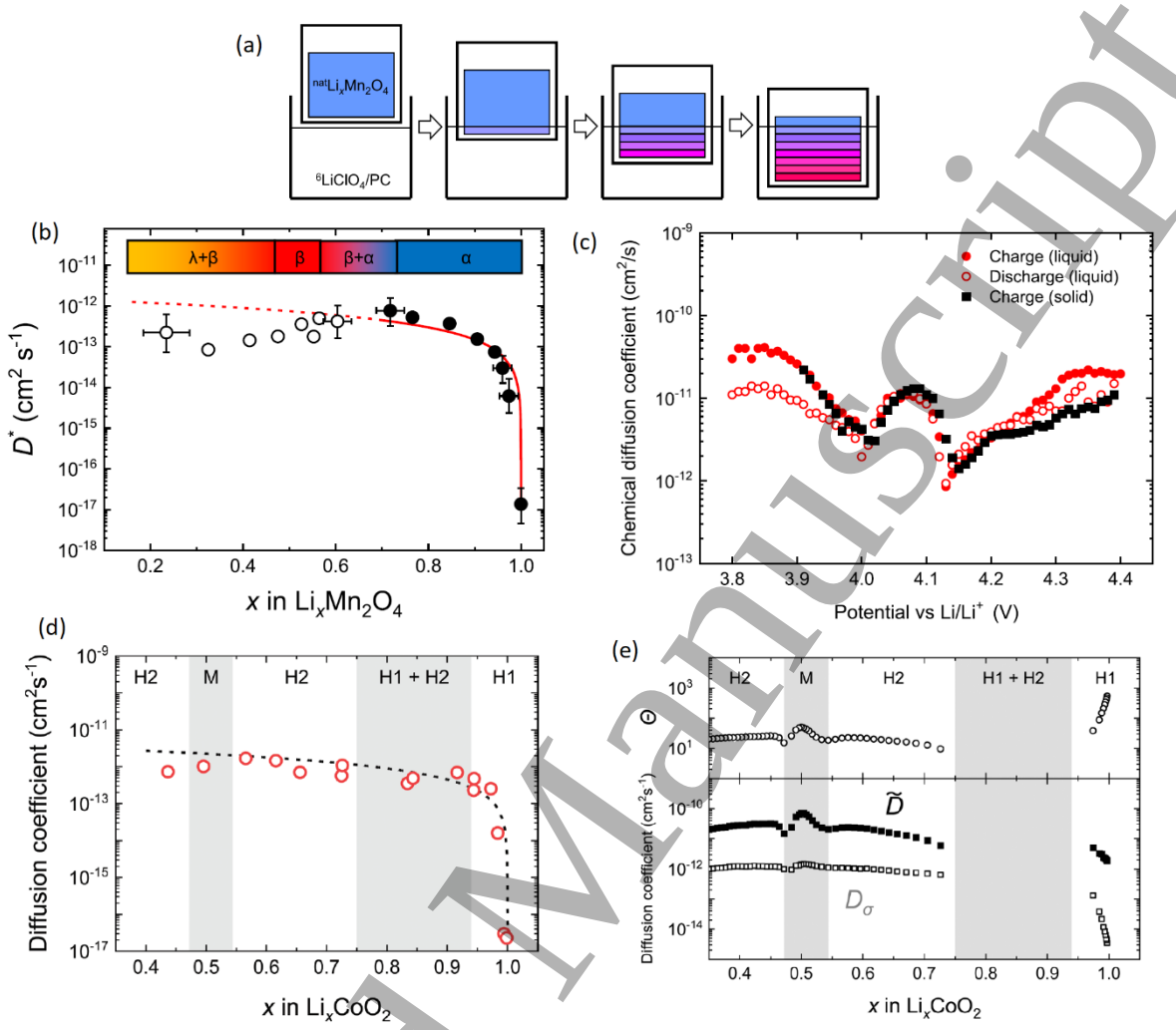

Figure 13: (a) Schematic view of the step-isotope-exchange method. A thin film of intercalation material is immersed in a ^{6}Li enriched electrolyte with different stepwise dippings; different immersion times produce regions with different isotope concentrations, as shown in colors. Reproduced with permission from ref [95]. Copyright 2020 American Chemical Society. (b) Tracer diffusion coefficient obtained with the step-isotope-exchange method for $LiMn_2O_4$. The inset shows the different phases formed during intercalation. Full circles correspond to tracer diffusion coefficients for the α-phase, while open circles correspond to those for the β-phase. Reproduced with permission from ref [95]. Copyright 2020 American Chemical Society. (c) Chemical diffusion coefficients obtained with PITT for $LiMn_2O_4$ vs electrode potential, red circles correspond to a liquid electrolyte and black circles to a solid electrolyte. Reproduced with permission from ref [95]. Copyright 2020 American Chemical Society. (d) Tracer diffusion coefficient obtained with the step-isotope-exchange method for $LiCoO_2$ (red open circles), the dashed line corresponds to the equation for the vacancy diffusion mechanism. The white-grey zones correspond to different phases and phase coexistence regions. Reproduced with permission from ref [127]. Copyright 2021 The Owner Societies. (e) Thermodynamic factor, chemical diffusion coefficient (here represented as $\tilde{D}$) and jump-diffusion coefficient (here called conductivity diffusion coefficient, D_σ) calculated for $LiCoO_2$ with the step-isotope-exchange method and PITT. Reproduced with permission from ref [127]. Copyright 2021 The Owner Societies.

4. Interfacial phenomena (IP) and its coupling with diffusion

In the previous section, we discussed Li^+ diffusion phenomena and the importance of considering this kind of mass transport to analyze the intercalation of Li^+ in electrode materials and improve their performance. Another crucial phenomenon participating in electrode kinetics is charge transfer at the electrode/electrolyte interface, since it regulates the rate of Li^+ exchange between the electrode and the solution. Like diffusion, charge transfer is a slow process in Li^+ battery materials. For example, the heterogeneous rate constant in BV equation, k^0, which regulates the charge transfer rate at the interface varies several orders of magnitude (≈ 10^{-5} cm.s^{-1} – 10^{-9} cm.s^{-1}) depending on the experimental system [128–131]. This figure, together with the previous considerations regarding diffusion in section 3, indicates that the overall kinetics (charge transfer + diffusion) are slow in battery materials.

In a voltammetric experiment, if the electrochemical charge transfer reaction follows the Nernst equation, the reaction is considered to be *reversible*. On the other hand, if charge transfer is very slow as compared with the potential sweep rate, the back and forth reactions do not have time to balance, and an *irreversible* condition is reached. A reaction occurring between the limits of these conditions is denominated *quasi-reversible*. Moreover, charge transfer is coupled with diffusion, since a concentration gradient is established due to the generation/consumption of Li^+ at the electrode surface. This is why a complete model should consider both processes.

Important parameters characterizing the kinetics of electrochemical interfaces are the charge transfer resistance (R_{ch}), the exchange current density (j_o) and the activation energy (Δ) [81]. These are obtained using different experimental techniques, like chronoamperometry, chronocoulometry, cyclic voltammetry, EIS, PITT, GITT, etc. [89,132,133].

The exchange current density is defined at steady-state conditions, when the net current density j, reaches zero. Under these conditions, the forward and backward current densities are equal, i.e.:

$$j = j_a - j_c = 0 \tag{31}$$

$$j_0 = j_a = j_c \tag{32}$$

Within the Butler-Volmer description, Equation (9) leads to:

$$j_0 = nFk^0\left\{x\exp\left[-\frac{\alpha F\left(E-E^0\right)}{RT}\right]\right\} = nFk^0\left\{(1-x)\exp\left[-\frac{(1-\alpha)F\left(E-E^0\right)}{RT}\right]\right\} \tag{33}$$

Assuming $\alpha = 0.5$ and rearranging we get:

$$j_0 = nF(k^0)^{0.5}(1-x)^{0.5}x^{0.5} \tag{34}$$

In the kMC framework, equation (13) yields, counting N_i intercalation events (i) and N_d deintercalation events (d):

$$j_0 = \frac{e}{A}\left(\sum_j^{N_d}\Gamma_j^{\,d}\right) = \frac{e}{A}\left(\sum_j^{N_i}\Gamma_j^{\,i}\right) \tag{35}$$

The difference between the continuum Equation (34) and the kMC Equation (35) descriptions is that, in the first case the exchange current density always has the same dependence on Li^+

concentration, due to the averaged way in which free and occupied sites are considered (x and $(1-x)$ factors). Instead, the kMC scheme considers the summation over all the rates for the individual events, each of them dependent on the local microenvironment surrounding the sites considered, where each event may occur. Thus, in a kMC simulation j_0 depends on the crystal structure, which in turn affects the energetics of the charge transfer reaction.

However, the modelling of interfaces is particularly challenging since it requires assumptions on the atomic structures of the phases involved. Thus, surface properties such as chemical composition, crystalline structure and crystal orientation, may have a strong influence on interface kinetics. Furthermore, even in coarse-grained models, different properties of the system like dielectric constant, charge density, electric field, etc, may vary along the interface. This is not a minor issue, since these details are usually unknown, but are expected to impact the values of pre-exponential factors and activation energies. A good example of how to calculate activation energies at equilibrium potential for a complex system has been given by Haruyama et al. [134]. These authors have performed a detailed study of the reaction of Li+ at the graphite/electrolyte interface, using DFT calculations with an implicit solvation theory. Different paths for Li-ion insertion into graphite with two tilt angles were considered, finding an activation barrier next to 0.6 eV in all cases. This value was consistent with experimental measurements [135,136].

Assuming linear conditions (small potential perturbations), the overall resistance of the electrochemical cell (R_{cell}) is related to the electrode potential following Ohm's Law, as follows [137]:

$$i = \frac{|E - E_{eq}|}{R_{cell}} = \frac{\Delta E}{R_{cell}} \quad , \tag{36}$$

where E_{eq} is the initial equilibrium (steady-state) potential of the experiment and E is the applied potential. The charge transfer resistance R_{ch} is one of the components of R_{cell}. In the case of EIS experiments, the electrochemical system is often described in terms of an *equivalent circuit*, so that physicochemical phenomena are interpreted in terms of the behavior of the electronic components of a circuit. For example, Figure 14a shows a typical equivalent circuit proposed for cells using cathodes made of transition metal oxides. The fitting of Nyquist plots (output of EIS experiments) using an equivalent circuit gives the values of the different components assumed for the system.

In the kMC scheme developed by Kim et al. [137] R_{ch} is inversely proportional to the conductivity given by the thermally activated motion of ions, and is obtained from:

$$R_{ch} = wT\exp(\Delta / k_B T) \tag{37}$$

where Δ is the activation energy and w is a pre-exponential factor. This parameter can be obtained from Equation (12) or taken from the literature [123,137], for oxidation (removal) and reduction (insertion) events:

$$\Delta = \Delta^0{}_{i/d} + \alpha(H'_F - H'_I) \tag{38}$$

$$\Delta = \Delta^0{}_{i/d} + (1-\alpha)(H'_F - H'_I) \tag{39}$$

An averaged Δ for insertion/deinsertion of Li^+ can be obtained from kMC, when the simulation reaches the steady-state after applying a potentiostatic step. This parameter can also be calculated with experimental and/or kMC Arrhenius plots: $\ln(R_{ch}/T)$ vs T^{-1} or $\ln(j_0)$ vs T^{-1}.
A further important phenomenon at the electrode/electrolyte interface is the formation of the solid electrolyte interface (SEI) on the surfaces of different electrodes. This issue and others will be treated in the next section; in the present section we will focus only on Li^+ charge transfer and charge transfer coupled with diffusion.
The first kMC model devoted to lithium batteries was that of Deppe et al. [24] in 1994. It was applied to analyze the diffusion of Li^+ through the interface between an InSe cathode and a separator made of Li-doped borate glass. Simulations allowed the authors to show the influence of interactions and energy barriers on interfacial diffusion. However, no experimental measurements were reported to support the results.
Eight years later, Kim and Pyun [137] used kMC to study the cell impedance of $LiMn_2O_4$ using PITT and EIS measurements. They showed, using the equivalent circuit of Figure 14a to fit the Nyquist plot, that the major contribution to the resistance at intermediate frequencies (R_{ch}) is due to the insertion of Li^+ in $LiMn_2O_4$. So, the good agreement between the experimental activation energies obtained from Arrhenius plots of R_{ch} (Figure 14c) and the theoretical activation energies (Figure 13e) used to generate R_{ch} profiles (Figure 14d) point out the importance of the absorption/desorption kinetics on the intercalation of Li^+ in $LiMn_2O_4$ and the role of short-range interactions. They also concluded that R_{ch} is larger than the diffusion resistance. For these simulations they used $v^0 = 5\text{x}10^5\ \text{cm.s}^{-1}$ and ${\Delta^0}_{i/d} = 0.7$ eV, fitted to experiments.
The same year, Kim and Pyun performed experimental and kMC simulated potential steps and linear sweep voltammograms for $LiMn_2O_4$ [75]. The flux of Li^+ through the interface was calculated from the master equation that describes the evolution of lattice configuration with time [138]. The jump probability through the interface (W) was approximated according to $W = \kappa\left|E - E_{eq}\right|$, where κ is a conversion factor taken arbitrarily below unity. In this work, the authors showed how interactions between inserted ions affect the current transients and voltammetric profiles compared to the case without interactions. They also found that the transition from the disordered phase to the ordered phase is controlled by the flux of ions at the interface. The best correspondence with experiments was found for kMC simulations including these interactions. For example, deviations from a pure diffusional behavior were found in voltammetric and potentiostatic transients.
Later on, Jung et al. [139] analyzed with kMC the current transients for Li^+ intercalation in the region of coexistence of a Li-poor with a Li-rich phase in $\text{Li}\left[\text{Ti}_{5/3}\text{Li}_{1/3}\right]\text{O}_4$. They proposed that the wide potential plateau observed experimentally for the coexistence of these phases is due to repulsive interactions between Li ions, using a Hamiltonian with three Li-Li interaction terms.
The conductivity at different Li^+ concentrations for $LiMn_2O_4$ was calculated by Ouyang et al. [140] introducing the electric field ($\vec{E}$) in the probability equation. The latter was given by Metropolis algorithm, with $P = \exp\left[-\left({H'}_F - {H'}_I \pm \vec{E}\right)/k_B T\right]$. No pre-exponential factors were implemented. They highlighted the similarities between the behavior of this parameter and the trends observed in diffusion coefficients.

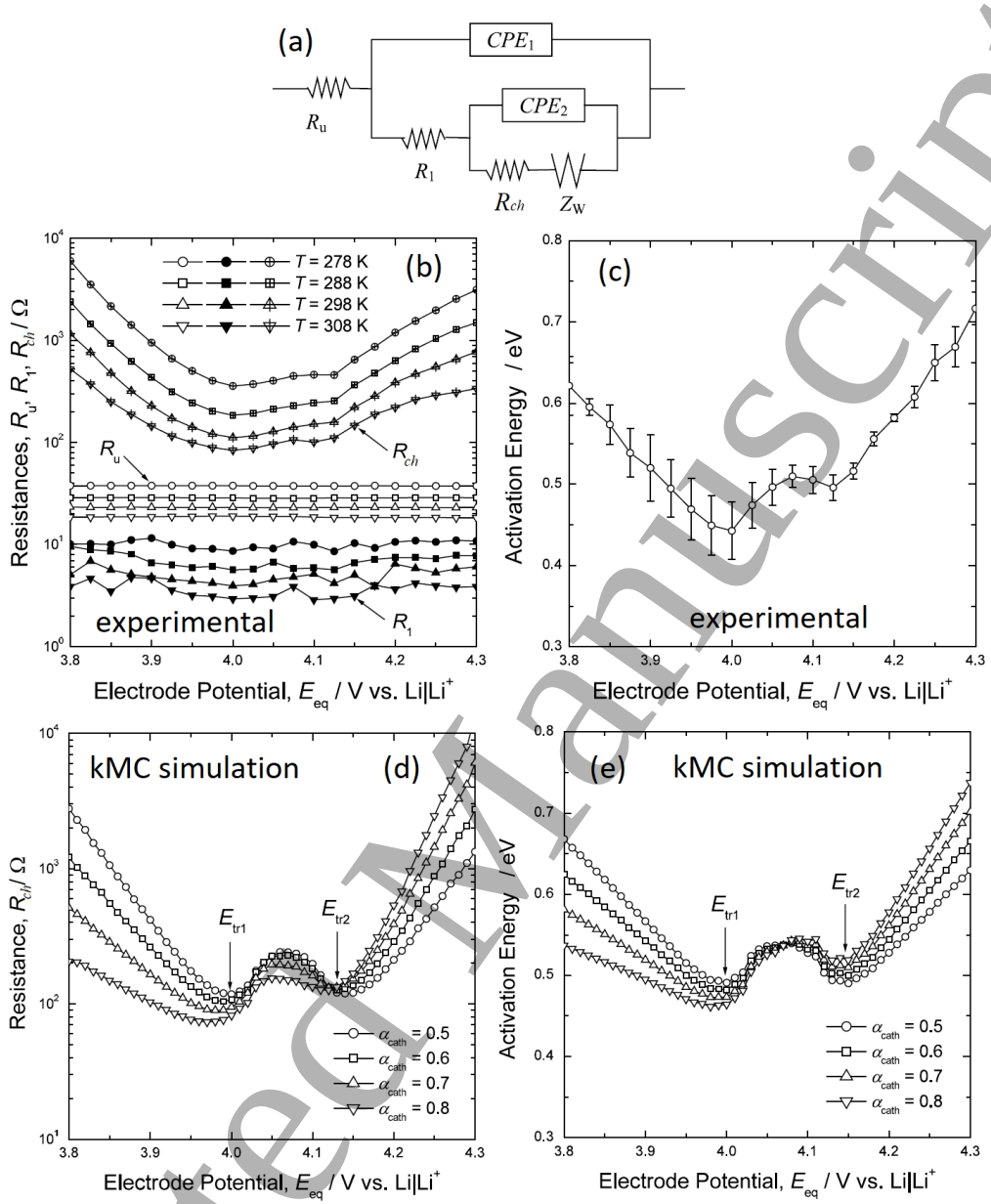

Figure 14: (a) equivalent circuit used for cathodes prepared with transition metal oxides. R_u is the uncompensated ohmic resistance of the electrolyte; R_1 the high-frequency resistance, CPE_1 a constant phase element; R_{ch} the intermediate frequency resistance and CPE_2 a constant phase element; and Z_W represents the Warburg impedance. (b) Experimental resistances of $LiMn_2O_4$ for different potentials and temperatures. (c) Activation energies calculated from experimental Arrhenius plots for $LiMn_2O_4$. (d) kMC simulations of the charge transfer resistance in $LiMn_2O_4$. (c) Activation energies used in the kMC simulations for $LiMn_2O_4$. Reproduced with permission from ref [137]. Copyright 2002 Elsevier Science B.V.

In 2011, Hin [141] simulated galvanostatic transients for a Li_xFePO_4 olivine cathode made of nanocrystals. They coupled continuum simulations for Li^+ diffusion in the electrolyte with kMC simulations for the events occurring in the electrode. The value of the Li^+ insertion/removal frequency was fitted to the data of reference [142]. Saddle-point binding energies and attempt

frequencies for diffusional jumps, were fitted to the Li^+ interstitial diffusivity tensor from reference [143].The author found an anisotropy for Li^+ insertion in particles with different orientations with respect to the flux direction of Li^+ in the electrolyte. The kMC galvanostatic curves for discharge reproduced the features observed in experiments (Figure 15a). A DFT-based kMC model was also applied to study the kinetics of phase evolution in charge/discharge processes of Li^+ in a Li_xFePO_4 cathode, as reported by Xiao and Henkelman [144].

Lithiation of crystalline silicon exhibiting {110} and {111} surfaces was studied by first-principles and kMC simulations by Cubuk et al. [145]. A pre-exponential factor of $1x10^{13}$ s^{-1} was assumed and the energy barriers for the kMC simulations were obtained from DFT calculations. The kMC simulations showed that the rates of the process are faster for {110} surfaces than for {111} ones (Figure 15b). These results and the features observed for the Li concentration depth profile inside the material, coincide with the trends observed experimentally [146].

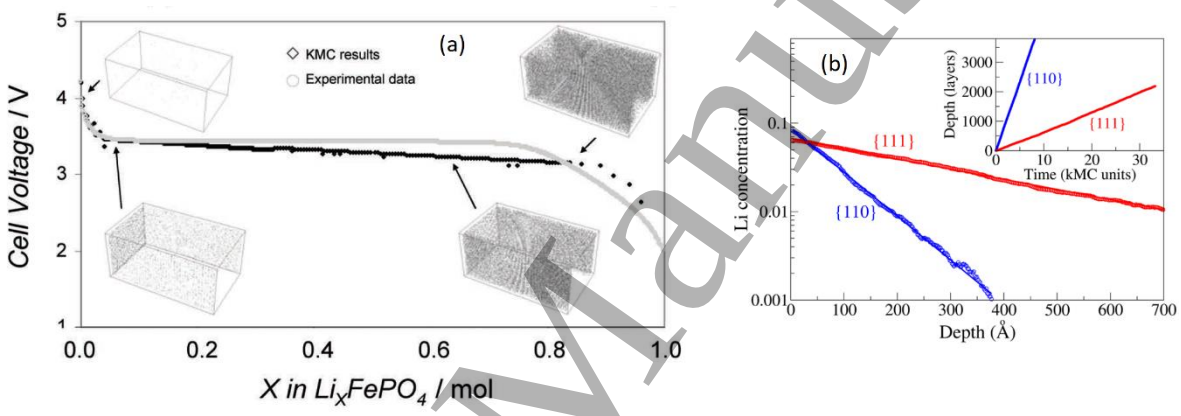

Figure 15: (a) Comparison between experimental galvanostatic curves for Li_xFePO_4 and kMC simulations. The current density was 0.5 A m^{-2}, under room temperature conditions. Grey points correspond to sites occupied by Li^+. Reproduced with permission from ref [141]. Copyright 2011 Wiley VCH. (b) Li concentration changes with depth for {110} and {111} surfaces of Silicon. The inset shows the time evolution of the depth reached by Li^+ for the two orientations. Reproduced with permission from ref [145]. Copyright 2013 American Chemical Society.

Based on *ab initio* and kMC simulations for the stage III-stage II transition, Krishnan et al. [147] highlighted the importance of kinetics and interactions for the intercalation of Li^+ in graphite, analysing the thermodynamics and kinetics of the staging phenomena leading to Daumas-Hérold structures. They used an energy barrier of 0.24 eV for hopping to second nearest-neighbour sites, based on the results of [64] and a pre-exponential factor taken from [120].

The subsequent work of Gavilán-Arriazu et al. [122] with kMC allowed to shed more light onto the origin of the Daumas-Hérold structures observed in graphite stages. In this work, energy barriers for charge transfer ($\Delta^0{}_{i/d} = 655$ meV) and diffusion ($\Delta^0{}_{diff} = 370$ meV) were obtained from the fitting of the experimental exchange current density [130] and diffusion coefficients [84], respectively. The pre-exponential factors were taken from reference [120]. The model, applied to a lattice-gas graphite slab of nanometric size, showed that DH structures are formed in a chronoamperometric kMC simulation. These structures are due to kinetic limitations arising from the slow rate of insertion/deletions of ions at the electrode/electrolyte interface as compared with diffusion. A scheme of this model is shown in Figure 16a. In the thermodynamic counterpart,

Rüddorf-Hoffman (RH) structures (where Li ions occupy each alternate graphite interlayer, leaving others nearly empty) were found with equilibrium MC simulations [37,48,82]. This shows that DH arrangements are metastable structures with higher energies than the perfectly ordered Stage II configurations obtained via equilibrium MC simulations.

The kinetic charge-transfer limitations become evident through the performance of simulations with an artificially reduced value of the charge transfer barrier, $\Delta^0{}_{i/d}$. Figure 16b shows the variation of the energy per Li^+ ion as a function of time, when $\Delta^0{}_{i/d} = 380$ meV (a value only 10 meV different from the diffusion barrier) A steep decrease of this energy can be observed at 40 ms (red dashed line) corresponding to the rearrangement of a DH structure to a RH one, closer to the thermodynamic equilibrium (a RH Stage II with some interlayer Li disorder). Thus, the enforced fast exchange rate of Li^+ at the interphase leads to the more stable RH structures.

Within the same model, Gavilán-Arriazu et al. [82] then extended the kinetic studies of LI^+ intercalation in graphite to analyse other techniques and properties. First, cyclic voltammetry kMC studies revealed that the hysteresis between the direct and inverse sweeps observed in experimental CV measurements, has an intrinsic kinetic origin (Figure 17a). The kinetic source of this hysteresis was then further understood with chronoamperometric simulations, as explained below

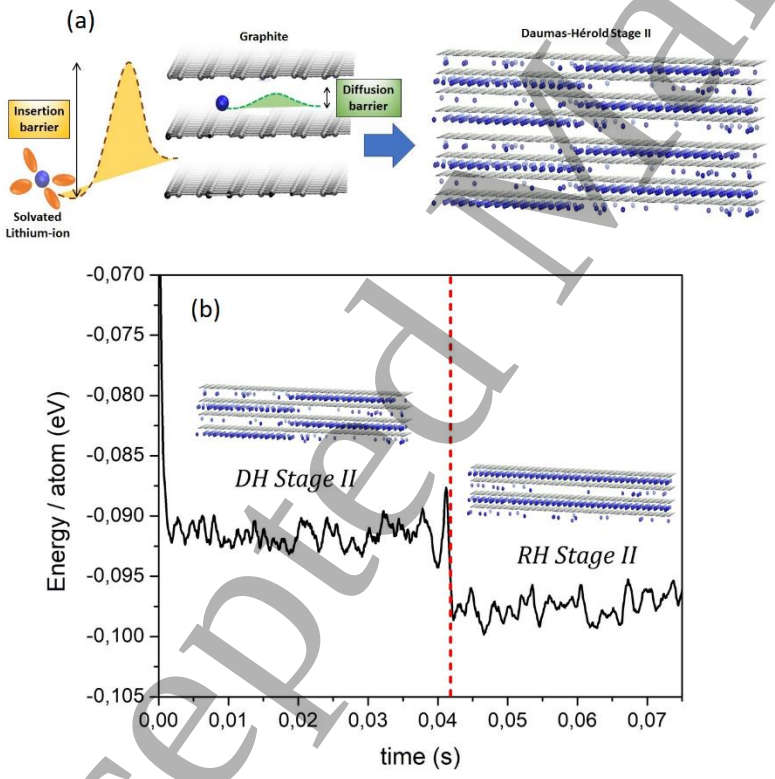

Figure 16: (a) Scheme of the model used by Gavilán-Arriazu et al. to explain the formation of DH domains in the case of Li^+ intercalation in graphite. Li^+ ions are represented with blue spheres, electrolyte with red balloons, and graphite is shown in grey. The energy barrier for particle exchange is shown in orange, the energy barrier for diffusion in green. The heights of the barriers are only illustrative, to show that the barrier for particle exchange is higher than that for diffusion transport. (b) Energy per Li^+ ion calculated with kMC simulations using a charge transfer barrier comparable to that of diffusion, to enforce equilibrium within simulation times. The dashed red line shows the time

at which a steep energy decrease reveals the transition from a DH structure to RH one. Reproduced with permission from ref [122]. Copyright 2018 Elsevier B.V.

Cyclic voltammograms (CVs) obtained with kMC show the impact of size on the overall processes observed in experimental CVs. The relationship, $\log(i_p) = a + b[\log(v)]$, defines the overall kinetic control of the process: $b = 1$ means pure charge transfer control, while $b = 0.5$ indicates a pure diffusional one. Intermediate values indicate mixed control. Experimentally, a change from a mixed control, at slow sweep rates, to diffusional control at higher sweep has been observed in thin graphite slabs [23] (Figure 17b). For thick graphite slabs, a pure diffusional control has been observed for all sweep rates [148]. The CVs simulated with kMC using nanosized slabs (ultra-thin slabs) found a mixed control for all sweep rates (Figure 17c). These results support experimental measurements: in nanosized systems, a concentration gradient cannot be formed, so pure diffusional control is not observed. As size increases, the system reaches conditions of finite diffusion, with kinetic control obtained at high sweep rates. Semi-infinite diffusion behavior is found for sufficiently thick electrodes.

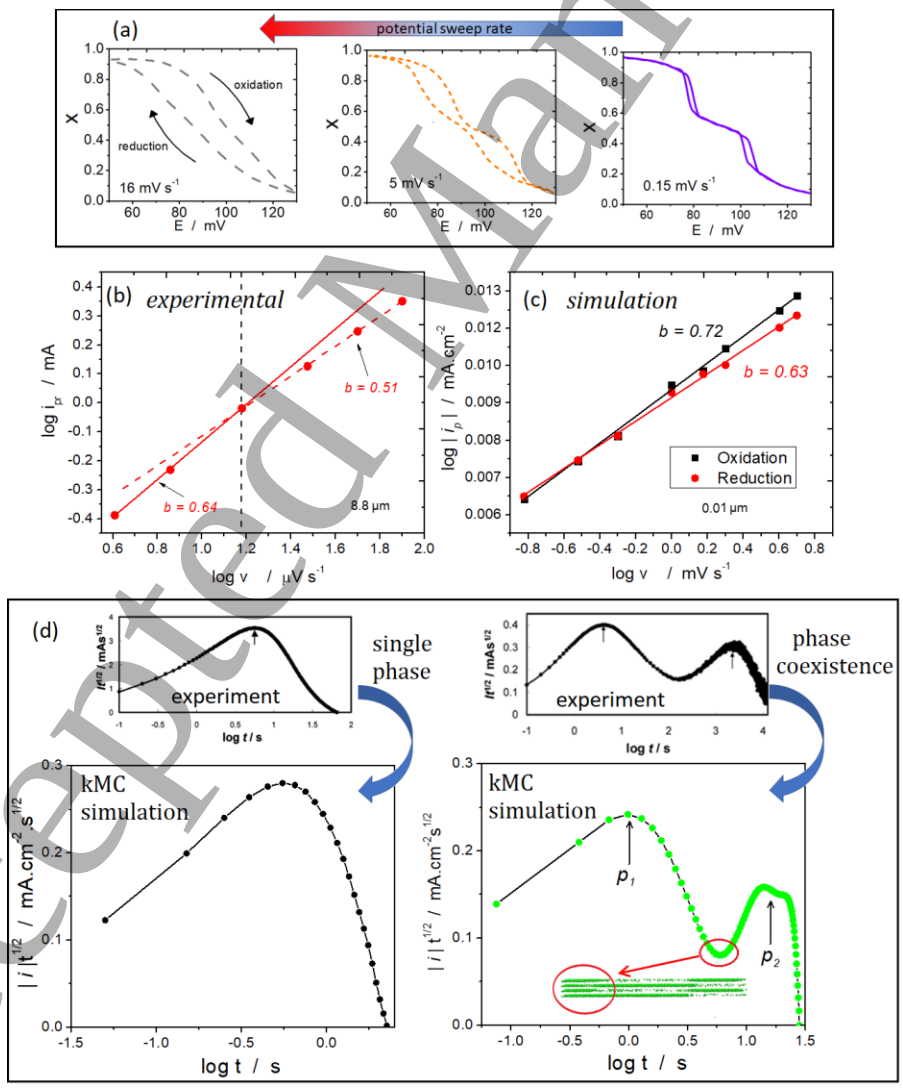

Figure 17: Results for Li^+ intercalation in graphite, except where otherwise indicated. (a) Isotherms obtained with kMC simulations of CVs for different sweep rates. A hysteresis loop is always present, becoming smaller at low sweep rates. Reproduced with permission from ref [123]. Copyright 2020 The Electrochemical Society. (b) experimental log-log plot for the reductive current peaks for the stage I-stage II transition vs the sweep rate, data extracted from [23]. The vertical dashed black line marks a change in slope. The red dashed line and the red solid line correspond to linear fits for high and low scan rates, respectively. (c) log-log plot for kMC simulated peak currents vs sweep rate for oxidation (black) and reduction (red). A coincidence is observed between simulated and experimental slopes at low sweep rates. (d) Current transients obtained with kMC for a potential step where a single phase is observed (left) and a potential step where phase coexistence occurs (right, green points). The experimental plots reproduced with permission from ref [133]. Copyright 2005 American Chemical Society. The simulation frame shows that the minimum between the two peaks (marked with a red circle) is due to the formation of a Li clog next to the interface (also marked with a red circle). In this inset, lithium ions are represented with green circles, and graphite substrate is omitted for easy viewing. Reproduced with permission from ref [82]. Copyright 2020 Elsevier Ltd.

The same work of Gavilán-Arriazu et al. simulated potential steps to get a deeper insight into the intercalation mechanism. Simulated current transients were compared with the experimental counterparts of reference [133]. The same trends were observed in experiments and simulations: on one hand, current transients present a single peak in the $|i|t^{1/2}$ vs $\log(t)$ representation (Figure 17d) when the initial and final potentials remain in the same lithiation stage. On the other hand, this representation of the current transient becomes divided into two peaks when the applied potential leads to a new lithiation stage. In this case, peaks p_1 and p_2, shown in the bottom right of Figure 17d, occur due to the coexistence of two phases (stages I and II) as the process evolves with time.

kMC simulations provide strong support to the experimental interpretations, yielding configurational information about the events taking place at different times of the potentiostatic transients. The snapshot of Figure 17d shows that the minimum between the pair of peaks in the $|i|t^{1/2}$ vs $\log(t)$ plot occurs when the new phase (stage I) is formed next to the interphase of the graphite slab, clogging the entry to the insertion of more Li^+ ions.

Moreover, the detailed atomistic information shows that the first peak, at shorter times, depends on charge transfer; while the second peak, at longer times, is under mixed control and is related to the growth of the new phase formed at the edge of the slab.

Another interesting result of these simulations is that deintercalation takes shorter times than intercalation, considering the same potential interval. This fact has also been observed experimentally [133,149]. The origin of this feature is again easy to unveil with kMC in the region of phase-coexistence: Figure 18a shows that when the potential step is in the direction of intercalation, it leads to the formation of a denser stage, which is initially formed next to the interface. On the contrary, for deintercalation potential steps, the stage formed next to the interface is less dense (Figure 18b). So, the denser stage formed during intercalation acts as a "clog" for Li^+ insertion, making particle insertion difficult. This is not the situation during deintercalation, because the less dense stage formed generates holes at the interface, which are rapidly filled by diffusing ions. This is one reason why hysteresis is always observed in CV experiments and simulations: the paths for Li^+ intercalation and deintercalation are different. These features were anticipated by Levi et al. [133,149]. However, simulations confirm their hypothesis, further providing atomistic information.

The cited works also shed light on changes of the exchange current density with Li^+ occupation observed in graphite, especially the maximum observed at the composition $x = 0.5$ (stage II) (Figure 18c). The predictions made using two Frumkin isotherms, one for stage II and another one for stage I, (dotted lines in Figure 18c), would lead to the conclusion that at $x = 0.5$ a minimum in j_0 should be observed. However, this is not the situation, neither for experiments nor for kMC simulations. The explanation was obtained from kMC runs initialized from a nearly perfect stage II configuration, which was obtained from equilibrium MC simulations (RH structure): a lower j_0 was obtained for a perfect RH structure, as compared with the defective DH structures. This result strongly suggests that the relatively high j_0 found at $x = 0.5$ is due to the formation of DH structures, in a scenario controlled by kinetics.

Gavillán-Arriazu et al. [123] investigated the effect of temperature on the kinetics of Li^+ intercalation in graphite via kMC. These simulations predicted the behavior of the chronoamperometric current transients for different input temperatures (Figure 19a). The configurations of the ions from the simulations were used to interpret the outstanding features occurring (events (i) to (v) in Figures 19b and c). j_o was calculated for different temperatures and lithium-ion concentrations (Figure 19d). Arrhenius plots of j_o were used to calculate the energy barriers for different stages (Table shown in Figure 19e), finding different energy barriers for the charge transfer at different stages, showing the impact of concentration and interactions on charge transfer kinetics.

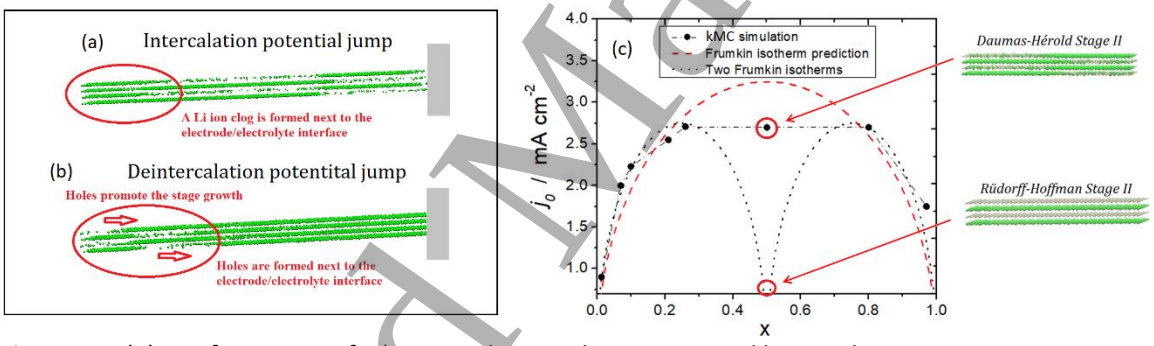

Figure 18: (a) Configuration of Li^+ inserted in graphite generated by a reductive potentiostatic jump. Green spheres are Li^+ ions; the graphite substrate was omitted. (b) Configuration of Li^+ ions in graphite obtained with an oxidative potentiostatic step. (c) exchange current densities obtained at different occupations at room temperature. kMC results are shown with full circles and dashed lines, a single-Frumkin isotherm prediction is shown in the red dashed line, and two-Frumkin isotherms are shown in a dotted line. The exchange current density values obtained from simulations for a DH type structure and RH arrangements at $x = 0.5$ are indicated with red circles. Reproduced with permission from ref [82]. Copyright 2020 Elsevier Ltd.

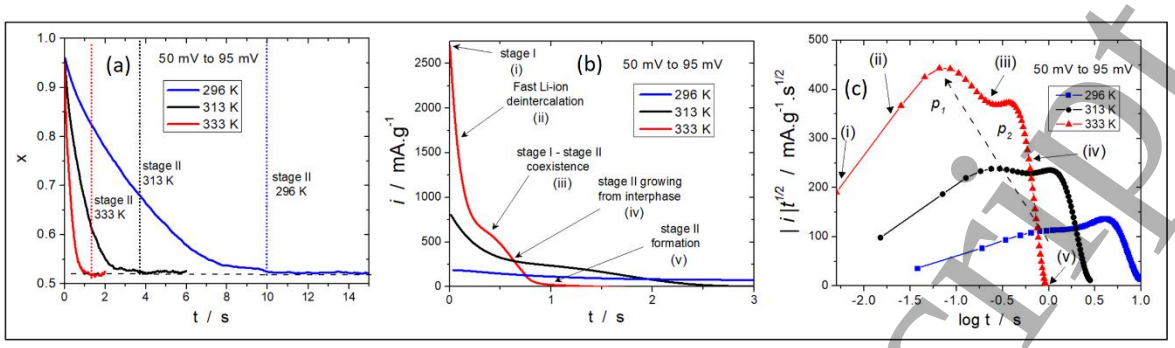

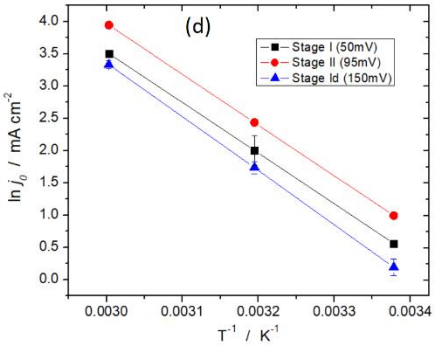

slope

(e)

Table III. Activation energy for charge transfer obtained from the Arrhenius plots of Figure 12 at different occupations conditions.

Stage	Electrode potential [mV]	Activation energy for charge transfer [eV]
Id	150	0.720 ± 0.003
II	95	0.679 ± 0.002
I	50	0.675 ± 0.001

Figure 19: (a) Li^+ occupation vs time, (b) current vs time and (c) $|i|t^{1/2} vs log t$ obtained with kMC simulations for the different temperatures indicated in the figures. The main features observed with the simulation frames are detailed in Figures (b) and (c). (d) Arrhenius plot for exchange current density at three different lithiation stages, leading to the calculation of activation barriers (shown in table (e)). Reproduced with permission from ref [123]. Copyright 2020 The Electrochemical Society.

5. Electrolyte: solid electrolyte interphase and Li^+ transport

Besides ion transfer at the electrode/solution interface and ion transport within the electrodes, other phenomena occurring in the electrolyte and at the electrolyte/electrode interface are further sources of rate limitation in the operation of LIBs. These have to do with the formation and growth of the so-called *solid electrolyte interphase* (SEI) on anodes and with Li^+ transport between the electrodes.

5.1. The Solid electrolyte interphase (SEI):

The SEI forms when the potential applied to the electrode exceeds the limits at which the electrolyte is stable. So, the electrolyte starts to degrade via a reduction reaction on the anode surface. The SEI is mainly formed at the first charging cycle and then acts as a barrier to prevent further electrolyte reaction in successive cycles, allowing Li^+ transport. The properties of the SEI (composition, thickness, morphology, etc.) depend on the operating conditions, and its generation is often accompanied by the formation of byproducts, capacity fade, and higher charge transfer resistances. These changes impact charge transfer and so the performance of LIBs. Thus, identification of these alterations and analysis of optimal conditions for its generation is crucial to optimize battery operation [2,150,151].

Methekar et al. [152] have simulated SEI formation and growth along charging cycles at constant potential (100 cycles) with kMC. This model simulated passive SEI layer formation, reduction, and growth, including in the perpendicular direction of lithium-ion intercalation. For such a model the

authors considered the formation of undesirable products (P) at the anode surface (S), according to Equation (40):

$$S + 2e^- + 2Li^+ \rightarrow P \quad (40)$$

These products promote an increasing layer thickness and blocking of the pores, so leading to an increasing charge transfer resistance. The events considered at the electrode/electrolyte interface within this model are: adsorption, desorption, surface diffusion, and formation of product P. The simulation parameters were obtained from continuum models and experiments. The side reaction for SEI formation and growth is described with a Butler-Volmer equation. Figure 20a shows the active surface coverage corresponding to the last configuration of a cycle vs the number of cycles. It is observed that the active surface coverage begins to decrease after cycle n° 10, as observed experimentally [153]. Figures 20b and c show configurations for the first and last cycles, respectively, where it can be observed that the number of passive sites (red squares) increases with the number of cycles. This work also discussed the impact of temperature and exchange current density on the charging cycles, showing that higher temperatures (20 degrees above room temperature) and low exchange current densities improve the performance of the overall process.

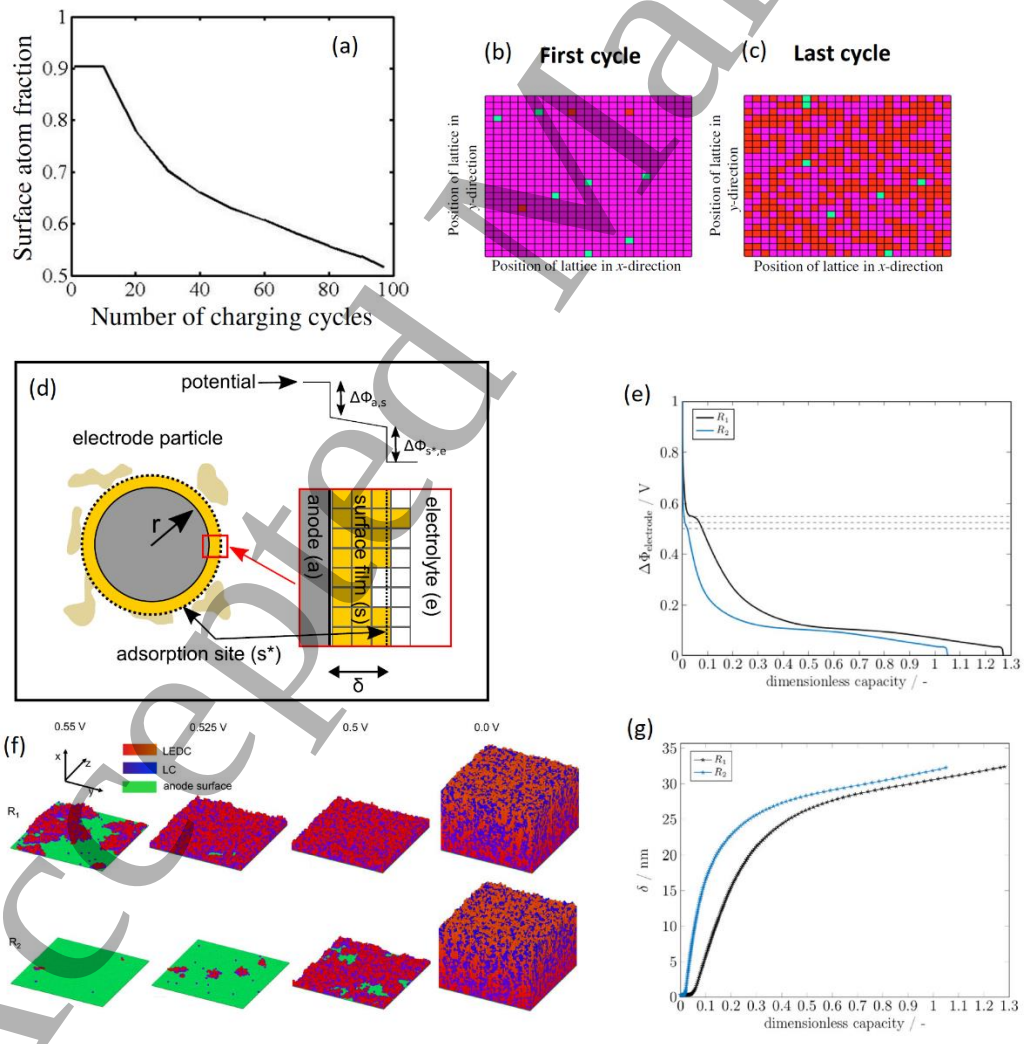

Figure 20: (a) Coverage of active SEI sites, considering the last coverage for each cycle, vs the number of charging cycles, at room temperature (298 K) and j_0= 1.5x10^{-10} A/m^2. (b) first cycle and (c) last charging cycle configurations. Magenta squares are virgin sites, while red squares are passive sites. Green squares are adsorbed Li^+ ions. Reproduced with permission from ref [152]. Copyright 2011 The Electrochemical Society. (d) Scheme of the multi-scale coupling between the continuum scale and the single-particle events of kMC. The anode/surface film ($\Delta\Phi_{a,s}$) and adsorption site/electrolyte ($\Delta\Phi_{s*,e}$) potential drops are also shown (e) electrode potential vs dimensionless capacity for a charging rate of 0.1 C and two-particle radii, $R_1 = 3$ μm and $R_2 = 10$ μm. (f) kMC configurations for SEI growth on the particles observed at different potentials, the LEDC, LC, and anode surface colors are indicated in the Figure. (g) Average SEI thickness is reported for the same conditions as Figure (b). Reproduced with permission from ref [154]. Copyright 2017 The Electrochemical Society.

Röder et al. [154,155] implemented a multi-scale model to simulate SEI formation and growth. They used a continuum model coupled with a kMC scheme, which considered the rates for surface diffusion, adsorption on top of surface sites, desorption, and side reactions for SEI growth. The model is shown in Figure 20d. Macroscopic calculations are made at the single-particle level, where the particle is surrounded by a dense inner film (orange) and byproducts that reduce porosity (light brown clouds). The microscopic zoom view inside the red square corresponds to the kMC simulation level. Potential drops are shown at the anode/surface film interface ($\Delta\Phi_{a,s}$) and at the film/electrolyte interface ($\Delta\Phi_{s*,e}$). The activation energies for diffusion and desorption were a function of the interactions at the local environment, while adsorption rates depended on the electrolyte species activities. The kMC equations for electrochemical reactions also considered the modification of the activation energy with the microscopic distance between the surface site of the film and the anode surface. Pre-exponential factors for diffusion were calculated from the surface diffusion coefficient. After a time interval, continuum and kMC models exchange information: microscopic configurations are updated with continuum data, while kMC outputs are introduced as inputs in the continuum model to set parameters. The authors used ethylene carbonate (EC) with $LiPF_6$ salt as the electrolyte, graphite as the anode, and assumed solid lithium carbonate (LC) and lithium ethylene dicarbonate (LEDC) as reaction products. Figure 20e shows the results for the electrode potential ($\Delta\Phi_{electrode}$) vs dimensionless capacity for a charge rate of 0.1 C and two-particle radii, $R_1 = 3$ μm and $R_2 = 10$ μm. The corresponding microscopic kMC configurations for the SEI growth at different potentials, for both radii, are shown in Figure 20f. The grey dashed lines in Figure 20e correspond to 0.55 V, 0.525 V, and 0.5 V, whose configurations are shown in Figure 20f. Finally, the average layer thickness is plotted vs the capacity in Figure 20g, illustrating the evolution of the SEI. These results show that particle size has more impact on SEI growth rate than on the final average film thickness and that the model provides a suitable tool for future theoretical works.

Another multi-scale approximation to simulate the SEI growth is the model of Shinagawa et al. [156]. This approach was similar to the previous multi-scale model, consisting of a single particle continuum model coupled with kMC simulations for SEI growth. The results presented included the capacity fade and SEI growth for hundreds of charging cycles, demonstrating the long times that this approach can simulate (Figure 21a).

A different approach for SEI growth was that developed by Hao et al. [78], including the three steps introduced above. The calculation of the kMC rates were those of mesoscale, given by Equation (16)

for Li-ion intercalation. The reaction of Li-ions with the solvent was treated in a way analogous to that of intercalation. The overpotential for both rate calculations, Li-ion intercalation, and side reactions, considered the electrolyte potential and the SEI ohmic drop as follows:

$$\eta = E - E_{electrolyte} - E^0 - i_t R_{SEI} \quad (41)$$

where $E_{electrolyte}$ is the potential in the electrolyte, R_{SEI} is the SEI resistance and i_t is the total current for intercalation (i_{Li^+}) and solvent reaction (i_{SEI}):

$$i_t = i_{Li^+} + i_{SEI} \quad (42)$$

Each current was calculated with BV expression, Equation (9). The activation energies for Li^+ diffusion in SEI, 38.4-76.8 KJ.mol^{-1}, were taken from the theoretical-experimental work in references [157,158], the pre-exponential factor was in the range $10^{12} \sim 10^{13}$ s^{-1}. Exchange current densities of 1 mA.cm^{-2} and 0.1 mA.cm^{-2} were used to calculate the rate constants for Li^+ reduction and SEI growth, respectively.

This model showed how activation energies for Li^+ diffusion affect charging times. Higher activation energies decrease Li^+ content at the electrode surface (Figure 21b), increasing the mass transfer dependence of the overall process. It was also shown how the solvent activation energy for diffusion affects SEI growth (Figure 21c).

Future modelling approaches should take into account that SEI growth continues even at open-circuit conditions ($i_t = 0$). Loss of Li into ongoing SEI growth during 'calendar ageing' is governed by the anode potential and its interplay with shuttle-type side reactions [159] that have their counterparts at the cathode.

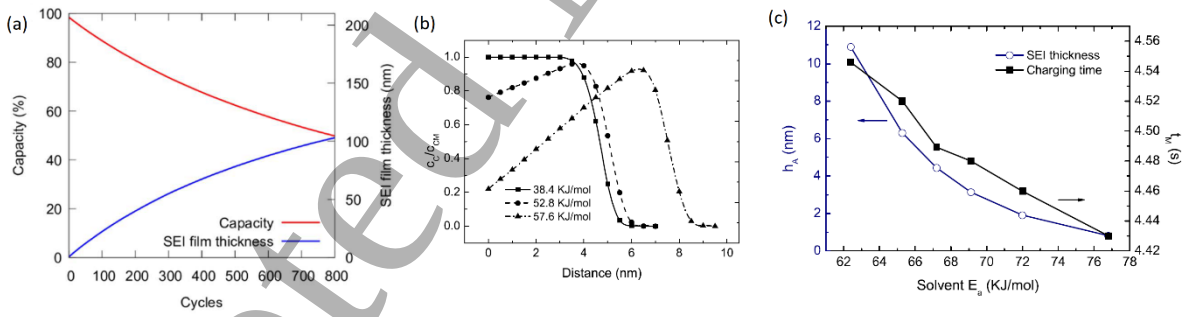

Figure 21: (a) Capacity and SEI thickness as a function of charging cycles. Reproduced with permission from ref [156]. Copyright 2017 The Electrochemical Society. (b) Concentration profiles for different activation energies for Li^+ diffusion. (c) SEI thickness and charging time for different activation energies for solvent diffusion. Reproduced with permission from ref [78]. Copyright 2017 American Chemical Society.

5.2. Li^+ transport in electrolyte:

Regarding Li^+ transport in a solid electrolyte, kMC models consider Li^+ hopping in a lattice of fixed geometry. An optimum electrolyte consists of a material with high ionic conductivity. The latter depends on the geometry of the hopping sites, the chemical composition, and the concentration of

ions [160]. So, understanding these factors is crucial to design better electrolyte materials. Conductivity is related to the diffusion coefficient according to:

$$\sigma = \frac{Cq^2}{k_B T} D^* \quad (43)$$

where C is the concentration, q the charge of the ion and D^* is the tracer diffusion coefficient defined in Equation (30)

The work of Scarle et al. [161] designed a kMC model to study Li^+ motion in polyethylene (PE). The energy was calculated within a self-consistent polarization field method (SCPF). It consists of the calculation of the polarization energy in a spherical region centered on a Li^+ ion interacting with the induced surrounding dipoles in the electrolyte, ignoring Li^+ polarization. A complete description of the method is detailed in reference [161]. The rate of Li^+ mobility was calculated with the typical kMC equation for activated processes, Equation (5), obtaining the activation energy for the hopping jump from a site *i* to a site *j* , Δ_{ij}, from:

$$\Delta_{ij} = U_{SCPF,j} - U_{SCPF,i} \quad (44)$$

where $U_{SCPF,j}$ and $U_{SCPF,i}$ are the SCPF energies for the sites *i* and *j*, respectively. The polymer structures consisting of 200 methylene groups were constructed using a polymer builder and an energy minimizer, and the polarization energies for a Li^+ were calculated. The results showed deviations of the Li^+ ion mean-square displacement (MSD) from the random walk behavior as a consequence of the environment. Unfortunately, no comparison with experimental cases was made, but this work set a precedent for future work.

First-principles studies of solid inorganic electrolytes with $(Al_xMg_{1-2x}Li_x)Al_2O_4$ spinel structure with different stoichiometry were carried by Mees et al. [162]. In this work, the diffusion of a Li^- vacancy, introduced in the $(Al_xMg_{1-2x}Li_x)Al_2O_4$ structure for a given x, was simulated with kMC. After a Li^- vacancy was introduced, the diffusion paths for Li^- exchange with successive adjacent cations were evaluated with the NEB algorithm. One of these paths was chosen statistically within the kMC algorithm, to exchange occupations with one of the nearest neighbors. The diffusion coefficient D was then obtained with the classical relationships shown above in Section 3 for a single vacancy. An Arrhenius plot with the diffusion coefficients at different temperatures (Figure 22a) allowed the calculation of the activation energies for different x (Figure 22b). A decrease of the activation energy was found for increasing Li^+ fraction in the electrolyte structure; indicating a better conductivity.

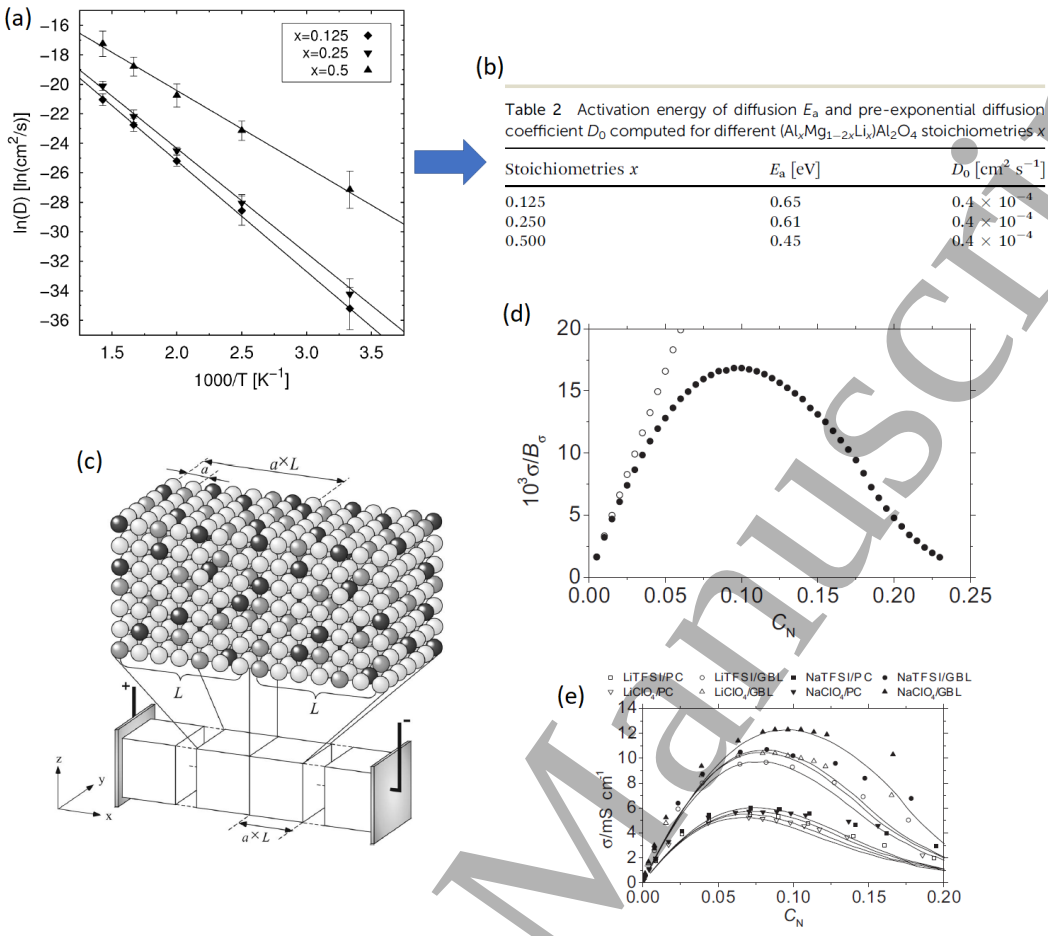

Figure 22: (a) Arrhenius plot for the diffusion of a single vacancy in $(Al_xMg_{1-2x}Li_x)Al_2O_4$ at different *x*, obtained from kMC simulations. (b) Activation energies obtained from Arrhenius the plots of Figure (a). Reproduced with permission from ref [162]. Copyright 2014 the Owner Societies. (c) Scheme of a liquid electrolyte model within an electrochemical cell, considering three moving species: anions, cations, and solvent. The size of the simulation box is *L* and *a* is the unit cell parameter. (d) kMC results for the ionic conductivity (σ) vs the concentration number (C_N) for the model shown in Figure (c), considering interacting (full circles) and non-interacting particles (empty circles). (e) Experimental σ vs C_N. Reproduced with permission from ref [163]. Copyright 2016 The Electrochemical Society.

Later on, Ozaki et al. [163] developed a kMC approach to study Li^+ self-diffusion and ionic conduction in electrolyte solutions at high concentrations. The model consisted of a "pseudo"-lattice, with a single lattice constant, where ions and solvent may move (Figure 22c). Each of the sites was considered to be occupied by one of the species: anions (charge -1), cations (charge +1), or solvent molecules (neutral). Interactions among the different species were considered and exchange or "swap" of species placed in nearest neighbor sites was evaluated. The authors also considered the role of the heat of dissolution of the crystal in the solvent, to calculate the energetics of the system. The ionic conductivity was calculated from:

$$\sigma = \frac{j}{\vec{E}} \qquad (45)$$

where j is the current density calculated from the flux of anions and cations through a unit area and $\vec{E}$ is the electric field. The results showed that repulsion between ions with the same charge determines the bell-shaped form of the conductivity as a function of the concentration number C_N (Figure 22d), as observed in the experiment (Figure 22e).

Geometry effects on Li^+ transport in "lithium-garnet" electrolytes [164] explored by Morgan [160]. Garnet electrolytes are solid materials with the formula $Li_xM_3M'_2O_{12}$, M and M' being two different metals. The geometry of the lattice is considered as "unusual" (Figure 23a) and in this work, it was used to define a lattice gas. In the stoichiometry of the material, $x_{Li} = 9$ corresponds to the fully occupied lithium-site lattice. Morgan used $v^0 = 1\text{x}10^{13}\ s^{-1}$ and a Metropolis algorithm [51] to calculate the hopping probabilities.

The cases of non-interacting particles and nearest-neighbor interactions were considered. Correlation factors were defined to account for deviations of some parameters from the random walk behavior: a factor f for D^* and f_I for σ. Different correlation factors for D^* and σ mean that correlations effects modify the relationship given Equation (43). The reduced conductivity shows the effect of the concentration on conductivity and is expressed as

$$\sigma' = xD_j \tag{46}$$

where x is the occupation degree of the lattice, $x = 1$ is equivalent to $x_{Li} = 9$, and D_j is the jump-diffusion coefficient.

The kMC results showed that this kind of solid present deviations of the tracer diffusion coefficient from the random walk behavior, for the non-interacting case, when Li^+ content is high (Figure 23b). Predictions were also made considering the repulsive energy between first neighbors (Figure 23c, d and e). These predictions may be useful for designing Garnet electrolytes with optimal conductivity properties.

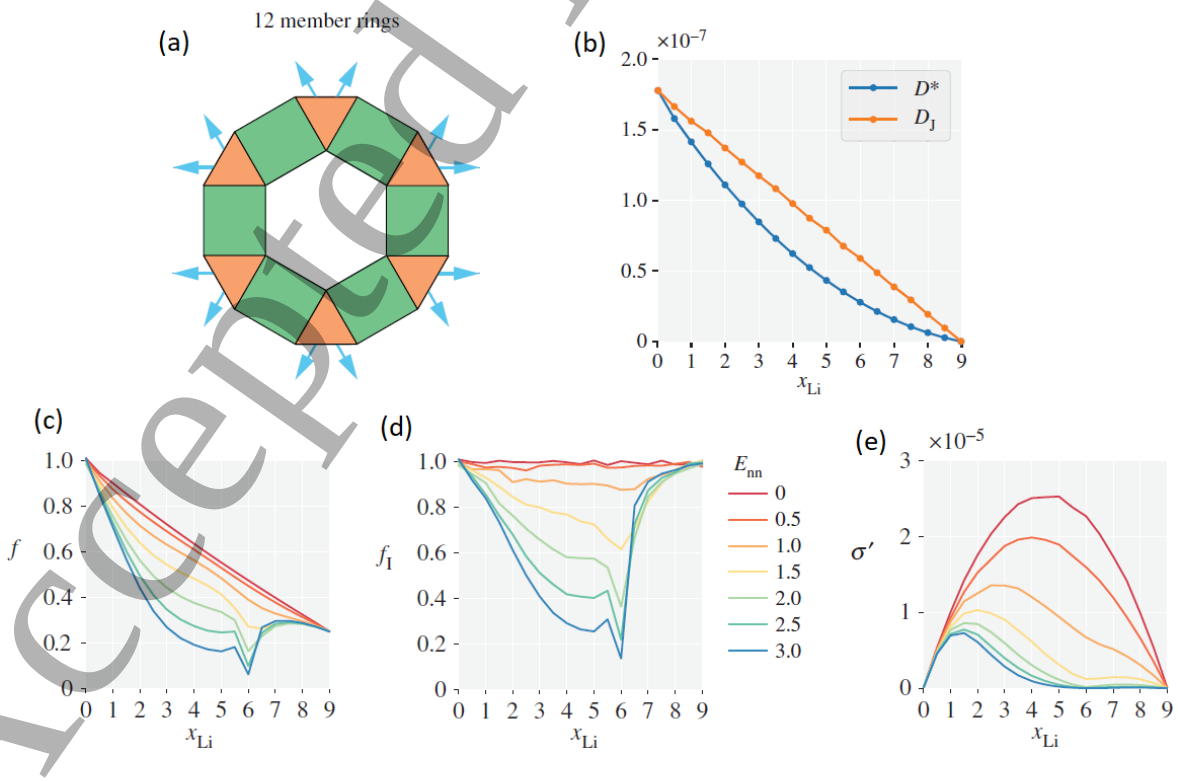

Figure 23: (a) Ring structure of a diffusion network in a garnet electrolyte. Alternating octahedral (orange) and tetrahedral (green) sites. The arrows show links with other rings. (b) Tracer and jump-diffusion coefficient for non-interacting particles. (c) correlation factor f (d) correlation factor f_I and (e) reduced conductivity σ' vs lithium content x_{Li} for different repulsive energies between first neighbors E_{nn}. Reproduced with permission from ref [160]. Copyright 2017 The Royal Society.

Regarding Li_3PO_4 electrolyte, Li et al. [165], have studied Li^+ diffusion using kMC and a machine-learning-based interatomic potential called a neuronal network (NN) potential to study Li^+ diffusion. The attractiveness of Machine-learning to study diffusion in amorphous materials is due to the fact that, compared with DFT, it has a much lower computational cost. One of the reasons is that the characterization of diffusion pathway in these types of material is complicated. The basic idea is that a NN potential "learns" from DFT calculations and then can predict structural energies that were not contained in the training set. Li et al. calculated with DFT the energies of 38592 structures. From these, 30874 were used for a training set, while the remaining were used as independent testing data. The diffusion coefficients obtained with the NN potential at different temperatures, calculated with kMC and MD, were found in agreement with those obtained with DFT-kMC and ab-initio MD, with DFT-kMC demanding a smaller computational effort. Li et al. used a $v^0 = 1\text{x}10^{13}\ \text{s}^{-1}$ and energy barriers calculated with NEB method.

6. Post-Li-ion cells

In the quest for storage systems with higher energy density, new systems are being designed that involve metallic lithium as an anode. Two attractive cells that present outstanding theoretical characteristics are Lithium-air (Li-O_2) with a gravimetric energy density of 11680 Wh.kg^{-1} [19] and Lithium-Sulfur (Li-S) with a gravimetric energy density of 600 Wh.kg^{-1} [16–18,166].

The most common Li-O_2 battery is that with non-aqueous electrolytes, although configurations with aqueous and hybrid aqueous electrolytes have been proposed. The cell consists of a non-aqueous Li metal anode and an air cathode made of an active surface (typically carbon) where oxygen is reduced in the first step to superoxide, which further reacts yielding finally Li_2O_2 (Figure 24). The reactions involved in the cell during a discharge cycle are the following:

Anode:

1) $Li \rightarrow Li^+ + e^-$ (47)

Cathode:

1) $O_2 + e^- \rightarrow O_2^-$ (48)

2a) $LiO_2 \rightarrow Li_2O_2 + O_2$ (49)

2b) $LiO_2 + 2Li^+ + 2e^- \rightarrow Li_2O_2$ (50)

The overall reaction results in:

$O_2 + 2Li^+ + 2e^- \rightarrow Li_2O_2 \qquad E^0 = 2.96\ V\ vs\ Li\ /\ Li^+$ (51)

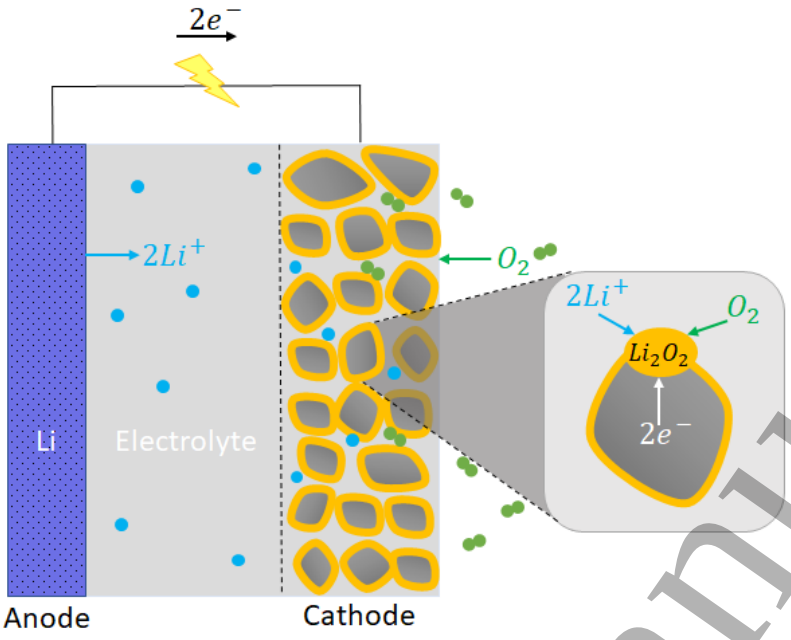

Figure 24: Schematic representation of Li-O_2 cell.

Turning to consider another post-lithium system, a Li-S electrochemical cell consists of a Li anode, a sulfur/carbon+binder cathode, an aqueous organic electrolyte, and a separator [167]. The anode reaction during discharge is the same as in Equation (47). The overall reaction of the cell for the discharge reaction is:

$$S_8 + 16Li \rightarrow 8Li_2S \quad (52)$$

This reaction occurs in two steps, as discussed in reference [167], where several reactions occur. The cell reactions and sulfur compounds arising at different stages are shown in Figure 25.

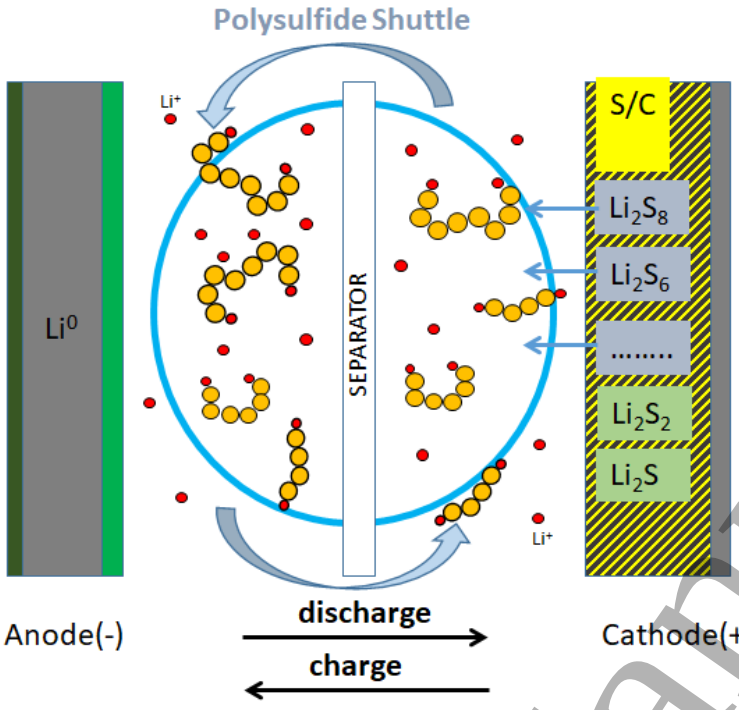

Figure 25: Schematic representation of a Li-S electrochemical cell and the different polysulfide species arising during the discharge reaction. The shuttle effect produced by polysulfides is illustrated schematically.

Despite their promising theoretical capacities, both kinds of post-lithium cells present different handicaps. In addition to the problems discussed in the introduction for metallic Li anodes, like dendrite formation and drastic volume changes, it turns out that Li_2S and Li_2S_2 present low conductivities, and that a phenomenon denominated the "shuttle effect" arises. The latter is caused by the migration of polysulfides from the cathode to the anode, where they are reduced. The problems with the lithium-air battery concern its unsatisfactory discharge capacity, its high overpotential, and severe parasitic reactions. Many of these deficiencies are due to the high reactivity of peroxidic species and to the insoluble and insulating nature of Li_2O_2 that forms during discharge. Thus, it is crucial the development of adequate theoretical models to bring answers to these critical issues [16,166–168].
In the following sections, kMC studies applied to metallic Li anodes (6.1), Li-air battery cathodes (6.2) and Li-S battery cathodes (6.3) will be presented.

6.1. Electrodeposition and growth on a metallic Li anode:
Most cell prototypes for Li-S and Li-air use Li-metal as the anode, and dendrite growth is one of the main failure mechanisms of LiBs. So, understanding dendrite formation and growth in metallic Li anodes is a key element to the development and understanding of these three types of cell, as described in detail below.
Dendrite growth and metal deposition on a metallic Li anode were analyzed by Aryanfar et al. [169], with coarse-grained kMC and experiments. They considered random diffusion and electromigration of Li^+ in an electrolyte formed by 1 M LiClO4 dissolved in propylene carbonate. The electric field was position- and time-dependent. The authors applied to the experimental working electrode current

pulses (-2 mA.cm^{-2}) of variable duration (t_{ON}), from 1 ms to 20 ms with ratios of $\gamma = t_{OFF}/t_{ON} = 0, 1, 2, 3$, where t_{OFF} represents a time during which galvanostatic control was lifted. These pulses were applied to deposit variable amounts of lithium. Since the galvanostatic experiment showed a stable voltage regime, the kMC simulations assumed an equivalent potentiostatic condition. Figure 26a shows the experimental and simulation results. The average dendrite length varies depending on the frequencies of the charging pulses. Short pulse durations $t_{ON} = 1$ ms with longer t_{ON} ($\gamma = 3$) reduces dendrite length, as compared with long pulse durations (20 ms), which do not show a change in dendrite length when increasing t_{OFF}. kMC simulation details, in Figure 26b, show the impact of the electric field on deposition growth (blue vectors), comparing $t_{ON} = 1$ ms with $t_{ON} = 20$ ms for $\gamma = 3$. The same model was then used to generate surface morphologies and perform MD simulations with a reactive potential (ReaxFF) [170]. This work highlighted the importance of Li self-diffusion for thermal relaxation of Li anodes.

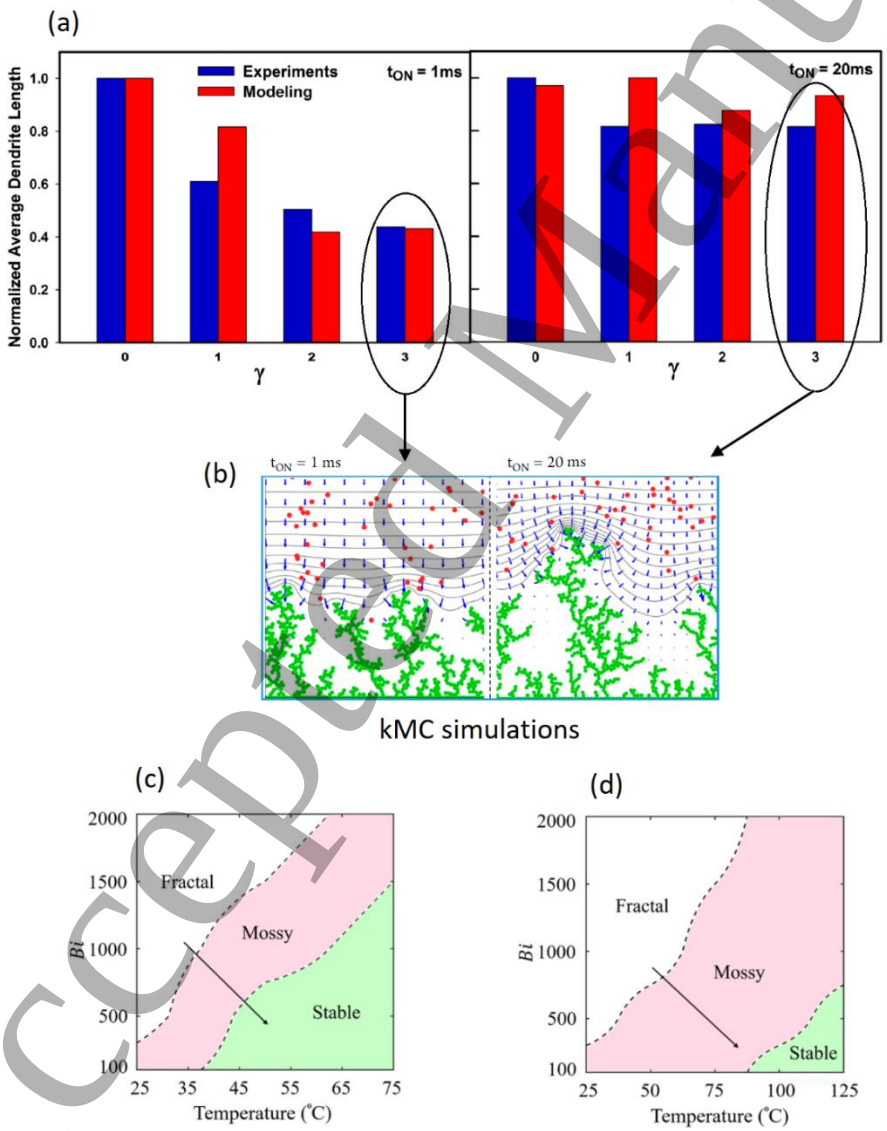

Figure 26: (a) Normalized average dendrite length for different $\gamma = t_{OFF}/t_{ON}$ ratios, as defined in the text. Two t_{ON} were considered. The results shown are from both experiments (blue bars) and modeling (red bars). (b) Representation of two configurations at different t_{ON}, for $\gamma = 3$, obtained with kMC simulations. Reproduced with permission from ref [169]. Copyright 2014 American Chemical Society. (c) Phase map of different morphologies obtained with kMC simulations, assuming a uniform thermal field. The diagram is constructed in the *Bi*-parameter (see text)/temperature plane. (d) Phase map of different morphologies obtained with kMC simulations and a non-uniform thermal field. Reproduced with permission from ref [171]. Copyright 2020 American Chemical Society.

Mesoscale kMC modeling has been developed by Vishnugopi et al. [171], to study electrodeposition on a metallic Li anode. Reaction at the metal/electrolyte interface, surface diffusion of Li atoms, and diffusion of Li^+ in the electrolyte were considered. The rate constant for the reaction at the electrode surface (Γ_{ch}) was calculated according to Equation (16). The diffusion rates of the atoms deposited on the surface of the electrode were calculated assuming $v^0 = 10^{12} - 10^{13}\ s^{-1}$ and two activation barriers, depending on the type of surface diffusion. These were terrace diffusion ($\Delta = 0.14$ eV) and interlayer diffusion ($\Delta = 0.4$ eV) [172].The diffusion rate constant in the electrolyte was calculated as $\Gamma_{elec} = D/(2a)^2$.

A dimensionless quantity denominated Biot number, Bi, was defined as:

$$Bi = \frac{h}{a\delta}\frac{\Gamma_{ch}}{\Gamma_{ele}} \quad (53)$$

where h is the height of the system and δ is the occupation ratio of cation sites available in the electrolyte domain. Simulations were performed for different Bi and temperatures, and the structures of the deposit morphologies were classified into fractal, mossy and stable, depending on the degree of porosity, formation of rounded tips, and dendrite height. Phase diagrams were constructed in the $Bi - T$ plane Figure 26c and Figure 26d for uniform and non-uniform thermal fields. The latter denomination indicates that the thermal field was only applied to the surface of the electrode, in contrast with the uniform one, where the thermal field was uniform throughout the cell. From fractal to stable phases, the porosity is reduced, the tips are more rounded and the dendrite height is lowered. The phase maps show that, in the case of the non-uniform thermal field, the morphology changes occur over a wider temperature range than with a uniform thermal field.

Later on, Ghalami Choobar et al. [173] studied the electrodeposition of Li onto metallic Li with a kMC-embedded atom method, considering (100), (110), and (111) single crystal faces. The reaction influenced by the electrochemical double layer was described using the Frumkin-Butler-Volmer equation [174]. Four types of mechanism were allowed for adatom diffusion, each of them with a different activation energy and pre-exponential factor, obtained from references [175–179]. These results showed the morphology evolution with time and considered how to reduce dendrite growth in terms of the LIB operating conditions and modification of its anode surface chemistry.

An aspect not considered in the previous works is the passivation layer formed on the Li metal surface. This topic was treated by Sitapure et al. [180] with kMC and MD simulations, considering the impact of the SEI on dendrite growth. MD was used to simulate SEI formation in different electrolytes: $LiPF_6$ + Dioxolane (DOL) + Fluoroethylene carbonate (FEC), and $LiPF_6$ + Ethylene

carbonate (EC). For this purpose, a reactive force field (ReaxFF) was implemented. kMC was employed to simulate the following events in the system: Li^+ incorporation into the SEI, Li^+ diffusion through the SEI, and Li^+ reduction on the anode surface. The pre-exponential factor was 2×10^{12} s^{-1}. The activation energy for desolvation was 0.43 eV [181].The activation energies for diffusion in the SEI depended on the type of electrolyte considered, and were taken from [182,183]. The rate for the reaction on the surface was calculated from the Faradaic current, following Equation (16). It was found that lower diffusion energy barriers in the SEI enhance dendrite formation.

6.2. Li-air battery cathode

A mesoscale model was developed by Blanquer et al. [184] to study O_2 and Li^+ transport, and reaction in a 3D cathode pore. The model considered a single pore with spherical geometry of different sizes and conducting cylindrical channels for Li^+ and O_2 transport with different radii and lengths. The model assumed that when Li^+ and O_2 react inside the pore, they form LiO_2 pairs in the first reaction step. These species can either move to the electrolyte and form Li_2O_2 and O_2 or can remain inside the pore and react on the surface to form a passivation layer. Simulations showed that the reaction to form LiO_2 mainly occurs next to the oxygen input channel, and depends on the size of the system, as shown in the snapshots on the right-hand side of Figure 27a. Changes in diffusion coefficients in the simulations lead to an increase of reaction rate and cell capacity. These conclusions are in agreement with previous experimental results [185].

Li_2O_2 thin film formation on a carbon nanofiber in contact with an electrolyte (dimethyl sulfoxide with 1 M Li^+) was modelled with mesoscale kMC by Yin et al. [186]. The model also considered catalyst nanoparticles randomly distributed on the surface of the nanofiber. Five different species and two-step mechanisms for Li_2O_2 formation were considered, as illustrated in Figure 27b. All species were allowed to translate or rotate on the surface, except Li_2O_2, which was assumed to form a film. Rate constants for reactions were calculated with a Butler-Volmer approach, considering on the surface slower kinetics due to passivation when the Li_2O_2 film is formed. A pre-exponential factor of $1x10^{10}$ s^{-1} was considered for the reaction on the carbon surface, while it was assumed to be two orders of magnitude higher for the catalysed reaction. Figure 27c shows Li_2O_2 film growth in the absence and presence of the catalyst. The colours of the species are the same as those shown in Figure 27b. In the case of the catalyst-loaded system (right of Figure 27c), Li_2O_2 growth on the catalyst species forms a thick film (depicted in green) on top of a thin film (depicted in orange), the thin film being in direct contact with carbon.

Due to the poor electron conductivity of Li_2O_2, Li-O_2 cells achieve higher discharge capacities when the Li_2O_2 deposit grows in a 3D mode rather than forming homogeneous films. Whilst this behaviour has been modelled on mean-field level [187], kMC simulations would be ideal to quantitatively explore the underlying EC-mechanism and its response to changes of electrolyte and electrode materials.

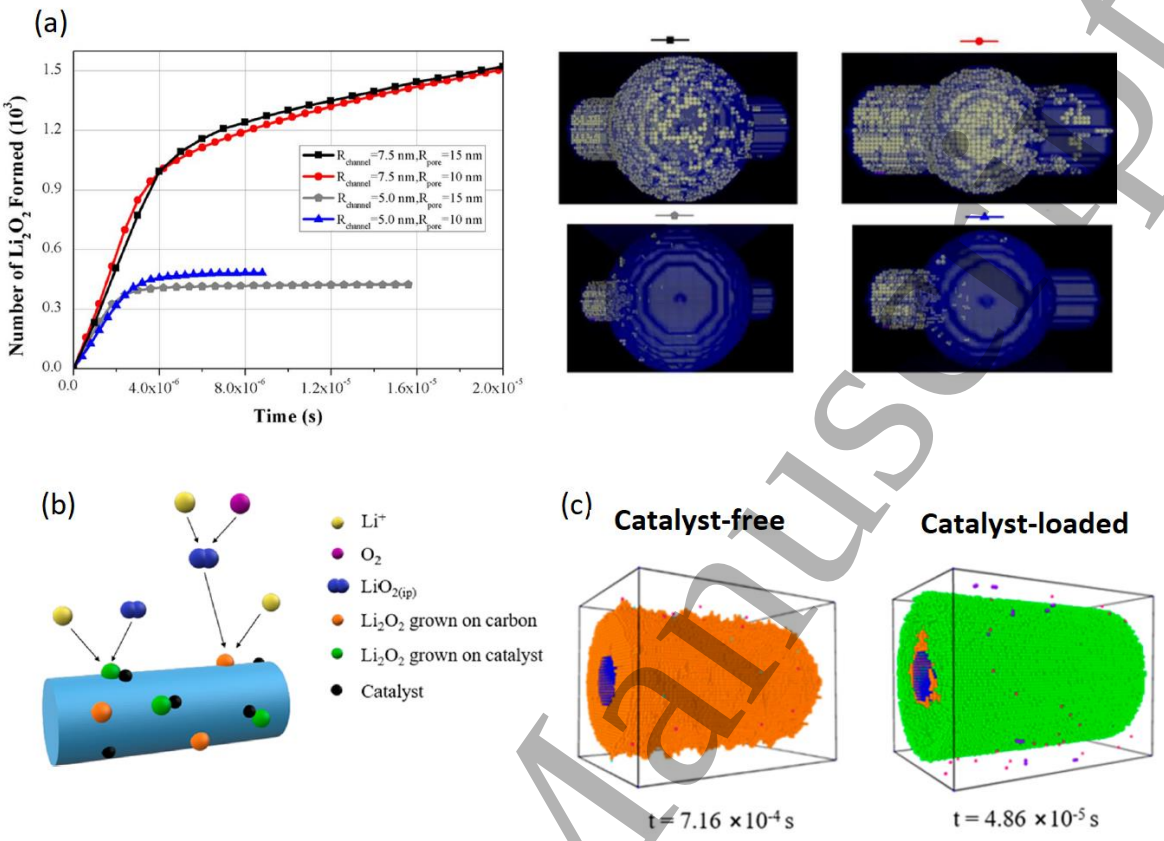

Figure 27: (a) Evolution of the number of Li_2O_2 species in pores and channels of different sizes. Simulation snapshots are also shown on the right Reproduced with permission from ref [184]. Copyright 2016 The Electrochemical Society. (b) Events allowed for Li_2O_2 electrodeposition on a carbon nanofiber, the color that represents each species is indicated in the Figure. (c) Final configurations for discharge process on a catalyst-free surface (left) and catalyst-loaded surface (right). The colors are the same as in Figure (b). Reproduced with permission from ref [186]. Copyright 2017 American Chemical Society.

6.3. Li-S battery cathode

A mesoscale kMC model to simulate LiS_2 film growth on a carbon surface was developed by Liu et al. [188]. Li_2S adsorption, desorption, and diffusion on the surface were the events considered in the model. The morphological evolution of the simulated film, Figure 28a, presented the same features as those observed in experimental SEM images [189] at a surface coverage of about 30%, Li_2S molecules form isolated islands; then these islands start to coalescence at a coverage of approximately 50%, and at coverages of 90% a continuous film is observed on the carbon substrate. A 3D kMC model with a Variable Step Size Method (VSSM) algorithm was applied by Thangavel et al. [190] to study a sulfur/carbon composite cathode. Four reaction events were contemplated.
Sulfur solvation:

$$S_{8\,(s)} \rightarrow S_{8(l)} \tag{53}$$

Reduction reactions:

$$S_{8\,(l)} + 4e^- \rightarrow 2S_{4\,(l)}^{2-} \quad (54)$$

$$S_{4\,(l)}^{2-} + 2e^- \rightarrow 2S_{2\,(l)}^{2-} \quad (55)$$

Electrodeposition:

$$2S_{2\,(l)}^{2-} + 4Li^+ + 2e^- \rightarrow 2Li_2S_{(s)} \quad (56)$$

Rate constants for Equations (54-56) were written in terms of the discharge current.

$$\Gamma_{red} = \frac{i}{ne}\Theta(\delta_e) \quad (57)$$

where i is the current from the discharge, n is the number of electrons transferred, and e the fundamental charge. $\Theta(\delta_e)$ is the electron tunneling probability, which depends on the tunneling distance δ_e from cathode surface.
Each solvated species was allowed to diffuse in 6 directions with the Stokes Einstein's equation:

$$\Gamma_{diff} = \frac{k_B T}{6\pi\rho r_i z^2} \quad (58)$$

where ρ is the viscosity of the solvent, r_i is the radius of gyration of the solvated *I* particle and z is a distance for particle motion.
Figure 28b shows results obtained by Thangavel et al. work for two discharge C-rates: C/2 (solid lines) and 2C (dashed line). Figure 28c shows snapshots of the Li_2S evolution for the data of Figure 28b.

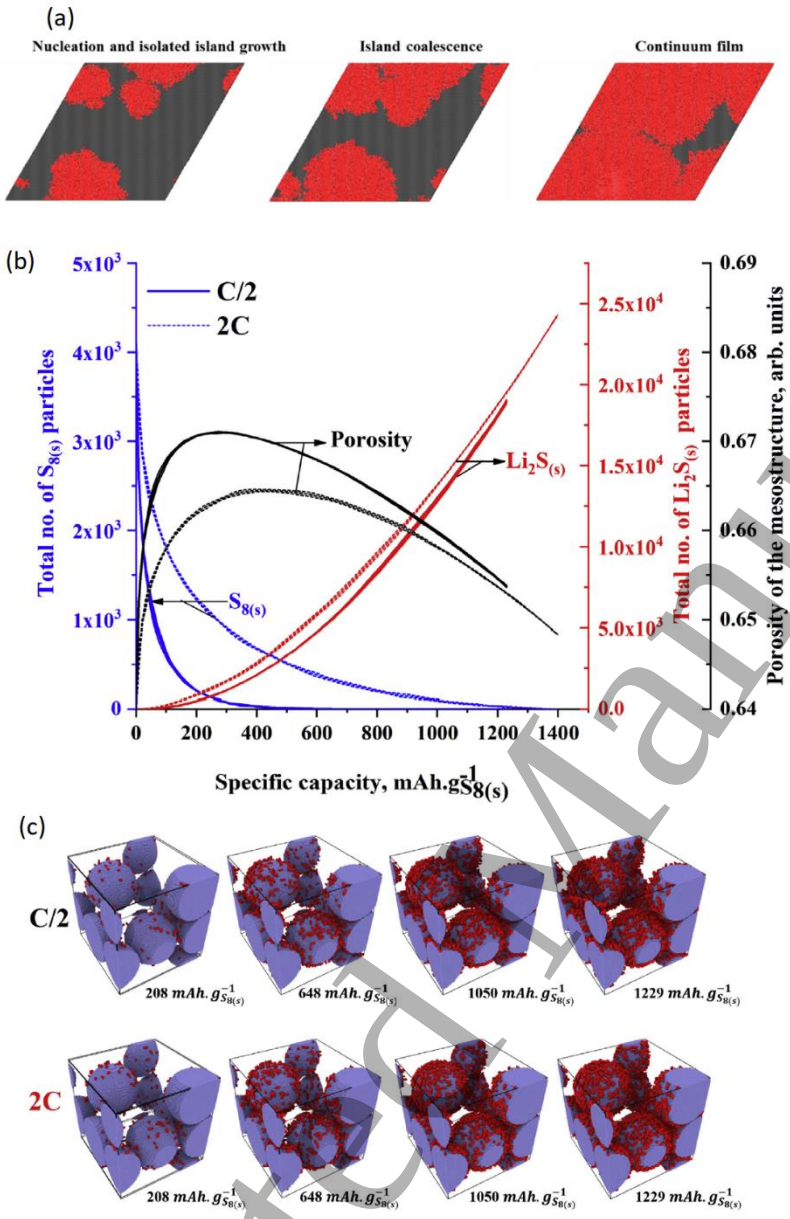

Figure 28: (a) Morphology of Li_2S (in red) at different precipitation stages. Reproduced with permission from ref [188]. Copyright 2017 American Chemical Society. (b) Total number of $S_{8(s)}$ particles, porosity and $Li_2S_{(s)}$ evolution for the two C-rates, indicated in the Figure. (c) $Li_2S_{(s)}$ (red particles) evolution on the mesoporous cathode material. Reproduced with permission from ref [190]. Copyright 2019 Elsevier B.V.

7. State-of-the-art and perspectives within the multiscale approach

As we have seen throughout this review, it becomes clear that the coupling between first-principles and atomistic kMC scales has been one of the most widely used multiscale tools over the years. The most popular strategy has been the use of DFT to calculate the activation energies of the different events, which are then used to implement kMC simulations. However, in recent years, new

multiscale schemes have been developed and implemented to deepen the study of rechargeable batteries. This evolution has two possibly dissimilar but equally demanding sources: the growing energy industry related to LIBs and the strong influence of different length and time scales in the performance of these devices.

Thorough reviews on multiscale modeling focused on LIBs have been recently given by Franco et al. [9,25] and Shi et al. [191]. In this section, we will briefly summarize the state-of-the-art of multiscale modeling involving kMC, with applications to Li-ion and Post-Li-ion batteries. We will focus on giving some details about the environment in which kMC may be embedded.

Li-based cells have the particularity of being devices presenting phenomena at different length and time scales. Their analysis requires different considerations that range from atomistic details, where detailed knowledge of the interaction between the particles is necessary, up to macroscopic features that characterize the electrode, separator, and electrolyte materials, like porosity, tortuosity, conductivity, viscosity, etc. This is so because in the electrochemical environment, the world of solid-state physics meets with the chemistry of solutions, and although in principle it could be thought that only bulky Li storage is important, interfaces are ubiquitous in batteries. Different kinetic processes at different lengths and timescales, occurring in Li-ion batteries, are shown schematically in Figure 29.

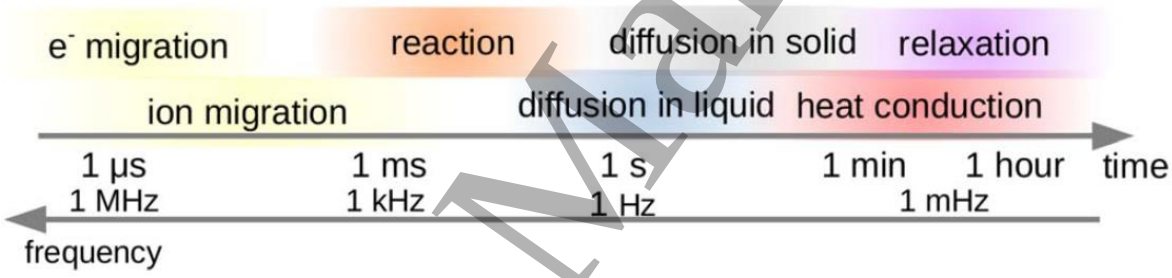

Figure 29: Different kinetic processes at different timescales. Reproduced with permission from ref [192]. Copyright 2018 The Electrochemical Society.

Different approaches individually cover a part of the wide range of length and time scales involved in the battery phenomenon. When put together, they may provide a unified and complete interpretation and overlap between them is necessary to ensure the accuracy of their predictions when going up in the time and length scales. Some of the simulation tools for this purpose are *first-principles calculations* at the quantum mechanical level; *molecular dynamics*, *mean-field*, *Monte Carlo* and *kinetic Monte Carlo* at the many-atoms scale; *phase field*, mesoscale *kinetic Monte Carlo*, coarse-grained *molecular dynamics,* and *discrete element method* for the mesoscale; and *numerical resolution of partial differential equations* at the largest scales.

The most important task when designing multiscale models is to reproduce, with the lowest computational cost and the highest fidelity, the phenomena that dictate the evolution of the system under consideration. A recent feature article by Leiva [193] briefly summarizes the most popular techniques implemented for lithium-ion battery modeling.

As discussed in section 4, Hin [141] devised a scheme to couple kMC with numerical continuum simulations. The model described Li^+ mobility in the electrolyte with a finite differences method, and charge transfer and evolution of Li^+ phases inside the electrode with kMC. Numerical resolution of differential equations and kMC were coupled at the electrode/electrolyte interface when

calculating the galvanostatic current. The local concentration of Li^+ was obtained using finite differences and rate constants for charge transfer were calculated with kMC. Similarly, in several articles a mesoscale implementation of kMC uses continuum equations connected with kMC events, as already seen in previous sections, for example, references [78,171]. Also, the works of Blanquer et al. [184], Thangavel et al. [190], and Yin et al. [186] provide interesting mesoscale kMC approaches for MSM of post-Li-ion cells.

Within the use of refined multiscale coupling algorithms, the works of Röder et al. [154,155] proposed a strategy to couple kMC with numerical simulations for battery applications. As mentioned in Section 5.1, SEI formation was studied with a multiscale algorithm that feeds kMC with continuum information (for example, potential values, surface fractions), while kMC output provides input data for continuum models (reaction rates, average SEI thickness). The steps performed in the multiscale procedure are shown in Figure 30. 1) The continuum model performs a time-step Δt, 2) the output of this simulation is then used as kMC input. kMC ends when Δt is reached. 3) Filters are used for smoothing kMC data. 4) The algorithm ends when some criteria are fulfilled, otherwise, smoothed kMC data is used to 5) predict the input for the continuum simulations in the next multiscale iteration. This procedure is also explained in reference [194]. General MSM strategies for coupling kMC with continuum equations for battery applications have been also proposed in the work of Röder et al. [195]. This work systematically compares different algorithms that are variations of the general idea presented previously [154,155].

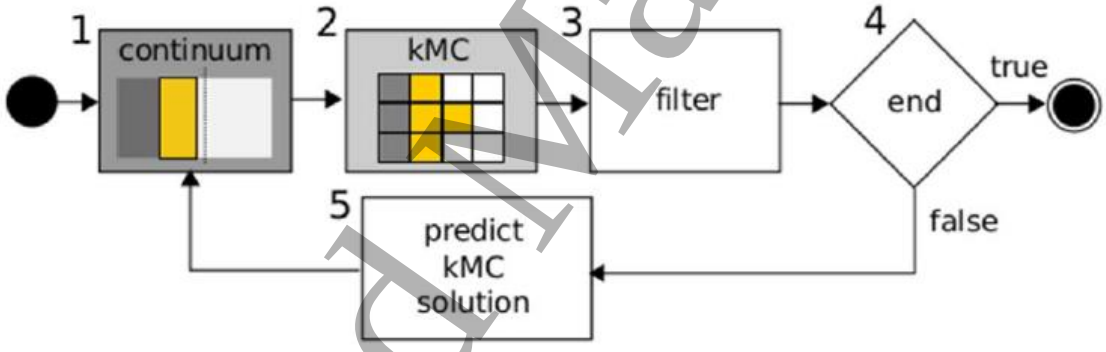

Figure 30: Scheme of the multiscale algorithm implemented by [154]. Reproduced with permission from ref [154]. Copyright 2017 The Electrochemical Society.

In a different approach, Shukla et al. [196] studied Si/C suspensions in electrolytes for slurry battery design, during the discharge cycle under galvanostatic conditions. The mesoscale model is shown in Figure 31. First, C and Si particles suspended in an electrolyte, located in a lattice next to a current collector, are randomly distributed Figure 31a. Silicon lithiation increases the particle volume, while carbon particles are considered to be conductive and connect Si isolated particles to make them electroactive. When Si is fully lithiated, the particle is considered inactive. The model only considers Brownian motion, using kMC to describe mass transport in the suspension Figure 31b. Electroactive Si particles must be identified, as well as the short conductive path for electrons Figure 31c (i). The amount of charge transferred is estimated for each time step. The charge is accumulated and the potential is calculated. If the accumulated charge is enough, Si particles expand in volume. Brownian motion and discharge steps are alternated until a cut-off potential is reached.

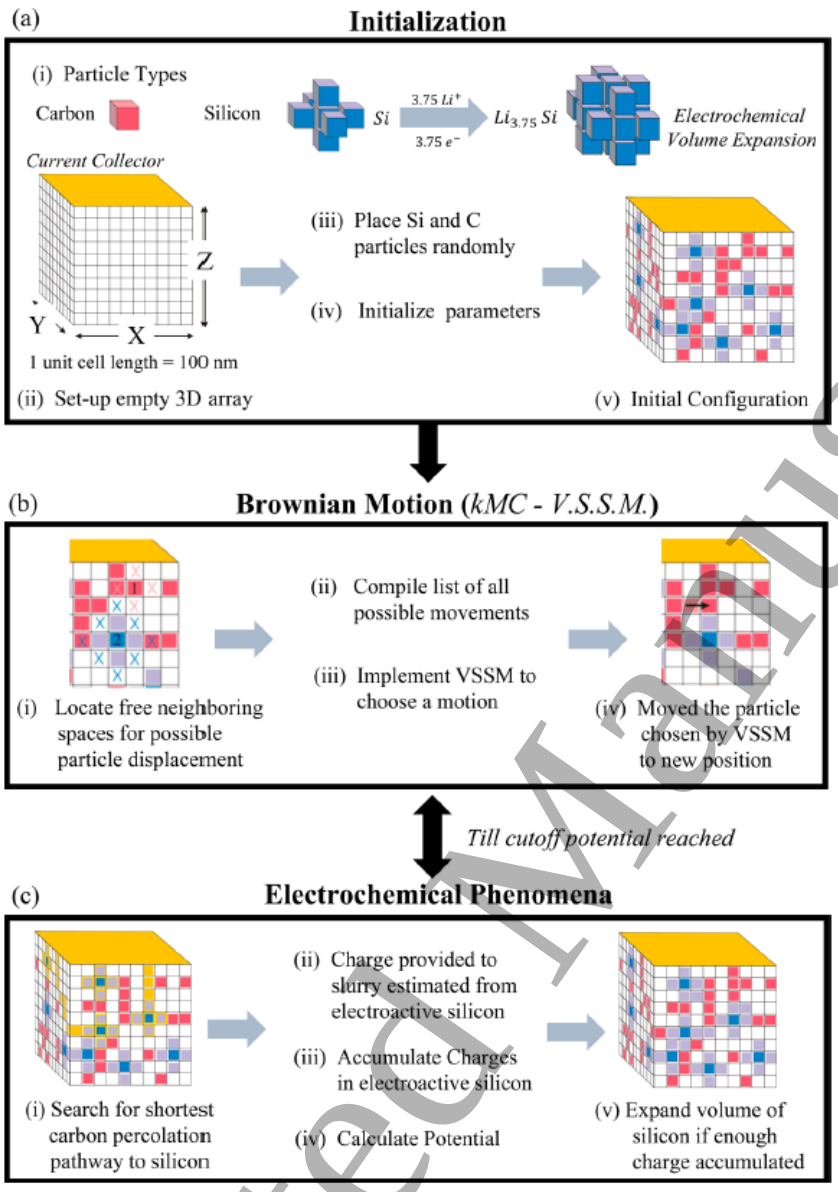

Figure 31: Multiscale Modelling (MSM) for Si lithiation during discharge in a suspension electrode composed of C particles (pink cubes), Si particles (blue cubes), electrolyte (white cubes), and a current collector (yellow). (a) initialization of the simulation box and setup of parameters, placing particles randomly. (b) Brownian motion simulated with kMC, steps (i-iv) are summarized in the figure. (c) electrochemical step and volume expansion of Si atoms; steps (i-v) are summarized in the figure. Reproduced with permission from ref [196]. Copyright 2017 American Chemical Society.

Mace et al. [197] have developed a MSM algorithm for Li-ion battery applications. In this work, diffusion coefficients were calculated in nanoporous materials. Starting from the structure of the storage material (Figure 32a), a 3D potential energy landscape was constructed (Figure 32b). In the case of Li-ion batteries, a solid electrolyte energy landscape can be obtained with a “pinball” model [198], using molecular dynamics. This denomination, due to the popular game, is used there to describe Li-ions moving in a “frozen” host. Then, using this energy grid, the energy basins, and transition states are identified with the TuTraSt algorithm presented in the work by Mace et al,

(Figure 32c). From these energy basins, a kMC lattice was constructed (Figure 32d) and the rate constants were calculated using both the energy basins and the transition state energies. Finally, kMC simulations were performed to calculate the diffusion coefficients.

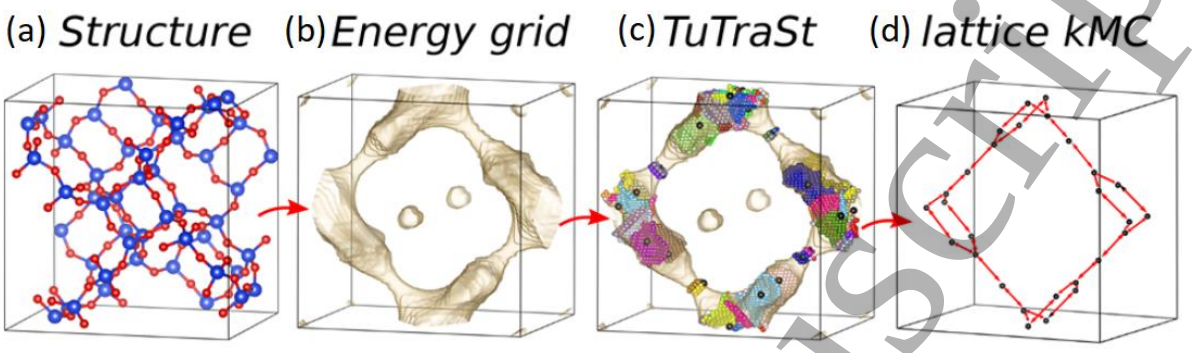

Figure 32: Schematic view of the lattice constructed with the TuTraSt algorithm from the energy landscape of a material. Reproduced with permission from ref [197]. Copyright 2019 American Chemical Society.

Sitapure et al. [180] combined kMC and MD simulations to study SEI formation and growth on metallic Li in different electrolytes. The electrolytes were simulated with MD using a reactive force field, and the events for diffusion and reactions to form the SEI were simulated with kMC. The results for this work were discussed in Section 6.1.

In recent years, machine learning (ML) strategies for solving complex physics problems have experienced an important growth, and the implementation of MSM coupled with ML will very probably constitute the goal for future theoretical and experimental researchers.

Machine-learning is a branch of Artificial Intelligence in computer science that is aimed to solve complex problems automatically. With this purpose, the algorithm learns patterns from a data set of information from both experimental and/or simulated sources, as crystal structures, energies, compositions, etc. The review made by Chen et al. [199] has summarized several technical issues and ML applications to energy materials.

A very interesting implementation of ML for battery applications is the construction of interatomic potentials from molecular structures. The idea is that the ML algorithm literally learns from the energy values provided by a reference, like first-principles calculations results, and then can predict energies from structures that were not included in the "training" step. The implementation of ML interatomic potentials presents the advantage of requiring less computational efforts than traditional DFT calculations and, thus, can be applied to simulate complex structures, like amorphous materials.

Inspired in the work of reference [200], Li et al. [165] implemented an ML potential to study an amorphous Li_3PO_4 electrolyte. The ML potential was used in kMC and MD simulations to study diffusion, finding an excellent agreement with DFT calculations. Recently, Panosetti et al. [201] have constructed a ML potential, using Density Functional Tight Binding (DFTB) as energy reference, to study Li^+ intercalation in graphite. The work used this potential to obtain diffusion energy barriers, showing the effectiveness of the proposed methodology to couple with atomistic simulations, like kMC. A DFT-based ML potential was used to predict the phase diagram of amorphous Li_xSi [202]. Bártok et al. have designed an ML-based potential for Si [203]. Other works have also focused on the design of ML interatomic potentials [204,205].

An interesting application of ML for MSM applied to the battery field, is the design of cluster expansion potentials, as discussed in the work of Cao et al. [206]. This work also discussed the kMC implementation of the cluster expansion algorithm.

The work of Bhowmik et al. [207], has recently discussed the need for strategies for coupling MSM, ML, and experimental data as a whole, to understand complex phenomena at battery interfaces. Figure 33, extracted from this work, shows a "big map" of the modelling and experimental techniques available to analyse LIB and post-Li-ion materials and interfaces, and the flow of information between them. This interconnection involves interpretation of the experimental information, input data for the models from these experiments, validation of the models based on their ability to predict the experiments, and input for the synthesis. In this map, it can be seen that kMC plays a central role (marked with a dashed light blue circle), being the bridge between different simulation scales and filling the gap between simulations and several experimental techniques. The authors of this work proposed the use of ML to couple and utilize simultaneously the data from experimental techniques and simulation methods, for the "inverse design" of battery interfaces. Inverse design aims to create new materials with the desired properties, from the mapping of the properties of known materials from their compositions, structures, etc.

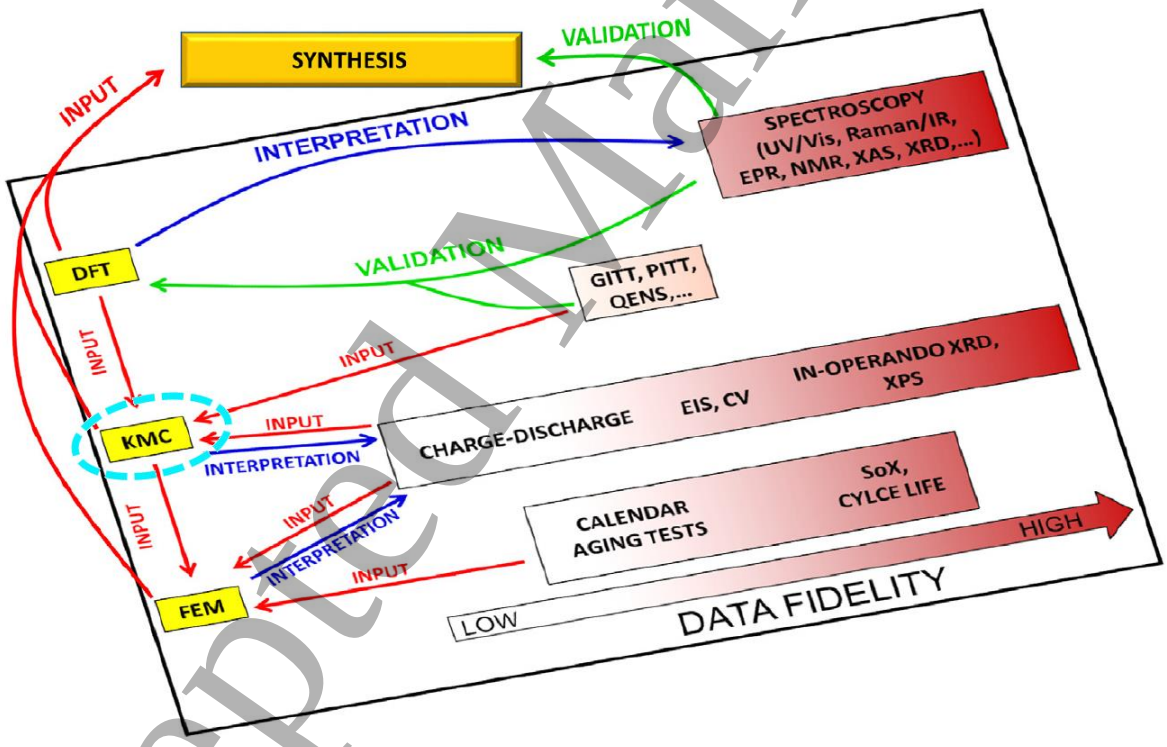

Figure 33: Different simulation scales and experimental techniques generally used to study battery materials and interfaces. The flux of information, like data input, validation of models and interpretation of the results, are represented with arrows. The central role of KMC (highlighted with a dashed light blue circle) in this complex scheme is evident. Reproduced with permission from ref [207]. Copyright 2019 Elsevier B.V.

8. Outlook and perspectives

The aim of the present review has been twofold: on one hand, it has been to provide to a wide electrochemical readership with the general foundations of kinetic Monte Carlo (kMC) (Section 2) and show that it is a simple methodology that can be used to bridge the gap between the atomistic scale and the world of partial differential equations (PDE) applied to the continuum scale. We have also provided starters in the field, such as advanced students, with some simple comprehensive criteria to test their early developments, comparing the atomistic description with results from its continuum counterpart (Section 2.3.)

On the other hand, considering a more specialized (but still broad) audience, we took a tour visiting several aspects of Li-ion and post-lithium cells to show the power that kMC has to describe many features of these systems. We started discussing simulations of Li^+ ion transport in bulk cathodes and anodes (Section 3.2 and 3.3, with a subsequent analysis of the validation of kMC by the experimental technique of step-isotope exchange). Then we turned to consider interfacial phenomena (Section 4), showing that kMC may be used to emulate the response of experimental systems to several techniques: potential and current steps, voltammetry, and electrochemical impedance spectroscopy. It was shown that other important parameters that can be used in PDE modeling like occupation-dependent diffusion coefficients and exchange current densities can be easily extracted from kMC simulations. The application of kMC to the solid electrolyte interphase (SEI) formation (Section 5.1) and Li^+ transport in an electrolyte (Section 5.2) was also discussed. Simulations of post lithium systems were analyzed in Section 6, and the connection with the problem of Li deposition on metallic Li anodes was addressed. A final discussion was given on the role of kMC in the context of multiscale modeling (MSM). To support our statement at the beginning of this outlook, we showed how kMC may play a central role to link continuum and atomistic modelling, and experimental results. We think that because of its comprehensive approach, the present review provides a suitable complement to recent MSM cited here.

Concerning future work in the area, we can identify some interesting aims:

- The complicated heterogeneous microkinetics of interfacial (electrode/electrolyte) and interphasial (SEI / electrode) phenomena during charge/discharge can be captured with kMC. Simulations considering these microscopic details are needed to validate the use of the ordinary Butler-Volmer approach to model exchange (or eventually develop more sophisticated and accurate transfer functions).
- Several uncertainties about diffusion kinetics during intercalation can be elucidated with kMC, allowing new models for the calculation of diffusion coefficients to be proposed. Kinetic Monte Carlo describes the entire complex scenario present in LIBs, naturally including details such as phase coexistence, finite-diffusion and different types of interactions, which are different or sometimes impossible to properly describe in simpler models.
- Related to the previous point, the implementation of kMC to emulate experimental electrochemical techniques may provide useful information for the interpretation of these results and the validation of simplified models. It can indicate important physical details that may be missing from simpler models. Insight into nanoscale and size-dependent behavior is also straightforward from kMC.
- On the experimental side, recent innovations in techniques showing the electrochemical behavior at the nanoscale (like computed tomography) will provide interesting feedback to the kMC results.
- The first steps have been taken to couple kMC with continuum models and mesoscale approaches. More work in this area is needed to take advantage of kMC in MSM.

- Many more applications of kMC to the emerging area of post-Li-ion cells are foreseen. As highlighted here, there are still very few applications of kMC to these systems.
- Machine Learning and MSM strongly emerge as multidisciplinary tools that will be applied to LIBs and post-Li systems. kMC will play the role of a central link within this simulation chain.

Acknowledgements

E.P.M. Leiva acknowledges grants PIP CONICET 11220150100624CO, PUE/2017 CONICET, FONCYT PICT-2015-1605 and SECyT of the Universidad Nacional de Córdoba. Support by CCAD-UNC and GPGPU Computing Group, Y-TEC and an IPAC grant from SNCAD-MinCyT, Argentina, are also gratefully acknowledged. M.P.M and H.E.H thank the Faraday Institution (https://faraday.ac.uk/; EP/S003053/1), grant number FIRG003, for funding.

References

[1] V. Etacheri, R. Marom, R. Elazari, G. Salitra, D. Aurbach, Challenges in the development of advanced Li-ion batteries: A review, Energy Environ. Sci. 4 (2011) 3243–3262. https://doi.org/10.1039/c1ee01598b.

[2] J.B. Goodenough, Y. Kim, Challenges for rechargeable Li batteries, Chem. Mater. 22 (2010) 587–603. https://doi.org/10.1021/cm901452z.

[3] J.B. Goodenough, K. Park, The Li-Ion Rechargeable Battery : A Perspective, (2013).

[4] M.R. Palacín, Recent advances in rechargeable battery materials: A chemist's perspective, Chem. Soc. Rev. 38 (2009) 2565–2575. https://doi.org/10.1039/b820555h.

[5] M.S. Islam, C.A.J. Fisher, Lithium and sodium battery cathode materials: Computational insights into voltage, diffusion and nanostructural properties, Chem. Soc. Rev. 43 (2014) 185–204. https://doi.org/10.1039/c3cs60199d.

[6] B. Scrosati, J. Hassoun, Y.K. Sun, Lithium-ion batteries. A look into the future, Energy Environ. Sci. 4 (2011) 3287–3295. https://doi.org/10.1039/c1ee01388b.

[7] X. Zeng, M. Li, D. Abd El-Hady, W. Alshitari, A.S. Al-Bogami, J. Lu, K. Amine, Commercialization of Lithium Battery Technologies for Electric Vehicles, Adv. Energy Mater. 9 (2019) 1–25. https://doi.org/10.1002/aenm.201900161.

[8] A. Van Der Ven, Z. Deng, S. Banerjee, S.P. Ong, Rechargeable Alkali-Ion Battery Materials: Theory and Computation, Chem. Rev. (2020). https://doi.org/10.1021/acs.chemrev.9b00601.

[9] A.A. Franco, A. Rucci, D. Brandell, C. Frayret, M. Gaberscek, P. Jankowski, P. Johansson, Boosting Rechargeable Batteries R&D by Multiscale Modeling: Myth or Reality?, Chem. Rev. 119 (2019) 4569–4627. https://doi.org/10.1021/acs.chemrev.8b00239.

[10] A. Ponrouch, M.R. Palacín, Post-Li batteries: promises and challenges, Philos. Trans. R. Soc. A Math. Phys. Eng. Sci. 377 (2019) 20180297. https://doi.org/10.1098/rsta.2018.0297.

[11] C.A. Calderón, A. Vizintin, J. Bobnar, D.E. Barraco, E.P.M. Leiva, A. Visintin, S. Fantini, F. Fischer, R. Dominko, Lithium Metal Protection by a Cross-Linked Polymer Ionic Liquid and Its Application in Lithium Battery, ACS Appl. Energy Mater. 3 (2020) 2020–2027. https://doi.org/10.1021/acsaem.9b02309.

[12] S.J. Zhang, Z.G. Gao, W.W. Wang, Y.Q. Lu, Y.P. Deng, J.H. You, J.T. Li, Y. Zhou, L. Huang, X.D. Zhou, S.G. Sun, A Natural Biopolymer Film as a Robust Protective Layer to Effectively Stabilize Lithium-Metal Anodes, Small. 14 (2018) 1–8. https://doi.org/10.1002/smll.201801054.

[13] P. Shi, X.Q. Zhang, X. Shen, R. Zhang, H. Liu, Q. Zhang, A Review of Composite Lithium Metal Anode for Practical Applications, Adv. Mater. Technol. 5 (2020). https://doi.org/10.1002/admt.201900806.

[14] J. Asenbauer, T. Eisenmann, M. Kuenzel, A. Kazzazi, Z. Chen, D. Bresser, The success story of graphite as a lithium-ion anode material-fundamentals, remaining challenges, and recent developments including silicon (oxide) composites, Sustain. Energy Fuels. 4 (2020) 5387–5416. https://doi.org/10.1039/d0se00175a.

[15] H. Zhang, Y. Yang, D. Ren, L. Wang, X. He, Graphite as anode materials: Fundamental mechanism, recent progress and advances, Energy Storage Mater. 36 (2021) 147–170. https://doi.org/10.1016/j.ensm.2020.12.027.

[16] M.A. Rahman, X. Wang, C. Wen, A review of high energy density lithium-air battery technology, J. Appl. Electrochem. 44 (2014) 5–22. https://doi.org/10.1007/s10800-013-0620-8.

[17] Z. Ma, X. Yuan, L. Li, Z.-F. Ma, D.P. Wilkinson, L. Zhang, J. Zhang, A review of cathode materials and structures for rechargeable lithium–air batteries, Energy Environ. Sci. 8 (2015) 2144–2198. https://doi.org/10.1039/C5EE00838G.

[18] X.-Q. Zhang, C. Liu, Y. Gao, J.-M. Zhang, Y.-Q. Wang, Research Progress of Sulfur/Carbon Composite Cathode Materials and the Corresponding Safe Electrolytes for Advanced Li-S Batteries, Nano. 15 (2020) 2030002. https://doi.org/10.1142/S1793292020300029.

[19] P. Tan, H.R. Jiang, X.B. Zhu, L. An, C.Y. Jung, M.C. Wu, L. Shi, W. Shyy, T.S. Zhao, Advances and challenges in lithium-air batteries, Appl. Energy. 204 (2017) 780–806. https://doi.org/10.1016/j.apenergy.2017.07.054.

[20] X. Zhao, G. Cheruvally, C. Kim, K.-K. Cho, H.-J. Ahn, K.-W. Kim, J.-H. Ahn, Lithium/Sulfur Secondary Batteries: A Review, J. Electrochem. Sci. Technol. 7 (2016) 97–114. https://doi.org/10.33961/jecst.2016.7.2.97.

[21] D.T. Gillespie, A general method for numerically simulating the stochastic time evolution of coupled chemical reactions, J. Comput. Phys. 22 (1976) 403–434. https://doi.org/10.1016/0021-9991(76)90041-3.

[22] K.A. Fichthorn, W.H. Weinberg, Theoretical Foundations of Dynamic Monte-Carlo Simulations, J. Chem. Phys. 95 (1991) 1090–1096. https://doi.org/10.1063/1.461138.

[23] M.D. Levi, E. a. Levi, D. Aurbach, The mechanism of lithium intercalation in graphite film electrodes in aprotic media. Part 2. Potentiostatic intermittent titration and in situ XRD studies of the solid-state ionic diffusion, J. Electroanal. Chem. 421 (1997) 89–97. https://doi.org/10.1016/S0022-0728(96)04833-4.

[24] J. Deppe, R.F. Wallis, I. Nachev, M. Balkanski, Two-dimensional hopping diffusion across material interfaces, J. Phys. Chem. Solids. 55 (1994) 759–766. https://doi.org/10.1016/0022-3697(94)90028-0.

[25] A.A. Franco, Multiscale modelling and numerical simulation of rechargeable lithium ion batteries: concepts, methods and challenges, RSC Adv. 3 (2013) 13027–13058. https://doi.org/10.1039/c3ra23502e.

[26] M.A. Snyder, A. Chatterjee, D.G. Vlachos, Net-event kinetic Monte Carlo for overcoming stiffness in spatially homogeneous and distributed systems, 29 (2005) 701–712. https://doi.org/10.1016/j.compchemeng.2004.09.016.

[27] A. Chatterjee, D.G. Vlachos, An overview of spatial microscopic and accelerated kinetic Monte Carlo methods, J Comput. Mater Des. 14 (2007) 253–308. https://doi.org/10.1007/s10820-006-9042-9.

[28] V.I. Tokar, H. Dreyssé, Accelerated kinetic Monte Carlo algorithm for diffusion-limited kinetics, Phys. Rev. E - Stat. Nonlinear, Soft Matter Phys. 77 (2008) 10–13.

https://doi.org/10.1103/PhysRevE.77.066705.
[29] A. Chatterjee, A.F. Voter, Accurate acceleration of kinetic Monte Carlo simulations through the modification of rate constants, J. Chem. Phys. 132 (2010). https://doi.org/10.1063/1.3409606.
[30] B. Puchala, M.L. Falk, K. Garikipati, An energy basin finding algorithm for kinetic Monte Carlo acceleration, J. Chem. Phys. 132 (2010) 1–14. https://doi.org/10.1063/1.3369627.
[31] E.C. Dybeck, C.P. Plaisance, M. Neurock, Generalized Temporal Acceleration Scheme for Kinetic Monte Carlo Simulations of Surface Catalytic Processes by Scaling the Rates of Fast Reactions, J. Chem. Theory Comput. 13 (2017) 1525–1538. https://doi.org/10.1021/acs.jctc.6b00859.
[32] W.R. Saunders, J. Grant, E.H. Müller, I. Thompson, Fast electrostatic solvers for kinetic Monte Carlo simulations, J. Comput. Phys. 410 (2020) 109379. https://doi.org/10.1016/j.jcp.2020.109379.
[33] A.F. Voter, INTRODUCTION TO THE KINETIC MONTE CARLO METHOD, in: K.E. Sickafus, E.A. Kotomin, B.P. Uberuaga (Eds.), Radiat. Eff. Solids, Springe, 2007: pp. 1–23. https://doi.org/10.1007/978-1-4020-5295-8_1.
[34] M. Andersen, C. Panosetti, K. Reuter, A practical guide to surface kinetic Monte Carlo simulations, Front. Chem. 7 (2019) 1–24. https://doi.org/10.3389/fchem.2019.00202.
[35] P. Kratzer, Monte Carlo and Kinetic Monte Carlo Methods – A Tutorial, NIC Ser. 42 (2009) 51–76. http://www.fz-juelich.de/nic-series/volume42.
[36] P. Muñoz, ESTUDIOS DE SISTEMAS VEHICULARES DE EMISIÓN CERO Y MODELADO DE BATERÍAS LIFEPO4 PARA APLICACIONES EN SISTEMAS DE TRANSPORTE TERRESTRE, UNIVERSIDAD NACIONAL DE CÓRDOBA, FACULTAD DE CIENCIAS EXACTAS, FÍSICAS Y NATURALES, 2019. https://rdu.unc.edu.ar/handle/11086/12734.
[37] E.M. Gavilán-Arriazu, O.A. Pinto, B.A.L. de Mishima, E.P.M. Leiva, O.A. Oviedo, Grand Canonical Monte Carlo Study of Li Intercalation into Graphite, J. Electrochem. Soc. 165 (2018) A2019–A2025. https://doi.org/10.1149/2.1211809jes.
[38] M.P. Mercer, S. Finnigan, D. Kramer, D. Richards, H.E. Hoster, The influence of point defects on the entropy profiles of Lithium Ion Battery cathodes: a lattice-gas Monte Carlo study, Electrochim. Acta. 241 (2017) 141–152. https://doi.org/10.1016/j.electacta.2017.04.115.
[39] E.P.M. Leiva, E. Perassi, D. Barraco, Shedding Light on the Entropy Change Found for the Transition Stage II→Stage I of Li-Ion Storage in Graphite, J. Electrochem. Soc. 164 (2017) A6154–A6157. https://doi.org/10.1149/2.0231701jes.
[40] M. Otero, A. Sigal, E.M. Perassi, D. Barraco, E.P.M. Leiva, Statistical mechanical modeling of the transition Stage II → Stage I of Li-ion storage in graphite. A priori vs induced heterogeneity, Electrochim. Acta. 245 (2017) 569–574. https://doi.org/10.1016/j.electacta.2017.05.128.
[41] S. Schlueter, R. Genieser, D. Richards, H.E. Hoster, M.P. Mercer, Quantifying structure dependent responses in Li-ion cells with excess Li spinel cathodes: Matching voltage and entropy profiles through mean field models, Phys. Chem. Chem. Phys. 20 (2018) 21417–21429. https://doi.org/10.1039/c8cp02989j.
[42] M.P. Mercer, M. Otero, M. Ferrer-Huerta, A. Sigal, D.E. Barraco, H.E. Hoster, E.P.M. Leiva, Transitions of lithium occupation in graphite: A physically informed model in the dilute lithium occupation limit supported by electrochemical and thermodynamic measurements, Electrochim. Acta. 324 (2019) 134774. https://doi.org/10.1016/j.electacta.2019.134774.
[43] T. Hill, An Introduction to Statistical Thermodynamics, Dover Publications Inc, 2003.
[44] Y. Reynier, R. Yazami, B. Fultz, The entropy and enthalpy of lithium intercalation into graphite, J. Power Sources. 119–121 (2003) 850–855. https://doi.org/10.1016/S0378-

7753(03)00285-4.
[45] Y. Reynier, J. Graetz, T. Swan-Wood, P. Rez, R. Yazami, B. Fultz, Entropy of Li intercalation in LixCoO2, Phys. Rev. B - Condens. Matter Mater. Phys. 70 (2004) 1–7. https://doi.org/10.1103/PhysRevB.70.174304.
[46] S. Kim, S. Pyun, Thermodynamic and kinetic approaches to lithium intercalation into a Li1−δMn2O4 electrode using Monte Carlo simulation, Electrochim. Acta. 46 (2001) 987–997.
[47] M.P. Mercer, C. Peng, C. Soares, H.E. Hoster, D. Kramer, Voltage hysteresis during lithiation/delithiation of graphite associated with meta-stable carbon stackings, J. Mater. Chem. A. 9 (2021) 492–504. https://doi.org/10.1039/d0ta10403e.
[48] E.M. Perassi, E.P.M. Leiva, A theoretical model to determine intercalation entropy and enthalpy: Application to lithium/graphite, Electrochem. Commun. 65 (2016) 48–52. https://doi.org/10.1016/j.elecom.2016.02.003.
[49] J. Filhol, C. Combelles, R. Yazami, M. Doublet, I. Charles, G.C.- Universite, Phase Diagrams for Systems with Low Free Energy Variation : A Coupled Theory / Experiments Method Applied to Li-Graphite, Ournal Phys. Chem. C. 6 (2008) 3982–3988.
[50] K.E. Thomas, J. Newman, Heats of mixing and of entropy in porous insertion electrodes, J. Power Sources. 119–121 (2003) 844–849. https://doi.org/10.1016/S0378-7753(03)00283-0.
[51] N. Metropolis, A.W. Rosenbluth, M.N. Rosenbluth, A.H. Teller, E. Teller, Equation of state calculations by fast computing machines, J. Chem. Phys. 21 (1953) 1087–1092. https://doi.org/http://dx.doi.org/10.1063/1.1699114.
[52] N. Metropolis, S. Ulam, The Monet Carlo Method, J. Am. Stat. Assoc. 44 (1949) 335–341.
[53] N. Metropolis, The beginning of the Monte Carlo method, Los Alamos Sci. (1987 Spec. Issue Dedic. to Stanislaw Ulam). (1987) 125–130.
[54] R.L. Strawderman, Monte Carlo Methods in Statistical Physics, J. Am. Stat. Assoc. 96 (2001) 778–778. https://doi.org/10.1198/jasa.2001.s394.
[55] D.P. Landau, K. Binder, A Guide to Monte Carlo Simulations in Statistical Physics , Second Edition, 2000.
[56] K. Binder, Monte Carlo Methods in Statistical Physics (Topics in Current Physics), Springer, Berlin, 1978.
[57] P.A. Derosa, P.B. Balbuena, A Lattice-Gas Model Study of Lithium Intercalation in Graphite, J. Electrochem. Soc. 146 (1999) 3630. https://doi.org/10.1149/1.1392525.
[58] W.C. Wong, J. Newman, Monte Carlo Simulation of the Open-Circuit Potential and the Entropy of Reaction in Lithium Manganese Oxide, J. Electrochem. Soc. 149 (2002) A493. https://doi.org/10.1149/1.1459714.
[59] E.M. Gavilán Arriazu, B.A. López de Mishima, O.A. Oviedo, E.P.M. Leiva, O.A. Pinto, Criticality of the phase transition on stage two in a lattice-gas model of a graphite anode in a lithium-ion battery, Phys. Chem. Chem. Phys. 19 (2017) 23138–23145. https://doi.org/10.1039/C7CP04253A.
[60] J. Rossat-Mignod, A. Wiedenmann, Laboratoire, K.C. Woo, J.W. Milliken, J.E. Fischer, First-order phase transition in the graphite compound LiC6, Solid State Commun. 44 (1982) 1339–1342.
[61] E.M. Gavilán Arriazu, J.M. Hümöller, O.A. Pinto, B. López de Mishima, E.P.M. Leiva, O.A.A. Oviedo, Fractional and integer stages of lithium ion-graphite systems. The role of electrostatic and elastic contributions., Phys. Chem. Chem. Phys. (2020). https://doi.org/10.1039/D0CP01886D.
[62] V.I. Kalikmanov, S.W. De Leeuw, Role of elasticity forces in thermodynamics of intercalation

compounds: Self-consistent mean-field theory and Monte Carlo simulations, J. Chem. Phys. 116 (2002) 3083–3089. https://doi.org/10.1063/1.1436472.

[63] J.R. Dahn, D.C. Dahn, R.R. Haering, Elastic energy and staging in intercalation compounds, Solid State Commun. 42 (1982) 179–183. https://doi.org/10.1016/0038-1098(82)90999-1.

[64] K. Persson, Y. Hinuma, Y. Meng, A. Van der Ven, G. Ceder, Thermodynamic and kinetic properties of the Li-graphite system from first-principles calculations, Phys. Rev. B. 82 (2010) 1–9. https://doi.org/10.1103/PhysRevB.82.125416.

[65] A. Van Der Ven, C. Marianetti, D. Morgan, G. Ceder, Phase transformations and volume changes in spinel LixMn2O4, Solid State Ionics. 135 (2000) 21–32. https://doi.org/10.1016/S0167-2738(00)00326-X.

[66] F.A. Soto, P.B. Balbuena, Elucidating Oligomer-Surface and Oligomer-Oligomer Interactions at a Lithiated Silicon Surface, Electrochim. Acta. 220 (2016) 312–321. https://doi.org/10.1016/j.electacta.2016.10.082.

[67] C. Heath Turner, Z. Zhang, L.D. Gelb, B.I. Dunlapc, Kinetic Monte Carlo Simulation of Electrochemical Systems, Rev. Comput. Chem. 28 (2015) 175–204. https://doi.org/10.1002/9781118889886.ch5.

[68] Y. Xin, A. Huang, Q. Hu, H. Shi, M. Wang, Z. Xiao, X. Zheng, Z. Di, P.K. Chu, Barrier Reduction of Lithium Ion Tunneling through Graphene with Hybrid Defects : First-Principles Calculations, Adv. Theory Simulations. 1 (2018) 1700009. https://doi.org/10.1002/adts.201700009.

[69] P. Pechukas, Transition State Theory, Annu. Rev. Phys. Chem. 32 (1981) 159–177. https://doi.org/10.1146/annurev.pc.32.100181.001111.

[70] K.J. Laidler, M.C. King, The development of transition-state theory, J. Phys. Chem. 87 (1983) 2657–2664. https://doi.org/10.1021/j100238a002.

[71] P. Hänggi, P. Talkner, M. Borkovec, Reaction-rate theory: Fifty years after Kramers, Rev. Mod. Phys. 62 (1990) 251–341. https://doi.org/10.1103/RevModPhys.62.251.

[72] A.J. Bard, L.R. Faulkner, Electrochemical Methods : Fundamentals and Applications, 2001.

[73] S.J. Mitchell, G. Brown, P.A. Rikvold, Dynamics of Br electrosorption on single-crystal Ag(100): A computational study, J. Electroanal. Chem. 493 (2000) 68–74. https://doi.org/10.1016/S0022-0728(00)00296-5.

[74] G. Brown, P.A. Rikvold, M.A. Novotny, A. Wieckowski, Simulated Dynamics of Underpotential Deposition of Cu with Sulfate on Au(111), J. Electrochem. Soc. 146 (1999) 1035–1040. https://doi.org/10.1149/1.1391717.

[75] S. Il Pyun, S.W. Kim, J.M. Ko, Lithium Transport through a Sol-Gel Derived Li1-δMn2O4 Film Electrode : Analysis of Current Transient by Monte Carlo Simulation, J. New Mater. Electrochem. Syst. 5 (2002) 135–141.

[76] S.J. Mitchell, G. Brown, P.A. Rikvold, Static and dynamic Monte Carlo simulations of Br electrodeposition on Ag(1 0 0), Surf. Sci. 471 (2001) 125–142. https://doi.org/10.1016/S0039-6028(00)00892-X.

[77] G. Brown, P.A. Rikvold, S.J. Mitchell, M. a. Novotny, Monte Carlo Methods for Equilibrium and Nonequilibrium Problems in Interfacial Electrochemistry, Computer (Long. Beach. Calif). (1998) 14. http://arxiv.org/abs/cond-mat/9805126.

[78] F. Hao, Z. Liu, P.B. Balbuena, P.P. Mukherjee, Mesoscale Elucidation of Solid Electrolyte Interphase Layer Formation in Li-Ion Battery Anode, J. Phys. Chem. C. 121 (2017) 26233–26240. https://doi.org/10.1021/acs.jpcc.7b09465.

[79] H. Mehrer, Diffusion in Solids, Springer Berlin Heidelberg, Berlin, Heidelberg, 2007. https://doi.org/10.1007/978-3-540-71488-0.

[80] D.A. Reed, G. Ehrlich, Surface diffusion, atomic jump rates and thermodynamics, Surf. Sci.

102 (1981) 588–609. https://doi.org/10.1016/0039-6028(81)90048-0.

[81] C. Montella, Discussion of the potential step method for the determination of the diffusion coefficients of guest species in host materials, J. Electroanal. Chem. 518 (2002) 61–83. https://doi.org/10.1016/S0022-0728(01)00691-X.

[82] E.M. Gavilán-Arriazu, O.A. Pinto, B.A. López de Mishima, D.E. Barraco, O.A. Oviedo, E.P.M. Leiva, Kinetic Monte Carlo applied to the electrochemical study of the Li-ion graphite system, Electrochim. Acta. 331 (2020) 135439. https://doi.org/10.1016/j.electacta.2019.135439.

[83] J. Xie, K. Kohno, T. Matsumura, N. Imanishi, A. Hirano, Y. Takeda, O. Yamamoto, Li-ion diffusion kinetics in LiMn2O4 thin films prepared by pulsed laser deposition, Electrochim. Acta. 54 (2008) 376–381. https://doi.org/10.1016/j.electacta.2008.07.067.

[84] M.D. Levi, D. Aurbach, Diffusion coefficients of lithium ions during intercalation into graphite derived from the simultaneous measurements and modeling of electrochemical impedance and potentiostatic intermittent titration characteristics of thin graphite electrodes, J. Phys. Chem. B. 101 (1997) 4641–4647. https://doi.org/10.1021/jp9701911.

[85] K. Wen, M. Xia, P. Deng, W. Lv, W. He, A sandwich-structured double-battery device for direct evaluation of lithium diffusion coefficients and phase transition in electrodes of lithium ion batteries, Chem. Eng. Sci. 200 (2019) 80–86. https://doi.org/10.1016/j.ces.2019.01.062.

[86] C.-H. Chen, F. Brosa Planella, K. O'Regan, D. Gastol, W.D. Widanage, E. Kendrick, Development of Experimental Techniques for Parameterization of Multi-scale Lithium-ion Battery Models, J. Electrochem. Soc. 167 (2020) 080534. https://doi.org/10.1149/1945-7111/ab9050.

[87] M.W. Verbrugge, B.J. Koch, Modeling Lithium Intercalation of Single-Fiber Carbon Microelectrodes, J. Electrochem. Soc. 143 (1996) 600–608. https://doi.org/10.1149/1.1836486.

[88] K. Tang, X. Yu, J. Sun, H. Li, X. Huang, Kinetic analysis on LiFePO4 thin films by CV, GITT, and EIS, Electrochim. Acta. 56 (2011) 4869–4875. https://doi.org/10.1016/j.electacta.2011.02.119.

[89] M.D. Levi, D. Aurbach, Potentiostatic and Galvanostatic Intermittent Titration Techniques, Charact. Mater. (2012) 913–932. https://doi.org/10.1002/0471266965.com125.

[90] Q. Wang, H. Li, X. Huang, L. Chen, Determination of Chemical Diffusion Coefficient of Lithium Ion in Graphitized Mesocarbon Microbeads with Potential Relaxation Technique, J. Electrochem. Soc. 148 (2001) A737. https://doi.org/10.1149/1.1377897.

[91] A. V. Churikov, A. V. Ivanischev, Application of pulse methods to the determination of the electrochemical characteristics of lithium intercalates, Electrochim. Acta. 48 (2003) 3677–3691. https://doi.org/10.1016/S0013-4686(03)00505-X.

[92] M. Ecker, T.K.D. Tran, P. Dechent, S. Käbitz, A. Warnecke, D.U. Sauera, Parameterization of a physico-chemical model of a lithium-ion battery: I. Determination of parameters, J. Electrochem. Soc. 162 (2015) A1836–A1848. https://doi.org/10.1149/2.0551509jes.

[93] L. Pfaffmann, C. Birkenmaier, M. Müller, W. Bauer, F. Scheiba, T. Mitsch, J. Feinauer, Y. Kr, A. Hintennach, T. Schleid, V. Schmidt, H. Ehrenberg, Investigation of the electrochemically active surface area and lithium diffusion in graphite anodes by a novel OsO 4 staining method, J. Power Sources. 307 (2016) 762–771. https://doi.org/10.1016/j.jpowsour.2015.12.085.

[94] I. Umegaki, S. Kawauchi, H. Sawada, H. Nozaki, Y. Higuchi, K. Miwa, Y. Kondo, M. Månsson, M. Telling, F.C. Coomer, S.P. Cottrell, T. Sasaki, T. Kobayashi, J. Sugiyama, Li-ion diffusion in Li intercalated graphite C6Li and C12Li probed by μ+SR, Phys. Chem. Chem. Phys. 19 (2017)

19058–19066. https://doi.org/10.1039/c7cp02047c.
[95] N. Kuwata, G. Hasegawa, D. Maeda, N. Ishigaki, T. Miyazaki, J. Kawamura, Tracer Diffusion Coefficients of Li Ions in LixMn2O4Thin Films Observed by Isotope Exchange Secondary Ion Mass Spectrometry, J. Phys. Chem. C. 124 (2020) 22981–22992. https://doi.org/10.1021/acs.jpcc.0c06375.
[96] R. Darling, J. Newman, Dynamic Monte Carlo simulations of diffusion in LiyMn2O4, J. Electrochem. Soc. 146 (1999) 3765–3772. https://doi.org/Doi 10.1149/1.1392547.
[97] Y. Gao, J.N. Reimers, J.R. Dahn, Changes in the voltage profiles of Li/Li 1-xMn2-xO4 cells as a function of x, Phys. Rev. B. 54 (1996) 3878–3883. https://doi.org/10.1103/PhysRevB.54.3878.
[98] A. Van der Ven, G. Ceder, M. Asta, P.D. Tepesch, First-principles theory of ionic diffusion with nondilute carriers, Phys. Rev. B. 64 (2001) 1–17. https://doi.org/10.1103/PhysRevB.64.184307.
[99] J.M. Sanchez, F. Ducastelle, D. Gratias, Generalized cluster description of multicomponent systems, Phys. A Stat. Mech. Its Appl. 128 (1984) 334–350. https://doi.org/10.1016/0378-4371(84)90096-7.
[100] A. Van Der Ven, J.C. Thomas, Q. Xu, B. Swoboda, D. Morgan, Nondilute diffusion from first principles : Li diffusion in Li x TiS 2, (2008) 1–12. https://doi.org/10.1103/PhysRevB.78.104306.
[101] J. Bhattacharya, A. Van Der Ven, Phase stability and nondilute Li diffusion in spinel Li 1+xTi2O4, Phys. Rev. B - Condens. Matter Mater. Phys. 81 (2010) 27–30. https://doi.org/10.1103/PhysRevB.81.104304.
[102] H. Liu, M.J. Choe, R.A. Enrique, B. Orvañanos, L. Zhou, T. Liu, K. Thornton, C.P. Grey, Effects of Antisite Defects on Li Diffusion in LiFePO4 Revealed by Li Isotope Exchange, J. Phys. Chem. C. 121 (2017) 12025–12036. https://doi.org/10.1021/acs.jpcc.7b02819.
[103] A.O. Boev, S.S. Fedotov, A.M. Abakumov, K.J. Stevenson, G. Henkelman, D.A. Aksyonov, The role of antisite defect pairs in surface reconstruction of layered AMO2 oxides: A DFT+U study, Appl. Surf. Sci. 537 (2021). https://doi.org/10.1016/j.apsusc.2020.147750.
[104] J. Yu, M.L. Sushko, S. Kerisit, K.M. Rosso, J. Liu, Kinetic Monte Carlo study of ambipolar lithium ion and electron-polaron diffusion into nanostructured TiO 2, J. Phys. Chem. Lett. 3 (2012) 2076–2081. https://doi.org/10.1021/jz300562v.
[105] M. V. Koudriachova, N.M. Harrison, S.W. De Leeuw, Effect of diffusion on Lithium intercalation in titanium dioxide, Phys. Rev. Lett. 86 (2001) 1275–1278. https://doi.org/10.1103/PhysRevLett.86.1275.
[106] N.A. Deskins, M. Dupuis, Electron transport via polaron hopping in bulk Ti O2: A density functional theory characterization, Phys. Rev. B - Condens. Matter Mater. Phys. 75 (2007) 1–10. https://doi.org/10.1103/PhysRevB.75.195212.
[107] S. Kerisit, K.M. Rosso, Z. Yang, J. Liu, Dynamics of coupled lithium/electron diffusion in TiO2 polymorphs, J. Phys. Chem. C. 113 (2009) 20998–21007. https://doi.org/10.1021/jp9064517.
[108] J. Moon, B. Lee, M. Cho, K. Cho, Ab initio and kinetic Monte Carlo simulation study of lithiation in crystalline and amorphous silicon, J. Power Sources. 272 (2014) 1010–1017. https://doi.org/10.1016/j.jpowsour.2014.09.004.
[109] C. Chang, X. Li, Z. Xu, Microstructure- and concentration-dependence of lithium diffusion in the silicon anode: Kinetic Monte Carlo simulations and complex network analysis, Appl. Phys. Lett. 113 (2018). https://doi.org/10.1063/1.5022334.
[110] G. Henkelman, B.P. Uberuaga, H. Jónsson, A climbing image nudged elastic band method for finding saddle points and minimum energy paths, J. Chem. Phys. 113 (2000) 9901–9904.

https://doi.org/10.1063/1.1329672.
[111] G.A. Tritsaris, K. Zhao, O.U. Okeke, E. Kaxiras, Diffusion of lithium in bulk amorphous silicon: A theoretical study, J. Phys. Chem. C. 116 (2012) 22212–22216. https://doi.org/10.1021/jp307221q.
[112] X. Yan, A. Gouissem, P. Sharma, Atomistic insights into Li-ion diffusion in amorphous silicon, Mech. Mater. 91 (2015) 306–312. https://doi.org/10.1016/j.mechmat.2015.04.001.
[113] L.K. Béland, P. Brommer, F. El-Mellouhi, J.F. Joly, N. Mousseau, Kinetic activation-relaxation technique, Phys. Rev. E - Stat. Nonlinear, Soft Matter Phys. 84 (2011) 1–13. https://doi.org/10.1103/PhysRevE.84.046704.
[114] F. Fan, S. Huang, H. Yang, M. Raju, D. Datta, V.B. Shenoy, A.C.T. Van Duin, S. Zhang, T. Zhu, Mechanical properties of amorphous LixSi alloys: A reactive force field study, Model. Simul. Mater. Sci. Eng. 21 (2013). https://doi.org/10.1088/0965-0393/21/7/074002.
[115] M. Trochet, N. Mousseau, Energy landscape and diffusion kinetics of lithiated silicon: A kinetic activation-relaxation technique study, Phys. Rev. B. 96 (2017). https://doi.org/10.1103/PhysRevB.96.134118.
[116] J. Moon, B. Lee, M. Cho, K. Cho, Ab initio and kinetic Monte Carlo study of lithium diffusion in LiSi, Li12Si7, Li13Si5 and Li15Si4, J. Power Sources. 328 (2016) 558–566. https://doi.org/10.1016/j.jpowsour.2016.07.092.
[117] S. Chang, J. Moon, K. Cho, M. Cho, Multiscale analysis of prelithiated silicon nanowire for Li-ion battery, Comput. Mater. Sci. 98 (2015) 99–104. https://doi.org/10.1016/j.commatsci.2014.11.001.
[118] K. Zhong, Y. Yang, G. Xu, J.M. Zhang, Z. Huangx, An ab initio and Kinetic Monte Carlo simulation study of lithium ion diffusion on graphene, Materials (Basel). 10 (2017). https://doi.org/10.3390/ma10070761.
[119] K. Zhong, R. Hu, G. Xu, Y. Yang, J.M. Zhang, Z. Huang, Adsorption and Ultrafast Diffusion of Lithium In Bilayer Graphene: Ab Initio and Kinetic Monte Carlo Simulation Study, ArXiv. (2019).
[120] K. Toyoura, Y. Koyama, A. Kuwabara, F. Oba, I. Tanaka, First-principles approach to chemical diffusion of lithium atoms in a graphite intercalation compound, Phys. Rev. B - Condens. Matter Mater. Phys. 78 (2008) 1–12. https://doi.org/10.1103/PhysRevB.78.214303.
[121] H. Oka, Y. Makimura, T. Uyama, T. Nonaka, Y. Kondo, C. Okuda, Changes in the stage structure of Li-intercalated graphite electrode at elevated temperatures, J. Power Sources. 482 (2021) 228926. https://doi.org/10.1016/j.jpowsour.2020.228926.
[122] E.M. Gavilán-Arriazu, O.A. Pinto, B.A. López de Mishima, D.E. Barraco, O.A. Oviedo, E.P.M. Leiva, The kinetic origin of the Daumas-Hérold model for the Li-ion/graphite intercalation system, Electrochem. Commun. 93 (2018) 133–137. https://doi.org/10.1016/j.elecom.2018.07.004.
[123] E.M. Gavilán-Arriazu, M.P. Mercer, O.A. Pinto, O.A. Oviedo, D.E. Barraco, H.E. Hoster, E.P.M. Leiva, Effect of temperature on the kinetics and thermodynamics of electrochemical insertion of Li-ions into a graphite electrode, J. Electrochem. Soc. 167 (2020) 013533. https://doi.org/http://jes.ecsdl.org/content/167/1/013533.abstract.
[124] M.D. Levi, C. Wang, D. Aurbach, Z. Chvoj, Effect of temperature on the kinetics and thermodynamics of electrochemical insertion of Li-ions into a graphite electrode, J. Electroanal. Chem. 562 (2004) 187–203. https://doi.org/10.1016/j.jelechem.2003.08.032.
[125] M.A. Cabañero, N. Boaretto, M. Röder, J. Müller, J. Kallo, A. Latz, Direct determination of diffusion coefficients in commercial Li-ion batteries, J. Electrochem. Soc. 165 (2018) A847–A855. https://doi.org/10.1149/2.0301805jes.

[126] X. Ji, Y. Wang, J. Zhang, Understanding the anisotropic strain effects on lithium diffusion in graphite anodes: A first-principles study, Phys. B Condens. Matter. 539 (2018) 66–71. https://doi.org/10.1016/j.physb.2018.03.046.

[127] G. Hasegawa, N. Kuwata, Y. Tanaka, T. Miyazaki, N. Ishigaki, K. Takada, J. Kawamura, Tracer diffusion coefficients of Li+ions inc-axis oriented LixCoO2thin films measured by secondary ion mass spectrometry, Phys. Chem. Chem. Phys. 23 (2021) 2438–2448. https://doi.org/10.1039/d0cp04598e.

[128] E.E. Levin, S.Y. Vassiliev, V.A. Nikitina, Solvent effect on the kinetics of lithium ion intercalation into LiCoO2, Electrochim. Acta. 228 (2017) 114–124. https://doi.org/10.1016/j.electacta.2017.01.040.

[129] S. Chauque, F.Y. Oliva, A. Visintin, D. Barraco, E.P.M. Leiva, O.R. Cámara, Lithium titanate as anode material for lithium ion batteries: Synthesis, post-treatment and its electrochemical response, J. Electroanal. Chem. 799 (2017) 142–155. https://doi.org/10.1016/j.jelechem.2017.05.052.

[130] Y. Chang, J. Jong, G.T. Fey, Kinetic Characterization of the Electrochemical Intercalation of Lithium Ions into Graphite Electrodes, J. Electrochem. Soc. 147 (2000) 2033–2038. https://doi.org/10.1149/1.1393481.

[131] J.P. Zheng, D.J. Crain, D. Roy, Kinetic aspects of Li intercalation in mechano-chemically processed cathode materials for lithium ion batteries: Electrochemical characterization of ball-milled LiMn2O4, Solid State Ionics. 196 (2011) 48–58. https://doi.org/10.1016/j.ssi.2011.06.004.

[132] M.D. Levi, D. Aurbach, The application of electroanalytical methods to the analysis of phase transitions during intercalation of ions into electrodes, J Solid State Electrochem. (2007) 1031–1042. https://doi.org/10.1007/s10008-007-0264-x.

[133] M.D. Levi, E. Markevich, D. Aurbach, The Effect of Slow Interfacial Kinetics on the Chronoamperometric Response of Composite Lithiated Graphite Electrodes and on the Calculation of the Chemical Diffusion Coefficient of Li Ions in Graphite, J. Phys. Chem. B. 109 (2005) 7420–7427. https://doi.org/https://doi.org/10.1021/jp0441902.

[134] J. Haruyama, T. Ikeshoji, M. Otani, Analysis of Lithium Insertion / Desorption Reaction at Interfaces between Graphite Electrodes and Electrolyte Solution Using Density Functional + Implicit Solvation Theory, J. Phys. Chem. C. 122 (2018) 9804–9810. https://doi.org/10.1021/acs.jpcc.8b01979.

[135] T. Abe, H. Fukuda, Y. Iriyama, Z. Ogumi, Solvated Li-Ion Transfer at Interface Between Graphite and Electrolyte, J. Electrochem. Soc. 151 (2004) 1120–1123. https://doi.org/10.1149/1.1763141.

[136] Y. Yamada, Y. Iriyama, T. Abe, Z. Ogumi, Kinetics of Lithium Ion Transfer at the Interface between Graphite and Liquid Electrolytes : Effects of Solvent and Surface Film, Langmuir. 25 (2009) 12766–12770. https://doi.org/10.1021/la901829v.

[137] S.W. Kim, S. Il Pyun, Analysis of cell impedance measured on the LiMn2O4 film electrode by PITT and EIS with Monte Carlo simulation, J. Electroanal. Chem. 528 (2002) 114–120. https://doi.org/10.1016/S0022-0728(02)00900-2.

[138] G.T.B. M.E.J. Newman, Monte Carlo Method in statistical physics, Clarenton –Press Oxford, 1999.

[139] K.N. Jung, S. Il Pyun, S.W. Kim, Thermodynamic and kinetic approaches to lithium intercalation into Li[Ti5/3Li1/3]O4 film electrode, J. Power Sources. 119–121 (2003) 637–643. https://doi.org/10.1016/S0378-7753(03)00192-7.

[140] C.Y. Ouyang, S.Q. Shi, Z.X. Wang, H. Li, X.J. Huang, L.Q. Chen, Ab initio molecular-dynamics studies on 'LixMi2O 4 as cathode material for lithium secondary batteries, Europhys. Lett.

67 (2004) 28–34. https://doi.org/10.1209/epl/i2004-10049-1.
[141] C. Hin, Kinetic monte carlo simulations of anisotropic lithium intercalation into LixFePO4 electrode nanocrystals, Adv. Funct. Mater. 21 (2011) 2477–2487. https://doi.org/10.1002/adfm.201002049.
[142] R.E. García, Y.-M. Chiang, W. Craig Carter, P. Limthongkul, C.M. Bishop, Microstructural Modeling and Design of Rechargeable Lithium-Ion Batteries, J. Electrochem. Soc. 152 (2005) A255. https://doi.org/10.1149/1.1836132.
[143] J.L. Dodd, Phase composition and dynamical studies of lithium iron phosphate, California Institute of Technology Pasadena, California, 2007. http://thesis.library.caltech.edu/1662/.
[144] P. Xiao, G. Henkelman, Kinetic Monte Carlo Study of Li Intercalation in LiFePO4, ACS Nano. 12 (2018) 844–851. https://doi.org/10.1021/acsnano.7b08278.
[145] E.D. Cubuk, W.L. Wang, K. Zhao, J.J. Vlassak, Z. Suo, E. Kaxiras, Morphological evolution of Si nanowires upon lithiation: A first-principles multiscale model, Nano Lett. 13 (2013) 2011–2015. https://doi.org/10.1021/nl400132q.
[146] X.H. Liu, H. Zheng, L. Zhong, S. Huang, K. Karki, L.Q. Zhang, Y. Liu, A. Kushima, W.T. Liang, J.W. Wang, J.H. Cho, E. Epstein, S.A. Dayeh, S.T. Picraux, T. Zhu, J. Li, J.P. Sullivan, J. Cumings, C. Wang, S.X. Mao, Z.Z. Ye, S. Zhang, J.Y. Huang, Anisotropic swelling and fracture of silicon nanowires during lithiation, Nano Lett. 11 (2011) 3312–3318. https://doi.org/10.1021/nl201684d.
[147] S. Krishnan, G. Brenet, E. Machado-charry, D. Caliste, L. Genovese, T. Deutsch, P. Pochet, Revisiting the domain model for lithium intercalated graphite, Appl. Phys. Lett. 103 (2014) 251904. https://doi.org/10.1063/1.4850877.
[148] B. Markovsky, M.D. Levi, D. Aurbach, The basic electroanalytical behavior of practical graphite–lithium intercalation electrodes, Electrochim. Acta. 43 (1998) 2287–2304. https://doi.org/10.1016/S0013-4686(97)10172-4.
[149] M.D. Levi, E. Markevich, D. Aurbach, Comparison between Cottrell diffusion and moving boundary models for determination of the chemical diffusion coefficients in ion-insertion electrodes, Electrochim. Acta. 51 (2005) 98–110. https://doi.org/10.1016/j.electacta.2005.04.007.
[150] A. Wang, S. Kadam, H. Li, S. Shi, Y. Qi, Review on modeling of the anode solid electrolyte interphase (SEI) for lithium-ion batteries, Npj Comput. Mater. 4 (2018). https://doi.org/10.1038/s41524-018-0064-0.
[151] B.K. Antonopoulos, C. Stock, F. Maglia, H.E. Hoster, Solid electrolyte interphase: Can faster formation at lower potentials yield better performance?, Electrochim. Acta. 269 (2018) 331–339. https://doi.org/10.1016/j.electacta.2018.03.007.
[152] R.N. Methekar, P.W.C. Northrop, K. Chen, R.D. Braatz, V.R. Subramanian, Kinetic Monte Carlo Simulation of Surface Heterogeneity in Graphite Anodes for Lithium-Ion Batteries: Passive Layer Formation, J. Electrochem. Soc. 158 (2011) A363. https://doi.org/10.1149/1.3548526.
[153] A.T. Stamps, C.E. Holland, R.E. White, E.P. Gatzke, Analysis of capacity fade in a lithium ion battery, J. Power Sources. 150 (2005) 229–239. https://doi.org/10.1016/j.jpowsour.2005.02.033.
[154] F. Röder, R.D. Braatz, U. Krewer, Multi-scale simulation of heterogeneous surface film growth mechanisms in lithium-ion batteries, J. Electrochem. Soc. 164 (2017) E3335–E3344. https://doi.org/10.1149/2.0241711jes.
[155] F. Röder, R.D. Braatz, U. Krewer, Multi-Scale Modeling of Solid Electrolyte Interface Formation in Lithium-Ion Batteries, Comput. Aided Chem. Eng. 38 (2016) 157–162. https://doi.org/10.1016/B978-0-444-63428-3.50031-X.

[156] C. Shinagawa, H. Ushiyama, K. Yamashita, Multiscale Simulations for Lithium-Ion Batteries: SEI Film Growth and Capacity Fading, J. Electrochem. Soc. 164 (2017) A3018–A3024. https://doi.org/10.1149/2.0381713jes.
[157] O. Borodin, G. V. Zhuang, P.N. Ross, K. Xu, Molecular Dynamics Simulations and Experimental Study of Lithium Ion Transport in Dilithium Ethylene Dicarbonate, J. Phys. Chem. C. 117 (2013) 7433–7444. https://doi.org/10.1021/jp4000494.
[158] S. Shi, Y. Qi, H. Li, L.G. Hector, Defect thermodynamics and diffusion mechanisms in Li2CO 3 and implications for the solid electrolyte interphase in Li-ion batteries, J. Phys. Chem. C. 117 (2013) 8579–8593. https://doi.org/10.1021/jp310591u.
[159] A. Zülke, Y. Li, P. Keil, R. Burrell, S. Belaisch, M. Nagarathinam, M.P. Mercer, H.E. Hoster, High-Energy Nickel-Cobalt-Aluminium Oxide (NCA) Cells on Idle: Anode- versus Cathode-Driven Side Reactions, Batter. Supercaps. (2021) 1–3. https://doi.org/10.1002/batt.202100046.
[160] B.J. Morgan, Lattice-geometry effects in garnet solid electrolytes: A lattice-gas monte carlo simulation study, R. Soc. Open Sci. 4 (2017). https://doi.org/10.1098/rsos.170824.
[161] S. Scarle, M. Sterzel, A. Eilmes, R.W. Munn, Monte Carlo simulation of Li + motion in polyethylene based on polarization energy calculations and informed by data compression analysis, J. Chem. Phys. 123 (2005) 1–13. https://doi.org/10.1063/1.2064647.
[162] M.J. Mees, G. Pourtois, F. Rosciano, B. Put, P.M. Vereecken, A. Stesmans, First-principles material modeling of solid-state electrolytes with the spinel structure, Phys. Chem. Chem. Phys. 16 (2014) 5399–5406. https://doi.org/10.1039/c3cp54610a.
[163] H. Ozaki, K. Kuratani, T. Kiyobayashi, Monte-Carlo Simulation of the Ionic Transport of Electrolyte Solutions at High Concentrations Based on the Pseudo-Lattice Model, J. Electrochem. Soc. 163 (2016) H576–H583. https://doi.org/10.1149/2.0941607jes.
[164] V. Thangadurai, H. Kaack, W.J.F. Weppner, Novel fast lithium ion conduction in garnet-type Li5La3M2O12 (M = Nb, Ta), J. Am. Ceram. Soc. 86 (2003) 437–440. https://doi.org/10.1111/j.1151-2916.2003.tb03318.x.
[165] W. Li, Y. Ando, E. Minamitani, S. Watanabe, Study of Li atom diffusion in amorphous Li3PO4 with neural network potential, J. Chem. Phys. 147 (2017). https://doi.org/10.1063/1.4997242.
[166] H. Woo, J. Kang, J. Kim, C. Kim, S. Nam, B. Park, Development of carbon-based cathodes for Li-air batteries: Present and future, Electron. Mater. Lett. 12 (2016) 551–567. https://doi.org/10.1007/s13391-016-6183-1.
[167] W. Kang, N. Deng, J. Ju, Q. Li, D. Wu, X. Ma, L. Li, M. Naebe, B. Cheng, A review of recent developments in rechargeable lithium-sulfur batteries, Nanoscale. 8 (2016) 16541–16588. https://doi.org/10.1039/c6nr04923k.
[168] X. Fan, W. Sun, F. Meng, A. Xing, J. Liu, Advanced chemical strategies for lithium–sulfur batteries: A review, Green Energy Environ. 3 (2018) 2–19. https://doi.org/10.1016/j.gee.2017.08.002.
[169] A. Aryanfar, D. Brooks, B. V. Merinov, W.A. Goddard, A.J. Colussi, M.R. Hoffmann, Dynamics of lithium dendrite growth and inhibition: Pulse charging experiments and monte carlo calculations, J. Phys. Chem. Lett. 5 (2014) 1721–1726. https://doi.org/10.1021/jz500207a.
[170] A. Aryanfar, T. Cheng, A.J. Colussi, B. V. Merinov, W.A. Goddard, M.R. Hoffmann, Annealing kinetics of electrodeposited lithium dendrites, J. Chem. Phys. 143 (2015). https://doi.org/10.1063/1.4930014.
[171] B.S. Vishnugopi, F. Hao, A. Verma, P.P. Mukherjee, Double-Edged Effect of Temperature on Lithium Dendrites, ACS Appl. Mater. Interfaces. 12 (2020) 23931–23938. https://doi.org/10.1021/acsami.0c04355.

[172] M. Jäckle, K. Helmbrecht, M. Smits, D. Stottmeister, A. Groß, Self-diffusion barriers: Possible descriptors for dendrite growth in batteries?, Energy Environ. Sci. 11 (2018) 3400–3407. https://doi.org/10.1039/c8ee01448e.

[173] B. Ghalami Choobar, H. Modarress, R. Halladj, S. Amjad-Iranagh, Electrodeposition of lithium metal on lithium anode surface, a simulation study by: Kinetic Monte Carlo-embedded atom method, Comput. Mater. Sci. 192 (2021) 110343. https://doi.org/10.1016/j.commatsci.2021.110343.

[174] M. Van Soestbergen, Frumkin-Butler-Volmer theory and mass transfer in electrochemical cells, Russ. J. Electrochem. 48 (2012) 570–579. https://doi.org/10.1134/S1023193512060110.

[175] M. Jäckle, A. Groß, Microscopic properties of lithium, sodium, and magnesium battery anode materials related to possible dendrite growth, J. Chem. Phys. 141 (2014). https://doi.org/10.1063/1.4901055.

[176] M. Jäckle, A. Groß, Influence of electric fields on metal self-diffusion barriers and its consequences on dendrite growth in batteries, J. Chem. Phys. 151 (2019) 1–16. https://doi.org/10.1063/1.5133429.

[177] L.J. Zhou, Z.F. Hou, L.M. Wu, Y.F. Zhang, First-principles studies of lithium adsorption and diffusion on graphene with grain boundaries, J. Phys. Chem. C. 118 (2014) 28055–28062. https://doi.org/10.1021/jp5102175.

[178] D. Gaissmaier, D. Fantauzzi, T. Jacob, First principles studies of self-diffusion processes on metallic lithium surfaces, J. Chem. Phys. 150 (2019). https://doi.org/10.1063/1.5056226.

[179] P. Hundekar, S. Basu, J. Pan, S.F. Bartolucci, S. Narayanan, Z. Yang, N. Koratkar, Exploiting self-heat in a lithium metal battery for dendrite healing, Energy Storage Mater. 20 (2019) 291–298. https://doi.org/10.1016/j.ensm.2019.04.013.

[180] N. Sitapure, H. Lee, F. Ospina-Acevedo, P.B. Balbuena, S. Hwang, J.S.I. Kwon, A computational approach to characterize formation of a passivation layer in lithium metal anodes, AIChE J. 67 (2021). https://doi.org/10.1002/aic.17073.

[181] Y.C. Chen, C.Y. Ouyang, L.J. Song, Z.L. Sun, Electrical and lithium ion dynamics in three main components of solid electrolyte interphase from density functional theory study, J. Phys. Chem. C. 115 (2011) 7044–7049. https://doi.org/10.1021/jp112202s.

[182] S. Hull, T.W.D. Farley, W. Hayes, M.T. Hutchings, The elastic properties of lithium oxide and their variation with temperature, J. Nucl. Mater. 160 (1988) 125–134. https://doi.org/10.1016/0022-3115(88)90039-6.

[183] P. Guan, L. Liu, X. Lin, Simulation and Experiment on Solid Electrolyte Interphase (SEI) Morphology Evolution and Lithium-Ion Diffusion, J. Electrochem. Soc. 162 (2015) A1798–A1808. https://doi.org/10.1149/2.0521509jes.

[184] G. Blanquer, Y. Yin, M.A. Quiroga, A.A. Franco, Modeling Investigation of the Local Electrochemistry in Lithium-O 2 Batteries: A Kinetic Monte Carlo Approach , J. Electrochem. Soc. 163 (2016) A329–A337. https://doi.org/10.1149/2.0841602jes.

[185] I. Landa-Medrano, R. Pinedo, I.R. de Larramendi, N. Ortiz-Vitoriano, T. Rojo, Monitoring the Location of Cathode-Reactions in Li-O 2 Batteries , J. Electrochem. Soc. 162 (2015) A3126–A3132. https://doi.org/10.1149/2.0191502jes.

[186] Y. Yin, R. Zhao, Y. Deng, A.A. Franco, Compactness of the Lithium Peroxide Thin Film Formed in Li-O2 Batteries and Its Link to the Charge Transport Mechanism: Insights from Stochastic Simulations, J. Phys. Chem. Lett. 8 (2017) 599–604. https://doi.org/10.1021/acs.jpclett.6b02732.

[187] A. Rinaldi, O. Wijaya, H. Hoster, Lithium–Oxygen Cells: An Analytical Model to Explain Key Features in the Discharge Voltage Profiles, ChemElectroChem. 3 (2016) 1944–1950.

https://doi.org/10.1002/celc.201600184.
[188] Z. Liu, P.P. Mukherjee, Mesoscale Elucidation of Surface Passivation in the Li–Sulfur Battery Cathode, ACS Appl. Mater. Interfaces. 9 (2017) 5263–5271. https://doi.org/10.1021/acsami.6b15066.
[189] B.S.D.H. Kim, M.S.B. Lee, K.Y. Park, K. Kang, First-principles Study on the Charge Transport Mechanism of Lithium Sulfide (Li2S) in Lithium-Sulfur Batteries, Chem. - An Asian J. 11 (2016) 1288–1292. https://doi.org/10.1002/asia.201600007.
[190] V. Thangavel, O.X. Guerrero, M. Quiroga, A.M. Mikala, A. Rucci, A.A. Franco, A three dimensional kinetic Monte Carlo model for simulating the carbon/sulfur mesostructural evolutions of discharging lithium sulfur batteries, Energy Storage Mater. 24 (2020) 472–485. https://doi.org/10.1016/j.ensm.2019.07.011.
[191] S. Shi, J. Gao, Y. Liu, Y. Zhao, Q. Wu, W. Ju, C. Ouyang, R. Xiao, Multi-scale computation methods: Their applications in lithium-ion battery research and development, Chinese Phys. B. 25 (2015) 1–24. https://doi.org/10.1088/1674-1056/25/1/018212.
[192] U. Krewer, F. Röder, E. Harinath, R.D. Braatz, B. Bedürftig, R. Findeisen, Review—Dynamic Models of Li-Ion Batteries for Diagnosis and Operation: A Review and Perspective, J. Electrochem. Soc. 165 (2018) A3656–A3673. https://doi.org/10.1149/2.1061814jes.
[193] E.P.M. Leiva, Modeling of lithium-ion batteries is becoming viral : where to go ?, J. Solid State Electrochem. (2020) 20–23. https://doi.org/https://doi.org/10.1007/s10008-020-04703-1.
[194] J.A. Paulson, V. Ramadesigan, V.R. Subramanian, R.D. Braatz, Control systems analysis and design of multiscale simulation models, Proc. Am. Control Conf. 2016-July (2016) 3083–3085. https://doi.org/10.1109/ACC.2016.7525388.
[195] F. Röder, R.D. Braatz, U. Krewer, Direct coupling of continuum and kinetic Monte Carlo models for multiscale simulation of electrochemical systems, Comput. Chem. Eng. 121 (2019) 722–735. https://doi.org/10.1016/j.compchemeng.2018.12.016.
[196] G. Shukla, D. Del Olmo Diaz, V. Thangavel, A.A. Franco, Self-Organization of Electroactive Suspensions in Discharging Slurry Batteries: A Mesoscale Modeling Investigation, ACS Appl. Mater. Interfaces. 9 (2017) 17882–17889. https://doi.org/10.1021/acsami.7b02567.
[197] A. Mace, S. Barthel, B. Smit, Automated Multiscale Approach to Predict Self-Diffusion from a Potential Energy Field, J. Chem. Theory Comput. 15 (2019) 2127–2141. https://doi.org/10.1021/acs.jctc.8b01255.
[198] L. Kahle, A. Marcolongo, N. Marzari, Modeling lithium-ion solid-state electrolytes with a pinball model, Phys. Rev. Mater. 2 (2018) 065405. https://doi.org/10.1103/PhysRevMaterials.2.065405.
[199] C. Chen, Y. Zuo, W. Ye, X. Li, Z. Deng, S.P. Ong, A Critical Review of Machine Learning of Energy Materials, Adv. Energy Mater. 10 (2020) 1–36. https://doi.org/10.1002/aenm.201903242.
[200] N. Artrith, J. Behler, High-dimensional neural network potentials for metal surfaces: A prototype study for copper, Phys. Rev. B - Condens. Matter Mater. Phys. 85 (2012) 1–13. https://doi.org/10.1103/PhysRevB.85.045439.
[201] C. Panosetti, S.B. Anniés, C. Grosu, S. Seidlmayer, C. Scheurer, DFTB Modeling of Lithium-Intercalated Graphite with Machine-Learned Repulsive Potential, J. Phys. Chem. A. 125 (2021) 691–699. https://doi.org/10.1021/acs.jpca.0c09388.
[202] N. Artrith, A. Urban, G. Ceder, Constructing first-principles phase diagrams of amorphous LixSi using machine-learning-assisted sampling with an evolutionary algorithm, J. Chem. Phys. 148 (2018). https://doi.org/10.1063/1.5017661.
[203] A.P. Bartók, J. Kermode, N. Bernstein, G. Csányi, Machine Learning a General-Purpose

Interatomic Potential for Silicon, Phys. Rev. X. 8 (2018) 41048. https://doi.org/10.1103/PhysRevX.8.041048.

[204] Y. Zuo, C. Chen, X. Li, Z. Deng, Y. Chen, J. Behler, G. Csányi, A. V. Shapeev, A.P. Thompson, M.A. Wood, S.P. Ong, Performance and Cost Assessment of Machine Learning Interatomic Potentials, J. Phys. Chem. A. 124 (2020) 731–745. https://doi.org/10.1021/acs.jpca.9b08723.

[205] K. Lee, D. Yoo, W. Jeong, S. Han, SIMPLE-NN: An efficient package for training and executing neural-network interatomic potentials, Comput. Phys. Commun. 242 (2019) 95–103. https://doi.org/10.1016/j.cpc.2019.04.014.

[206] L. Cao, C. Li, T. Mueller, The Use of Cluster Expansions to Predict the Structures and Properties of Surfaces and Nanostructured Materials, J. Chem. Inf. Model. 58 (2018) 2401–2413. https://doi.org/10.1021/acs.jcim.8b00413.

[207] A. Bhowmik, I.E. Castelli, J.M. Garcia-Lastra, P.B. Jørgensen, O. Winther, T. Vegge, A perspective on inverse design of battery interphases using multi-scale modelling, experiments and generative deep learning, Energy Storage Mater. 21 (2019) 446–456. https://doi.org/10.1016/j.ensm.2019.06.011.